

Thesis for the Degree of Doctor of Science

**Observation of $B_s^0 \rightarrow \psi(2S)\phi$ and
Measurement of Branching Ratio
 $\mathcal{B}(B_s^0 \rightarrow \psi(2S)\phi)/\mathcal{B}(B_s^0 \rightarrow J/\psi\phi)$**

Daejung Kong

Department of Physics, Major in Particle Physics

The Graduate School

December 2005

**The Graduate School
Kyungpook National University**

**Observation of $B_s^0 \rightarrow \psi(2S)\phi$ and
Measurement of Branching Ratio
 $\mathcal{B}(B_s^0 \rightarrow \psi(2S)\phi)/\mathcal{B}(B_s^0 \rightarrow J/\psi\phi)$**

Daejung Kong

**Department of Physics, Major in Particle Physics
The Graduate School**

Supervised by Professor DongHee Kim

**Approved as a qualified thesis of Daejung Kong
for the degree of Doctor of Science
by the Evaluation Committee**

December 2005

Chairman	Prof. Kihyeon Cho
	Prof. Intae Yu
	Prof. DongHee Kim
	Prof. Hong Joo Kim
	Prof. Jun-Suhk Suh

The Graduate School Council, Kyungpook National University

Thesis advisor
DongHee Kim

Author
Daejung Kong

**Observation of $B_s^0 \rightarrow \psi(2S)\phi$ and
Measurement of Ratio of Branching
Fractions $\mathcal{B}(B_s^0 \rightarrow \psi(2S)\phi)/\mathcal{B}(B_s^0 \rightarrow J/\psi\phi)$**

Abstract

We report the first observation of $B_s^0 \rightarrow \psi(2S)\phi$ decay in $p\bar{p}$ collisions at $\sqrt{s} = 1.96$ TeV using 360 pb^{-1} of data collected by the CDF II detector at the Fermilab Tevatron. We observe 20.2 ± 5.0 and 12.3 ± 4.1 $B_s^0 \rightarrow \psi(2S)\phi$ candidates, in $\psi(2S) \rightarrow \mu^+\mu^-$ and $\psi(2S) \rightarrow J/\psi\pi^+\pi^-$ decay modes, respectively. We present the first measurement of the relative branching fraction $\mathcal{B}(B_s^0 \rightarrow \psi(2S)\phi)/\mathcal{B}(B_s^0 \rightarrow J/\psi\phi) = 0.52 \pm 0.13(\text{stat.}) \pm 0.04(\text{syst.}) \pm 0.06(\text{BR})$ using the $\psi(2S) \rightarrow \mu^+\mu^-$ decay mode.

Contents

1	Motivation	1
1.1	Electroweak Interactions	1
1.2	Hadroproduction	3
1.3	Hadronization	5
1.4	B mesons to vector-vector decay	6
1.5	Analysis Overview	7
2	Experimental Apparatus	11
2.1	Accelerator	12
2.2	Collider Detector at Fermilab	18
2.2.1	Detector coordinate system	18
2.2.2	Cerenkov Luminosity Counter	21
2.2.3	Tracking System	23
2.2.4	Time-of-Flight	31
2.2.5	Superconducting Solenoid Coil	33
2.2.6	Calorimeters	34
2.2.7	The Central Preradiator & Central Shower Maximum Detector	36
2.2.8	Muon Chambers	37

2.3	Trigger and data acquisition systems	41
3	Data Samples and Selection Cuts	45
3.1	Data Samples	45
3.2	Basic Selections	47
3.3	Selection for $J/\psi, \psi(2S) \rightarrow \mu^+\mu^-$	47
3.4	Selection for $\psi(2S) \rightarrow J/\psi\pi^+\pi^-$	49
3.5	Reconstruction of $B_u^\pm \rightarrow J/\psi K^\pm, B_u^\pm \rightarrow \psi(2S)K^\pm$ and $B_s^0 \rightarrow J/\psi\phi$	50
4	Observation of $B_s^0 \rightarrow \psi(2S)\phi$	57
4.1	Fitting method	57
4.2	Background contributions	58
4.3	Significance of Signal	60
4.4	Details on Background Contribution study	61
5	The measurement of $\mathcal{B}(B_s^0 \rightarrow \psi(2S)\phi)/\mathcal{B}(B_s^0 \rightarrow J/\psi\phi)$	73
5.1	Introduction	73
5.2	Realistic Monte Carlo generation	74
5.3	Monte Carlo sample and data comparison	74
5.4	Relative detection efficiencies for B^\pm and B_s	75
5.5	The measurement of $\mathcal{B}(B_s^0 \rightarrow \psi(2S)\phi)/\mathcal{B}(B_s^0 \rightarrow J/\psi\phi)$	76
6	Systematic studies and consistency checks	81
6.1	Introduction	81
6.2	Monte Carlo comparison between $\psi(2S)$ and J/ψ modes	83
6.3	Systematic Studies	87
6.3.1	Transverse Momentum of Muon	87

CONTENTS

vii

6.3.2	Polarization	87
6.3.3	Fitting	90
6.3.4	Daughter branching fraction	93
6.4	Consistency checks	94
6.4.1	Transverse Momentum of Muon	94
6.4.2	Run ranges	95
6.4.3	Transverse Momentum of Kaon	95
6.4.4	Other cuts	96
6.5	Summary for systematic errors	98
7	Conclusions	99
	Bibliography	101

List of Figures

1.1	Feynman diagram of $B_u^\pm, B_d^0, B_s^0 \rightarrow (J/\psi, \psi(2S))V$	9
1.2	The schematic diagrams of the B meson decay modes.	9
2.1	Fermilab accelerator complex.	14
2.2	Integrated luminosity delivered and recorded at CDF	16
2.3	The summary of delivered luminosity at Tevatron	16
2.4	Data taking efficiency as functions of $p\bar{p}$ stores and time	17
2.5	The initial instantaneous luminosity	17
2.6	Elevation view of one half of the CDF II detector	19
2.7	A schematic view of the CDF Run II Detector	20
2.8	The CDF detector coordinate system	22
2.9	The schematic trajectory of a charged particle	25
2.10	Schematic view of COT endplate	26
2.11	Nomial cell layout for SL2. Other superlayers are similar.	27
2.12	SVX bulkhead, end view. it shows two wedges installed.	30
2.13	Schematic view of CDF tracking system	30
2.14	The separation power as a function of momentum between K/π , p/π , and K/p	32
2.15	The TOF performance plot	32

2.16	Side view of the central region of the CDF II detector	33
2.17	Schematic view of the wedge module of the central electromagnetic calorimeter.	35
2.18	Schematic view of CES.	37
2.19	Cross section of a single muon chamber.	38
2.20	The coverage of muon system	40
2.21	Trigger System Flowchart for CDF	43
2.22	Block diagram of the Run II trigger system at CDF.	44
3.1	The invariance mass distributions of $J/\psi \rightarrow \mu^+\mu^-$	48
3.2	The invariance mass distributions of $\psi(2S) \rightarrow \mu^+\mu^-$	48
3.3	The invariance mass distributions of $\psi(2S) \rightarrow J/\psi\pi^+\pi^-$	49
3.4	$B_u^\pm \rightarrow J/\psi K^\pm$ mass distribution where $J/\psi \rightarrow \mu^+\mu^-$	51
3.5	$B_u^\pm \rightarrow (\psi(2S) \rightarrow \mu^+\mu^-)K^\pm$ mass distribution	51
3.6	$B_s^0 \rightarrow J/\psi\phi$ mass distribution	52
3.7	Cabbibo suppressed B^\pm mass distribution	54
3.8	Fitting of the $B_u^\pm \rightarrow J/\psi K^\pm$ and $B_u^\pm \rightarrow \psi(2S)K^\pm$ mass distribution with the Cabbibo suppressed decay contribution taken into account.	54
4.1	$B_s^0 \rightarrow \psi(2S)\phi$ mass distribution	58
4.2	The combined mass distribution of $B_s^0 \rightarrow \psi(2S)\phi$ decays	59
4.3	$K^{*0} \rightarrow K^+\pi^-$ distribution	64
4.4	Monte Carlo B_d^0 and B_s^0 distribution	64
4.5	Monte Carlo B_d^0 reflection in the B_s^0 signal region	64
4.6	B_d^0 mass distribution fitted with a single Gaussian for signal and 1st order polynomial for background	65

4.7	The B^0 reflection in B_s mass region	67
4.8	$\phi \rightarrow K^+ K^-$ distribution from $B_s^0 \rightarrow J/\psi \phi$	68
4.9	$\phi \rightarrow K^+ K^-$ mass distribution fitted	69
4.10	$\phi \rightarrow K^+ K^-$ distribution from $B_s^0 \rightarrow (\psi(2S) \rightarrow \mu^+ \mu^-) \phi$ decay .	70
4.11	$\phi \rightarrow K^+ K^-$ distribution from $B_s^0 \rightarrow (\psi(2S) \rightarrow \mu^+ \mu^-) \phi$ decay .	71
5.1	Comparison between Monte Carlo sample with data sample in the decay of $B_u^\pm \rightarrow J/\psi K^\pm$	78
5.2	Comparison between Monte Carlo sample with data sample in the decay of $B_u^\pm \rightarrow \psi(2S) K^\pm$	79
5.3	Comparison between Monte Carlo sample with data sample in the decay of $B_s^0 \rightarrow J/\psi \phi$	80
6.1	Comparison between Monte Carlo sample in the decay of $B_s^0 \rightarrow$ $J/\psi \phi$ and $B_s^0 \rightarrow \psi(2S) \phi, \psi(2S) \rightarrow \mu^+ \mu^-$	85
6.2	Comparison between Monte Carlo sample in the decay of $B_u^\pm \rightarrow$ $J/\psi K^\pm$ and $B_u^\pm \rightarrow \psi(2S) K^\pm, \psi(2S) \rightarrow \mu^+ \mu^-$	86
6.3	Comparison between Monte Carlo sample in the decay of CP even and CP odd of $B_s^0 \rightarrow \psi(2S) \phi, \psi(2S) \rightarrow \mu^+ \mu^-$	89
6.4	$B^\pm \rightarrow J/\psi(\psi(2S)) K^\pm$ mass distribution fitted with different range	91
6.5	$B_s^0 \rightarrow J/\psi(\psi(2S)) \phi$ mass distribution fitted with different range	92

List of Tables

1.1	The current relative branching ratio of B meson decays between $\psi(2S)$ and J/ψ final state.	8
2.1	Parameters describing the accelerator configuration in Run I and II	15
2.2	Central Outer Tracker geometry	28
2.3	Silicon tracker geometry	29
3.1	All applied cuts for reconstruction of B_u^\pm	53
3.2	The summary of cuts applied for reconstruction of $B_s^0 \rightarrow J/\psi\phi$, $B_s^0 \rightarrow \psi(2S)\phi$	53
4.1	Summary of fitting results of charmonium final states of Monte Carlo.	60
4.2	Summary of fitting results of charmonium final states using real data	60
4.3	P-value and significance of each decay mode and combined. . . .	61
4.4	Background Contribution from B_d^0 reflection to B_s^0 meson. . . .	63
5.1	The relative efficiencies from Monte Carlo simulation.	76
5.2	The observed number of events.	77
5.3	The PDG values for different decay modes [13].	77
5.4	The measured relative branching ratios	77

6.1	Systematics study using single muon efficiency measured from real data.	88
6.2	Comparison between CP even and CP odd $B_s^0 \rightarrow \psi(2S)\phi$	88
6.3	The systematics study due to fitting.	90
6.4	Consistency check with control sample, with high P_T muons only.	94
6.5	The relative branching ratio of split samples with different muon P_T	94
6.6	Consistency check with control sample, with different run ranges.	95
6.7	Consistency check with control sample, with different kaon P_T ranges.	96
6.8	Consistency checks on different cuts for the control sample $B_u^\pm \rightarrow$ $J/\psi K^\pm$ and $B_u^\pm \rightarrow \psi(2S)K^\pm$ using the “N-1 cut” approach. .	97
6.9	Summary of systematic studies.	98

Chapter 1

Motivation

At hadron colliders, the hadronic B decays involving a charmonium daughter meson is easier to study due to the fact that there are two muons involved in the final states which provides a distinctive signature for trigger selection. As a result, in the past, both hadron collider experiments (such as CDF) and e^+e^- threshold machines have studied extensively many decay modes involving a charmonium resonance. Studies of the decays of B mesons to $\psi(2S)$ final states has contributed to knowledge of hadronic B meson decays and provide insight into the interplay between weak and strong interactions.

1.1 Electroweak Interactions

Quark in their mass-eigenstate generations,

$$\begin{pmatrix} u \\ d \end{pmatrix} \begin{pmatrix} c \\ s \end{pmatrix} \begin{pmatrix} t \\ b \end{pmatrix}$$

may interact weakly with quarks in generations other than their own. The typical notation used to describe the degree of this mixing is the Cabibbo-Kobayashi-Maskawa (CKM) matrix [1, 2],

$$\begin{pmatrix} d' \\ s' \\ b' \end{pmatrix} = \begin{pmatrix} V_{ud} & V_{us} & V_{ub} \\ V_{cd} & V_{cs} & V_{cb} \\ V_{td} & V_{ts} & V_{tb} \end{pmatrix} \begin{pmatrix} d \\ s \\ b \end{pmatrix},$$

which, by convention, leaves the $+2/3$ charged quarks unmixed; the states (d', s', b') are the weak eigenstates. Under the constraints that there be three quark generations and the CKM matrix be unitary, the mixing can be parameterized with three angles and one complex phase. The pursuit of measurements to determine the CKM matrix elements and to observe the charge-parity (CP) violation within the b -quark system (a result of a non-zero complex phase) constitutes a major component of many experimental programs at modern particle accelerators.

The understanding of the weak interactions has its foundations in Fermi's theory of β decay, introduced in 1934 [3]. The four-fermion interaction was retained for several years before Sakurai introduced the universal V-A (vector and axial vector current) modification [4] to accommodate the experimentally observed parity violation. Unfortunately, the V-A Fermi theory violates unitarity violation (the predicted cross sections grew quadratically as a function of the center of mass energy) and is non-renormalizable at high energies. A theory is renormalizable if the predicted amplitudes of physical processes remain finite at all energies and for all powers of the coupling constant, often at the expense of the introduction of a finite number of experimentally determined parameters [5]. The standard model of electroweak interactions, developed primarily by Glashow, Weinberg and Salam in the 1960's [6, 7, 8] and based on the gauge group $SU(2) \times U(1)$, hypothesized four intermediate gauge fields to avoid these difficulties: the W^+ , W^- , Z^0 and the γ bosons. The standard model electroweak Lagrangian that represents the charged-current weak interaction between fermion fields is

$$\mathcal{L}_{cc} = -\frac{g}{2\sqrt{2}} \sum_i \bar{\xi} \gamma^\mu (1 - \gamma^5) (T^+ W_\mu^+ + T^- W_\mu^-) \xi_i \quad (1.1)$$

g is the $SU(2)$ gauge coupling constant, $\gamma^\mu(1 - \gamma^5)$ are the Dirac matrices representing the V-A current, T^+ and T^- are the weak isospin raising and lowering operators, respectively, W_μ^\pm are the massive weak charged boson fields, i represents the families and ξ_i are the fermion fields. In charged-current weak interactions of the b quark, the fermion fields are either left-handed $SU(2)$ doublets, $\xi_3 = \begin{pmatrix} t \\ b' \end{pmatrix}_L$, or right-handed $SU(2)$ singlets, $\xi_3 = (b')_R$, where b' is

the weak eigenstate defined in Equation 1.1.

1.2 Hadroproduction

In the present study, b and \bar{b} quarks were produced in 1.96 TeV collision of protons and antiprotons by way of the inclusive process

$$p(k_p) + \bar{p}(k_{\bar{p}}) \rightarrow b(k_b) + \bar{b}(k_{\bar{b}}) + X \quad (1.2)$$

X denotes the 'underlying event' and k_p and $k_{\bar{p}}$ (k_b and $k_{\bar{b}}$) are the momenta of the baryons (b quarks). Note that the $p(\bar{p})$ baryons each comprise several partons: the $uud(\bar{u}\bar{u}\bar{d})$ 'valence' quarks, gluons, and many 'sea' quark-antiquark pairs. A perturbative QCD formula for the invariant differential hadroproduction cross section of a b quark with energy E_b and mass m_b can be expressed by convolving the partonic cross section ($\hat{\sigma}$) with the parton distribution functions of the hadron reactants in the form [?]

$$\frac{E_b d^3\sigma}{d^3k_b} = \sum_{i,j} \int_0^1 dx_1 \int_0^1 dx_2 \left[\frac{E_b d^3\hat{\sigma}_{ij}}{d^3k_b}(x_1 k_p, x_2 k_{\bar{p}}, k_b; m_b, \mu, \Lambda) \right] F_i^p(x_1, Q^2) F_j^{\bar{p}}(x_2, Q^2), \quad (1.3)$$

where $x_1 k_p$ and $x_2 k_{\bar{p}}$ are the momenta of the incoming partons, $F_{i,j}^{p,\bar{p}}$ are the parton distribution functions for the i^{th} and j^{th} parton in the p and \bar{p} baryons, respectively, and Q^2 is the square of the four-momentum transfer. The parameter μ represents the energy scale of the process and, by assumption, $|Q| \equiv \mu$. The quantity Λ is an experimentally-determined parameter used in the description of the strong coupling constant, α_s , on the energy scale, μ . Integrating Equation refppdf over the momentum k_b yields the total cross section for the production of a b quark,

$$\sigma(s) = \sum_{i,j} \int_0^1 dx_1 \int_0^1 dx_2 \hat{\sigma}_{ij}(x_1 x_2 s; m_b, \mu, \Lambda) F_i^p(x_1, \mu^2) F_j^{\bar{p}}(x_2, \mu^2), \quad (1.4)$$

where s is the square of the center of mass energy of the colliding proton and antiproton. The threshold condition for $b\bar{b}$ production is met when the square of the parton-parton center of mass energy, $\hat{s} \equiv x_1 x_2 s$, satisfies the condition

$\hat{s} = 4m_b^2$. The heavy mass of the b quark makes possible QCD calculations of $\hat{\sigma}_{ij}$ as a perturbation series in powers of the running strong coupling constant, α_s . The first terms in the series that contribute to the cross section are $\mathcal{O}(\alpha_s^2)$ quark-antiquark annihilation or gluon-gluon fusion processes [9]:

$$\begin{aligned} q + \bar{q} &\rightarrow b + \bar{b} \\ g + g &\rightarrow b + \bar{b} \end{aligned} \tag{1.5}$$

The next-to-leading $\mathcal{O}(\alpha_s^3)$ terms in the perturbative series arise from the processes like

$$\begin{aligned} q + \bar{q} &\rightarrow b + \bar{b} + g \\ g + g &\rightarrow b + \bar{b} + g \\ g + q &\rightarrow b + \bar{b} + q \\ g + \bar{q} &\rightarrow b + \bar{b} + \bar{q} \end{aligned} \tag{1.6}$$

Due to interference with diagrams containing virtual gluons, the two processes in Equation 1.5 can also contribute at $\mathcal{O}(\alpha_s^3)$. For high energies, *i.e.*, when $k_T(b) \gg m_b$, where $k_T(b)$ is the momentum of the b quark projected onto a plane perpendicular to the axis of the two incoming partons, some of the next-to-leading order $\mathcal{O}(\alpha_s^3)$ mechanisms can contribute to the cross section by amounts comparable to the $\mathcal{O}(\alpha_s^2)$ contributions [10, 11]. In Equation 1.3 and 1.4, there is a degree of arbitrariness in the value of the renormalization scale, μ , that contributes a relatively large uncertainty to QCD predictions of b -quark production because they are not calculated to all orders in α_s . The value of μ is typically assigned to be near a physical scale, such as m_b or $\sqrt{m_b^2 + k_T^2(b)}$; however, these choices of μ are “bootstrapped” because the fact that b quarks are confined inside hadrons requires that extractions of m_b depend on the renormalization scheme used, model-specific definitions of m_b , and the value of μ itself [12, 13]. Nason, Dawson and Ellis (NDE) have calculated $\frac{d^2\sigma}{dy_b dk_T^2(b)}$, the inclusive differential b -quark production cross section, as a function of rapidity, y_b , and $k_T(b)$ [10, 11]. Rapidity is a measure of the

polar angle of a particle's trajectory, usually with respect to the collision axis, and is defined for a b quark as

$$y_b \equiv \frac{1}{2} \ln \left[\frac{E_b + k_z(b)}{E_b - k_z(b)} \right], \quad (1.7)$$

where $k_z(b)$ is the projection of the b -quark momentum onto the beam axis. The rapidity variable is useful to descriptions of high energy particle production because the shape of the particle-multiplicity distribution, dN/dy_b , is Lorentz-invariant; reference frame transformations amount to linear shifts in the origin of y_b [13].

1.3 Hadronization

The process of forming B hadrons from b quarks produced through hard scattering is called hadronization or fragmentation. It is a low Q^2 , non-perturbative QCD process. The hadronization process is commonly described by the semi-empirical string fragmentation model [14] that describes the quark-antiquark interaction with the potential $V(r) \propto kr$. As the quark and the antiquark separate, the string stretches, and the potential energy increases until a new $q\bar{q}$ pair is created out of the vacuum to form the new ends of the string. The new strings can stretch and break, as well, and form more $q\bar{q}$ pairs until the available energy is exhausted. These new particles are referred to as fragmentation particles and include B hadrons. The fragmentation process can be characterized by z , the fraction of the initial b quark momentum that is carried by the B meson. The probability distribution of the B meson P_T is described by a fragmentation function $D(z)$. Since fragmentation is a long-distance process and not calculable by perturbative QCD, a semi-empirical parameterization is used. Because the mass of the b quark is large, the B meson it forms carries most of the initial P_T . Therefore, $D(z)$ is expected to peak near the maximum value of $z = 1$. The parameterization by Peterson et al. [15] incorporates this expectation:

$$D(z) = \frac{N}{z(1 - 1/z - \epsilon(1 - z))^2} \quad (1.8)$$

where N is set by the normalization requirement that $\int_0^1 D(z)dz = 1$. The term $1 - 1/z - \epsilon(1 - z)$ is the energy lost by the b quark through gluon emission. The Peterson parameter, ϵ , depends on the energy of the gluon products and is determined experimentally to be $\epsilon = 0.006 \pm 0.002$ [16]. The value is based on a survey of several experimental e^+e^- observations. The search continues for better understanding of b quark fragmentation, its sensitivity to the type of collision environment in which the b quark was produced and the flavor of the non- b quark constituting the final state hadron.

1.4 B mesons to vector-vector decay

The weak decays of B mesons to vector-vector final states are of interest for many reasons, and much work has been done in analysing them within the framework of the Standard Model [17, 18, 19, 20, 21]. The decays involve the transformation of the b quark into a c quark and the generation of $\bar{c}s$ pair. The $\bar{c}c$ pair forms the J/ψ , while the s combines with the spectator to produce the second final state vector meson. Among other things, the decays provide us with the opportunity to test the so-called “factorization ansatz” that is often used as a calculational simplification. The common test of the factorization ansatz consists of comparing its simultaneous predictions for the longitudinal polarization fraction and the ratio of branching ratios of the decays $B_u^\pm \rightarrow J/\psi K^\pm$ and $B_d^0 \rightarrow J/\psi K^{*0}$, with measurements. Early results found that these two quantities were antagonistic: tuning the calculation to better predict one worsened the prediction of the other. However, the uncertainties on the measurements did not rule out factorization.

Another motivation for studying $B \rightarrow VV$ decays is to search for CP violation in the b system. The decay $B^0 \rightarrow J/\psi K_s$ is known as the “golden mode” for measuring the unitarity triangle β and hence, CP violation. The reason it is such a good mode for this study is that the final state is invariant under CP : $J/\psi \rightarrow l^+l^-$ and $K_S \rightarrow \pi^+\pi^-$. Violation of CP invariance appears as an asymmetry in the decay rates to this final state as a function of the mixing of the $B^0 - \bar{B}^0$ system. The observation of CP violation in B^0 decays were

reported by the CDF [24], BaBar [25] and Belle [26] experiment.

In addition, B_s^0 meson has two mass eigenstates ($B_{s,H}^0$ and $B_{s,L}^0$) with definite masses (heavy, m_H and light, m_L) and widths (Γ_H and Γ_L). One of the more interesting quantities in this system is the fractional difference in decay widths of the two mass states. For the B_d^0 system this difference is predicted to be of the order of 10^{-3} , making it too small to see with current experimental data sets. However, for B_s system, predictions are generally of the order of 10% [19, 23]. This clearly makes this a much more interesting decay to study. Since $B_{s,H}^0$ and $B_{s,L}^0$ are very nearly CP eigenstates, they will decay to distinct angular distributions. This enhances the statistical precision with which one can measure a lifetime difference. If $B_s^0 \rightarrow J/\psi\phi$ decay is dominantly one CP state, we can obtain the lifetime difference by measuring the average lifetime in the VV chain and measuring it in a decay where the admixture is perforce 50/50, one can perform a simultaneous fit to two lifetime components in the VV decay using the angular distribution in a weighting function to isolate the CP even and odd components. This increases the statistical power of a two component lifetime fit to determine the difference. In both cases, the information on the decay content can be provided by a polarization analysis.

1.5 Analysis Overview

Historically, observing $\psi(2S)$ final states of B meson decays is, to some extent, a measure of the B physics capability for a given experiment. For example, B_u^\pm was first observed at ARUGS in 1990 [27], and B_d^0 was observed at CDF (Run I) in 1998 [28]. CLEO observed $B_d^0 \rightarrow \psi(2S)Ks$ and $B_u^+ \rightarrow \psi(2S)K^{*+}$ in 2000 [29].

All these decay modes have been subsequently studied with more statistics by many experiments. Fig. 1.1 shows the tree level decay diagrams for the decay modes for B_u^\pm, B_d^0 as well as B_s^0 mesons. The measurements show that the rates of B_u^\pm and B_d^0 mesons decay to the $\psi(2S)$ final states is approximately 60% of the rates of the analogous decays to the J/ψ final states. For the B_s^0 meson, up to now the $B_s^0 \rightarrow J/\psi\phi$ decay has been observed and ALEPH

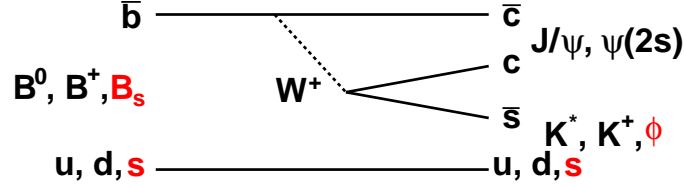
experiment reported one candidate event of $B_s^0 \rightarrow \psi(2S)\phi$ in 1993 [30]. The relative branching ratio between $B_s^0 \rightarrow \psi(2S)\phi$ and $B_s^0 \rightarrow J/\psi\phi$ has not been measured. Table 1.1 shows the current relative branching ratio of B meson decays between $\psi(2S)$ and J/ψ final state.

Decay channel	Value	Reference
$\frac{\mathcal{B}(B_u^\pm \rightarrow \psi(2S)K^\pm)}{\mathcal{B}(B_u^\pm \rightarrow J/\psi K^\pm)}$	$0.64 \pm 0.06 \pm 0.07$	BaBar 2002 [31]
$\frac{\mathcal{B}(B_d^0 \rightarrow \psi(2S)K^{*0})}{\mathcal{B}(B_d^0 \rightarrow J/\psi K^{*0})}$		
	0.61 ± 0.10	PDG 2004 [13]

Table 1.1: The current relative branching ratio of B meson decays between $\psi(2S)$ and J/ψ final state.

The $B_s^0 \rightarrow J/\psi\phi$ mode has recently been used to determine the decay widths for the heavy and light B_s^0 mass eigenstates by measuring the relative contribution of the CP-odd and CP-even components to the observed angular distribution as function of the decay time [32]. Observing the $B_s^0 \rightarrow \psi(2S)\phi$ would allow an independent measurement of the decay widths for the heavy and light B_s^0 mass eigenstates in the future. In particular, the polarization of $B_s^0 \rightarrow \psi(2S)\phi$ could be different from that of $B_s^0 \rightarrow J/\psi\phi$. We will describe first the search for $B_s^0 \rightarrow \psi(2S)\phi$ mode, then the measurement of the relative branching ratio between $B_s^0 \rightarrow \psi(2S)\phi$ and $B_s^0 \rightarrow J/\psi\phi$ where $\psi(2S)$, J/ψ decay to $\mu^+\mu^-$.

For the decay mode of $B_s^0 \rightarrow \psi(2S)\phi$, there are two channels [33]. One is $\psi(2S) \rightarrow \mu^+\mu^-$ and the other is $\psi(2S) \rightarrow J/\psi\pi^+\pi^-$. For observation of $B_s^0 \rightarrow \psi(2S)\phi$ mode, we will use both channels. However, for relative branching ratio measurement, we will use only $J/\psi, \psi(2S) \rightarrow \mu^+\mu^-$ channel. Since the decay topology is very similar between $B_s^0 \rightarrow \psi(2S)\phi$ and $B_s^0 \rightarrow J/\psi\phi$ for the di-muon mode, as shown in Fig. 1.2, it is relative easy to measure the relative branching ratio. The corresponding B_u^\pm can be used as control samples. In taking the ratio between the two decay modes of B_s^0 , the uncertainties in the bottom-quark production cross section, fragmentation, luminosity etc. will cancel out. In addition, this also results in cancellation of other systematic

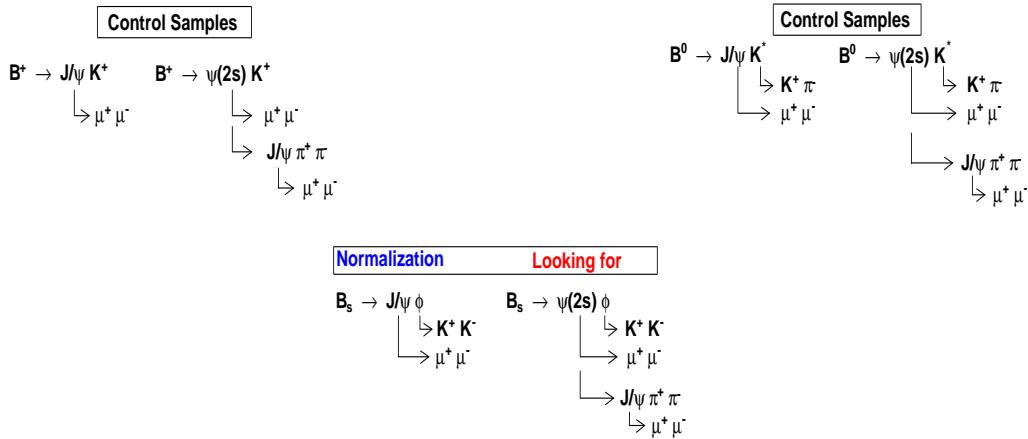
Figure 1.1: Feynman diagram of $B_u^\pm, B_d^0, B_s^0 \rightarrow (J/\psi, \psi(2S))V$

effects due to detection and reconstruction and their associated uncertainties.

The number of observed candidates for the decay mode $N(B_s^0 \rightarrow \psi(2S)\phi)$ can be decomposed into the form:

$$N(B_s^0 \rightarrow \psi(2S)\phi) = \int \mathcal{L} dt \cdot \sigma(p\bar{p} \rightarrow b) \cdot f_s \cdot \mathcal{B}(B_s^0 \rightarrow \psi(2S)\phi) \cdot \epsilon_{\psi(2S)\phi} \quad (1.9)$$

and similar forms can be written for the other B decays considered here. Here, $\int \mathcal{L} dt$ is time integrated luminosity, $\sigma(p\bar{p} \rightarrow b)$ is the bottom quark production cross section, and f_s is the probability that the fragmentation of a bottom quark will result in a B_s^0 meson.

Figure 1.2: The schematic diagrams of the B meson decay modes.

The expression $\mathcal{B}(B_s^0 \rightarrow \psi(2S)\phi)$ represents the branching fraction for the B_s^0 decay mode, and $\epsilon_{\psi(2S)\phi}$ is the acceptance and efficiency of detecting the final state. Therefore the relative branching fraction can be determined as follows (similar forms can be written for control samples as well):

$$\begin{aligned} & \frac{\mathcal{B}(B_s^0 \rightarrow \psi(2S)\phi)}{\mathcal{B}(B_s^0 \rightarrow J/\psi\phi)} \\ &= \frac{N(B_s^0 \rightarrow \psi(2S)\phi)\mathcal{B}(J/\psi \rightarrow \mu^+\mu^-)\mathcal{B}(\phi \rightarrow KK)}{N(B_s^0 \rightarrow J/\psi\phi)\mathcal{B}(\psi(2S) \rightarrow \mu^+\mu^-)\mathcal{B}(\phi \rightarrow K^+K^-)} \times \epsilon \\ &= \frac{N(B_s^0 \rightarrow \psi(2S)\phi)\mathcal{B}(J/\psi \rightarrow \mu^+\mu^-)}{N(B_s^0 \rightarrow J/\psi\phi)\mathcal{B}(\psi(2S) \rightarrow \mu^+\mu^-)} \times \epsilon \end{aligned} \quad (1.10)$$

where ϵ is the relative efficiency of $\epsilon = \frac{\epsilon_{(B_s^0 \rightarrow J/\psi\phi; J/\psi \rightarrow \mu^+\mu^-)}}{\epsilon_{(B_s^0 \rightarrow \psi(2S)\phi; \psi(2S) \rightarrow \mu^+\mu^-)}}$. The $\epsilon_{(B_s^0 \rightarrow J/\psi\phi)}$ and $\epsilon_{(B_s^0 \rightarrow \psi(2S)\phi)}$ are acceptances and efficiency products. We have already known the branching ratios of $\mathcal{B}(J/\psi \rightarrow \mu^+\mu^-) = (5.88 \pm 0.10)\%$ and $\mathcal{B}(\psi(2S) \rightarrow \mu^+\mu^-) = (7.3 \pm 0.8)^{-5}$ [13], what we need to measure are the observed event yields for $N(B_s^0 \rightarrow J/\psi\phi)$ and $N(B_s^0 \rightarrow \psi(2S)\phi)$ from data and determine the ratio of detection efficiencies (including trigger, reconstruction as well as analysis selection cuts). We can use the control samples to check the procedure and study the systematics. Note that in this approach, the total integrated luminosity, bottom quark production cross section, probability of fragmentation, as well as some of the detection and reconstruction efficiencies drop from the ratio.

We begin with a summary of the experiment apparatus and particle detection, triggers, data samples. We first describe the analysis approach, event selection criteria for the $B_s^0 \rightarrow \psi(2S)\phi$ final state, Then we will present the results on the control samples ($B_u^\pm \rightarrow \psi(2S)K^\pm$ and $B_u^\pm \rightarrow J/\psi K^\pm$), the normalization mode ($B_s^0 \rightarrow J/\psi\phi$), as well as the observation of $B_s^0 \rightarrow \psi(2S)\phi$, using both $\psi(2S) \rightarrow \mu^+\mu^-$ and $\psi(2S) \rightarrow J/\psi\pi^+\pi^-$. The rest of this thesis describes the measurement on the relative branch ratios and the systematics.

Chapter 2

Experimental Apparatus

The Tevatron proton-antiproton Collider is the highest-energy particle collider currently operational anywhere in the world. The Collider Detector at Fermilab(CDF) is an azimuthally and forward-backward symmetric apparatus designed to study proton-antiproton collisions at the Tevatron.

During the period between 1997 and 2001 both the accelerator complex and CDF underwent major upgrade to increase instantaneous luminosity and take data sample of eventually 2 fb^{-1} of integrated luminosity or more. The upgraded accelerator has a shorter time between beam crossings than its predecessor: 396 ns in the current 36-bunch mode compared to $3.5 \mu\text{s}$ in the old 6-bunch mode. The new configuration required detector upgrades to ensure a maximum response time shorter than the time between beam crossings.

This chapter describe the accelerator and the detector components used to identify and measure properties of the particles produced during the $p\bar{p}$ collisions.

2.1 Accelerator

The Tevatron is a superconducting particle accelerator and collider that is four miles in circumference. It accelerates protons and anti-protons up to 980 GeV and collides to produce elemental particles. A sketch of the accelerator complex at Fermilab is shown in Figure 2.1.

Generally a large number of $p\bar{p}$ collisions must occur to observe processes with small production cross section. The parameter that gives the rate of collisions is the luminosity, defined by the relation

$$N = \sigma \mathcal{L} \quad (2.1)$$

where N is the number of events produced per second for some final state, σ is the production cross section for that state and \mathcal{L} is the luminosity in units of $cm^{-2}s^{-1}$.

At two points around the Tevatron (“B0” and “D0”) the beams are focused by quadrupole magnets to achieve the highest luminosity possible within the detectors: CDF and DØ. The luminosity at the Tevatron can be expressed as:

$$\mathcal{L} = \frac{fBN_pN_{\bar{p}}}{2\pi(\sigma_p^2 + \sigma_{\bar{p}}^2)} F \left(\frac{\sigma_l}{\beta^*} \right) \quad (2.2)$$

where f is the revolution frequency at which proton or anti-proton travel around the Tevatron, which is about 70 kHz. B is the number of bunches, which is 36 now. N_p and $N_{\bar{p}}$ are the numbers of particles in proton and anti-proton bunches, typically about the order of 10^{11} and 10^{10} respectively. σ_p and $\sigma_{\bar{p}}$ are the rms beam size at the interaction point. F is a form factor which depends on the ratio of σ_l , the bunch length, to β^* , the beta function at the interaction point. The beta function is a measure of the beam width, and is proportional to the beam’s x and y extent in phase space. Anti-Proton availability is the most limiting factor for attaining high luminosities. The proton and anti-proton beams circulating in the Tevatron are unpolarized, and bunches exhibit a longitudinal density profile such that the resulting distribu-

tion of collisions along the beam axis is Gaussian, with a width of about 30 cm. Table 2.1 shows a comparison of Run I and Run II accelerator parameters.

The beam begins from a Cockcroft-Walton pre-accelerator [34] which accelerates H^- ions to 0.75 MeV. And the Linear accelerator (Linac) takes the H^- ions from 0.75 MeV kinetic energy to 400 MeV.

The Linac has two parts: 116 MeV drift-tube (Alvarez) linac operating at 201.25 MHz and a 400 MeV side-coupled cavity linac operating at 805 MHz [35]. Because of the Linac geometry, the accelerated ions become grouped into bunches.

Then they are injected into the Booster ring (a rapid cycling synchrotron with a diameter of 74.5 m) and two electrons are removed from the H^- ions by a thin carbon foil strips, leaving protons. Successive turns of ions are injected into the same orbit as the circulating protons. The protons are accelerated to 8 GeV in the booster before they are extracted into the Main Injector (MI), which operates at 53 MHz. This is accomplished by a series of electromagnetic kicks applied by RF cavities, about 500 kV per turn.

The Main Injector accepts these protons and continues the acceleration process, increasing their energy to 150 GeV. In addition, the Main Injector accelerates a portion of the protons to 120 GeV for use in anti-proton production. Then the 150 GeV protons from the Main Injector are delivered to the Tevatron in which the magnets have superconducting coils. The Main Injector, a new element of the Run II accelerator complex, is capable of larger proton currents than its predecessor, the Main Ring, enabling a higher rate of anti-proton production.

Anti-Protons are produced by extracting the proton beam from the Main Injector to hit a nickel target, creating a multi-particle spray that contains on average 20 anti-protons per million protons, with a mean kinetic energy of 8 GeV. The anti-protons are then focused by a lithium lens and separated from other particle species by a pulsed magnet.

Then the anti-protons produced in the target are accumulated in the \bar{p} accumulator which actually has two rings. One is for debunching in which a

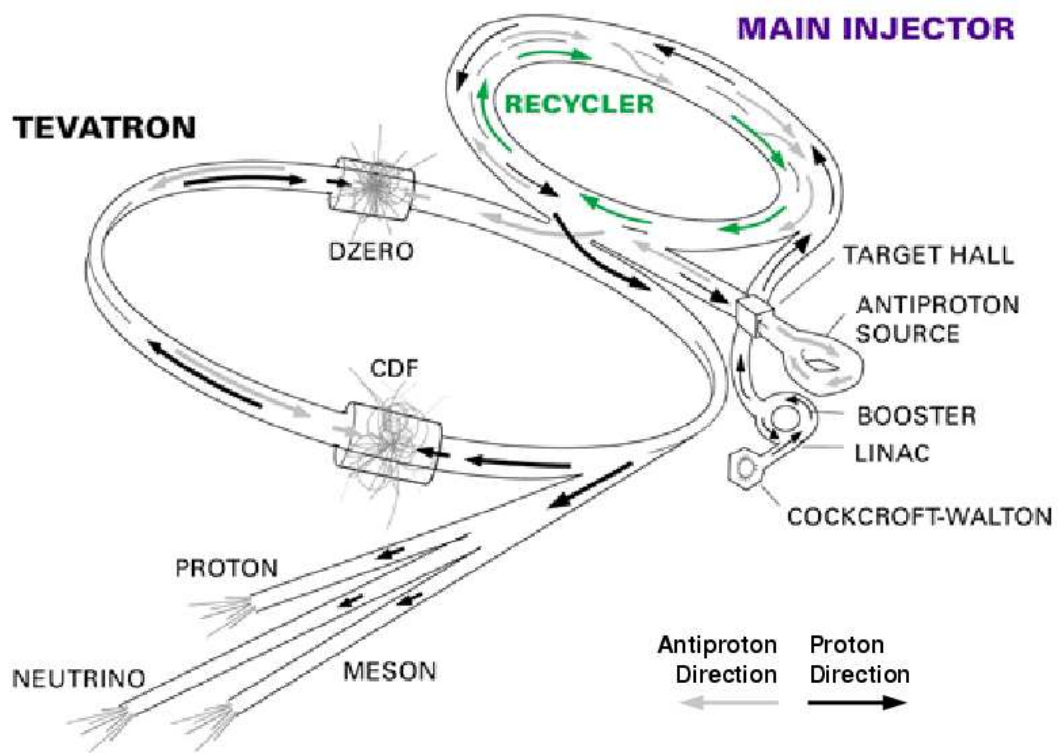


Figure 2.1: Fermilab accelerator complex.

Run	Ib	IIa
protons/bunch	2.3×10^{11}	2.7×10^{11}
anti-proton/bunch	5.5×10^{10}	3.0×10^{10}
total anti-protons	3.3×10^{11}	1.1×10^{12}
proton emittance (mm-mrad)	23π	20π
anti-proton emittance (mm-mrad)	13π	15π
β^*	35	35
anti-proton bunches	6	36
bunch length (m)	0.6	0.37
bunch spacing (ns)	3500	396
interactions/crossing	2.5	2.3

Table 2.1: Parameters describing the accelerator configuration in Run I and II. The Run Ib column shows typical operating parameters during 6×6 bunches. The Run IIa column shows projections for 36×36 operation.

rotation in synchrotron phase space is done to reduce the energy spread at the cost of increasing the time spread of the \bar{p} bunch. After debunching, the \bar{p} 's are added to the circulating beam in the accumulator where stochastic cooling takes place to reduce the random motions of the \bar{p} 's: horizontal, vertical and in synchrotron phase space [36]. When enough anti-protons are circulating in the accumulator ring, they are transferred back into the MI, and are accelerated.

Over a period of 10 to 20 hours, a stack of anti-protons is built up, in preparation for a new store in the Tevatron. At the start of a store, about once per day, 36 bunches of about 3×10^{11} protons and 36 bunches of roughly 3×10^{10} anti-protons are accelerated to 150 GeV by the Main Injector, transferred to the Tevatron – the final stage of Fermilab's accelerator chain. During most of the 2002–2005 run (Run II), the Tevatron was run with “36×36”. This led to an interval between beam crossings of about 396 ns. The 132 ns mode (140×105) is currently under development. The beam collisions continue typically for 8 hours.

In the collider run, protons and anti-protons are injected into Tevatron from opposite directions and accelerated up to 980 GeV. Then they collide with each other. This yields the center-of-mass energy of 1.96 TeV.

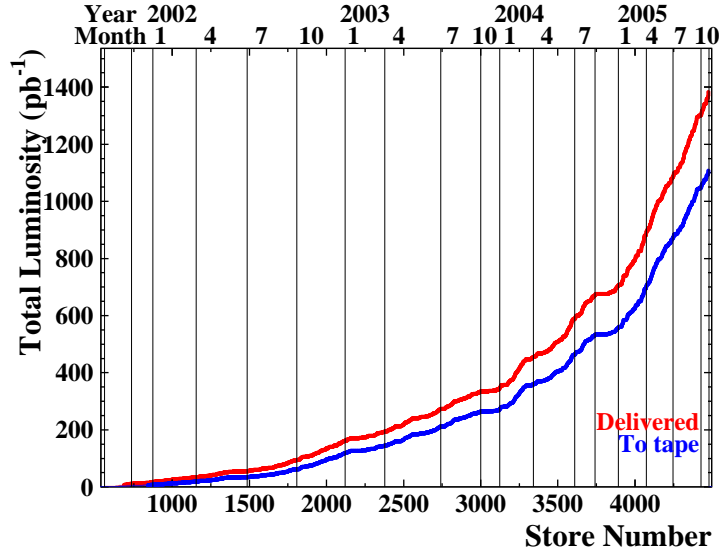


Figure 2.2: Integrated luminosity delivered (upper line) and recorded (lower) at CDF so far, as functions of $p\bar{p}$ stores and time [37]. It began to take physics-quality data at April, 2002.

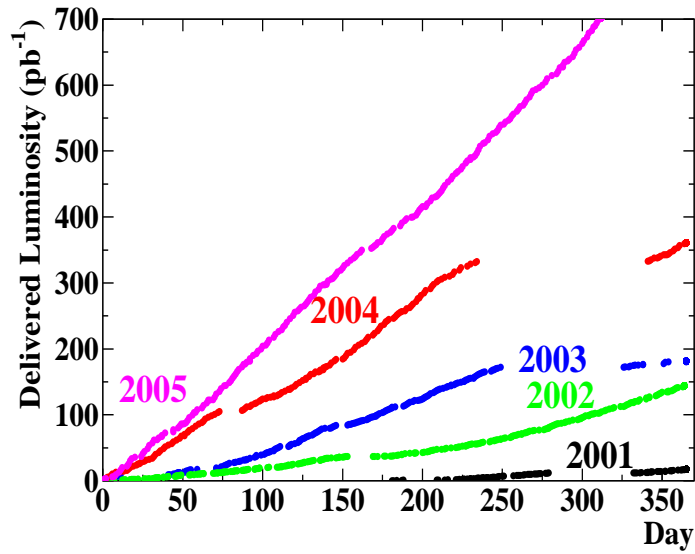


Figure 2.3: The summary of the delivered luminosity at Tevatron so far, as functions of $p\bar{p}$ stores and time. Each line shows luminosity delivered at the same year.

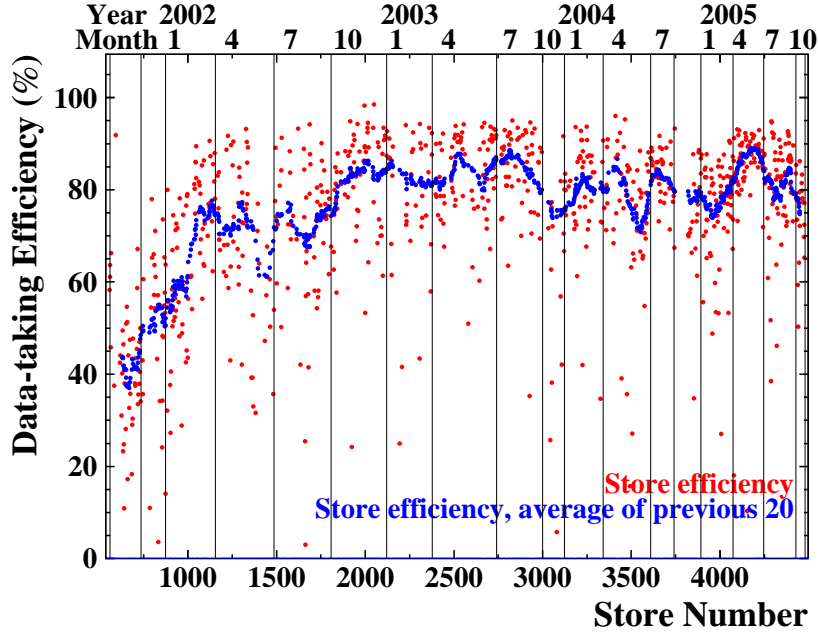


Figure 2.4: Data taking efficiency as functions of $p\bar{p}$ stores and time. It is a level of 80 to 90%. The inefficiency comes from trigger overflow, detector problem, high-voltage reconfiguration and so on.

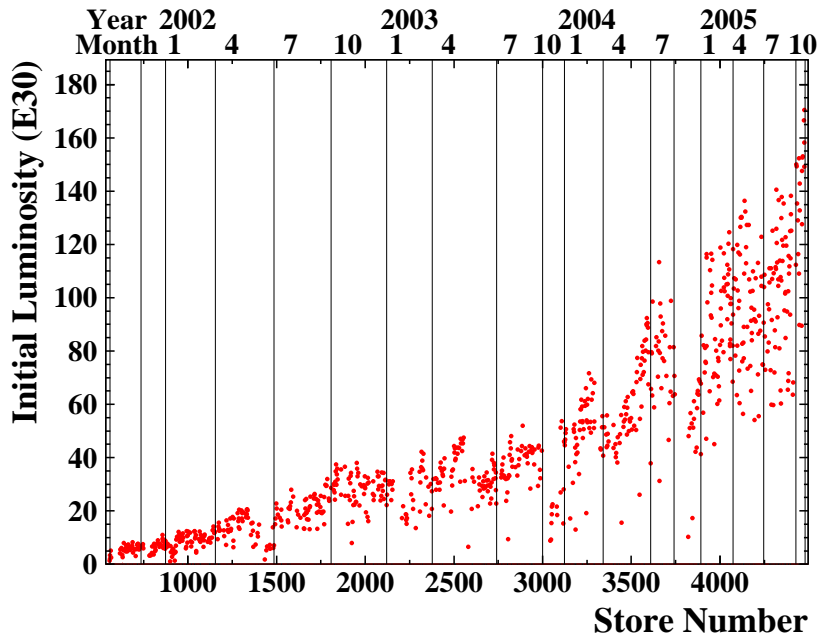


Figure 2.5: The initial instantaneous luminosity as functions of $p\bar{p}$ stores and time. The Tevatron has broken $10^{32} \text{ cm}^{-2} \text{ s}^{-1}$ barrier at October, 2005.

2.2 Collider Detector at Fermilab

The CDF detector is an azimuthally and forward-backward symmetric magnetic detector designed to study $p\bar{p}$ collisions at the Tevatron. It is an general purpose solenoidal detector which combines precision charged particle tracking with fast projective calorimetry and fine grained muon detection. The major function of this detector is to measure the energy, momentum, and, where possible, the identity of the particles produced during the proton-antiproton collision.

Major differences for Run II include : the replacement of the central tracking system; the replacement of a gas sampling calorimeter in the plug-forward region with a scintillating tile calorimeter; preshower detectors; expansion of the muon coverage, a time-of-flight detector and upgrades of trigger, readout electronics, and data acquisition system.

An elevation view of the CDF Run II is shown in Figure 2.7. Tracking systems are contained in a superconducting solenoid, 1.5 m in radius and 4.8 m in length, which generates a 1.4 T magnetic field parallel to the beam axis. Calorimetry and muon systems are all outside the solenoid. The detailed description of the individual detector component can be found in various papers [?]. A schematic drawing of the major detector components is also shown in Figure 2.7.

2.2.1 Detector coordinate system

In the detector coordinate system commonly used at CDF, we choose z axis along the proton beam direction (East) with zero at the detector center, y axis upward and x axis towards outside of the Tevatron ring (North). We use R as the distance to the beam line in cylindrical coordinates; ϕ is the azimuthal angle, and θ is the polar angle relative to the positive z -axis in spherical coordinates. Since hadrons are composite objects, daughter particles from a $p\bar{p}$ collision are often produced with significant momentum along the z axis. It is thus useful to define two variables, rapidity and pseudorapidity:

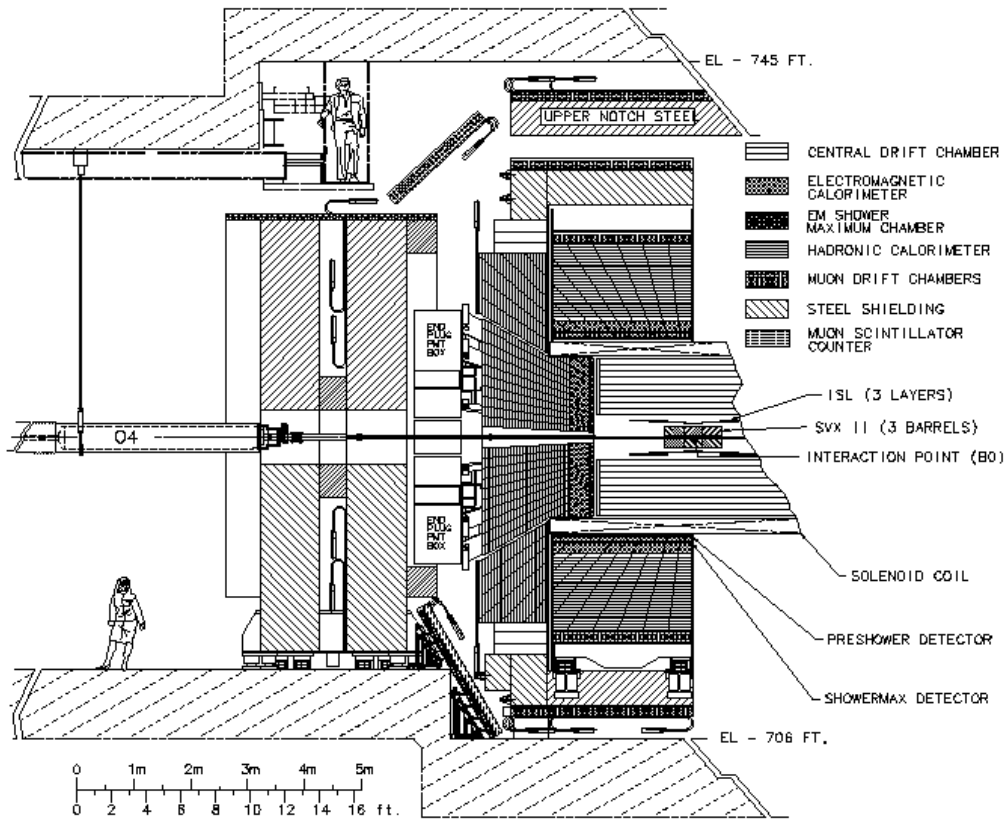


Figure 2.6: Elevation view of one half of the CDF II detector

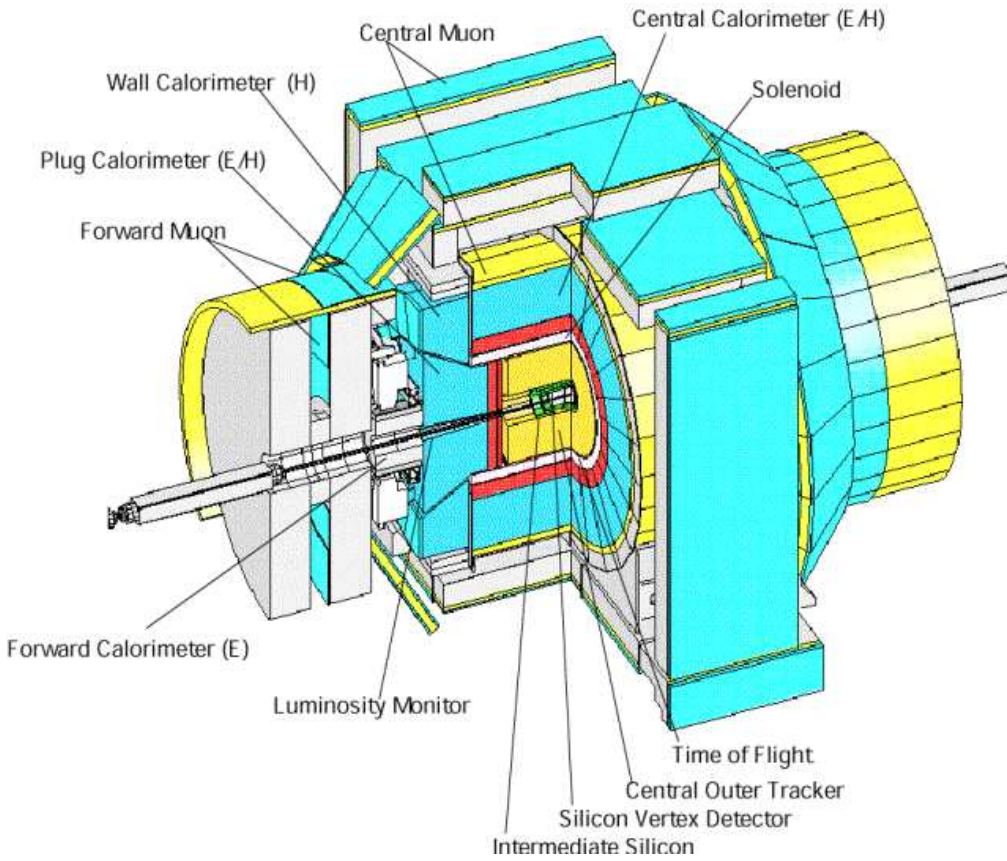


Figure 2.7: A schematic view of the CDF Run II Detector. The solenoid is located between the Central Outer Tracker and the Central Electromagnetic calorimeter. In the central region the existing solenoid and scintillator-based calorimeter were retained from Run I. On each “end” of CDF, the plug and forward ($|\eta| > 1$) calorimeters were replaced with one new end-plug calorimeter.

The rapidity, which is defined as:

$$y = \frac{1}{2} \ln \left(\frac{E + p_z}{E - p_z} \right) \quad (2.3)$$

is often used instead of the polar angle θ in the laboratory coordinate frame. The advantage of rapidity is that a change of rapidity is a constant $\delta y = \theta \equiv \tanh^{-1} \beta$ under a boost in z direction with velocity $\beta \equiv v/c$. For the case where $E \gg m$, the rapidity can be approximated by pseudo-rapidity:

$$\eta = \frac{1}{2} \ln \left(\frac{E + p_z}{E - p_z} \right) = -\ln \left(\tan \frac{\theta}{2} \right) \quad (2.4)$$

The interaction point at CDF is not at the coordinate (0,0,0), however, it is assumed that the reconstructed default track at CDF is from (0,0,0). So the pseudorapidity calculated from default track is called detector pseudorapidity.

$|\eta|$ extends from 0 at the perpendicular to the beampipe to approximately 3.5 at the most forward part of the detector. The central portion of the detector spans $0.0 \lesssim |\eta| \lesssim 1.0$, while the forward (plug) detector is located at $1.0 \lesssim |\eta| \lesssim 3.0$. Sub-detectors are placed radially at varying distances from the collision point. Starting from the beampipe and expanding outward one finds the tracking system, calorimetry systems, and muon systems.

2.2.2 Cerenkov Luminosity Counter

At hadron collider experiments the beam luminosity, traditionally, has been measured using the process of inelastic $p\bar{p}$ scattering. It has a large cross-section, $\sigma_{in} \sim 60$ mb, measured at the Tevatron energy (1.96 TeV) by the CDF, with an uncertainty of $\sim 6\%$. The rate of inelastic $p\bar{p}$ interactions is given by [38]:

$$\mu \cdot f_{BC} = \sigma_{in} \cdot \mathcal{L} \quad (2.5)$$

where \mathcal{L} is the instantaneous luminosity, f_{BC} is the rate of bunch crossing in the Tevatron, μ is the average number of $p\bar{p}$ interactions per bunch crossing.

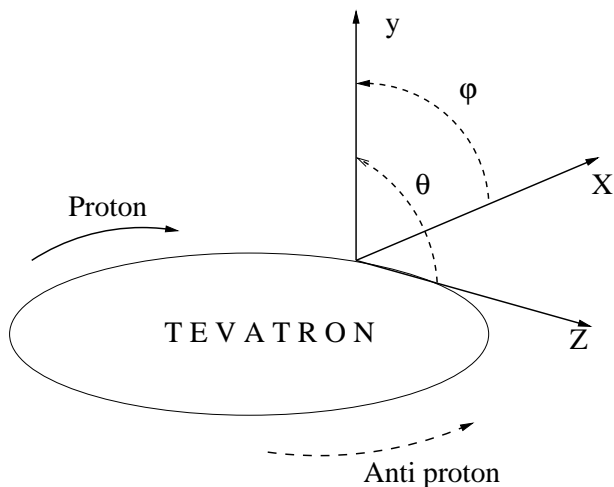


Figure 2.8: The CDF detector coordinate system

To detect inelastic $p\bar{p}$ events¹ efficiently a dedicated detector at small angles, operating at high rate and occupancy, is required. In Run II the Cerenkov Luminosity Counters (CLC) are being used by CDF to measure the Tevatron luminosity. The CLC is designed to measure μ accurately (within a few percent) all the way up to the high luminosity regime $\mathcal{L} \sim 2 \times 10^{32} \text{ cm}^{-2} \text{ s}^{-1}$ expected in Run II [?].

There are two CLC modules in the CDF detector, installed at small angles in the proton (East) and anti-proton (West) directions with rapidity coverage between 3.75 and 4.75. Each module consists of 48 thin, long, gas-filled, Cerenkov counters. The counters are arranged around the beam-pipe in three concentric layers, with 16 counters each, and pointing to the center of the interaction region [39]. The Cerenkov counters are not sensitive to beam halo², photons or neutrons, nor to soft charged particles which fall under the Cerenkov threshold.

¹The CLC has zero acceptance for elastic $p\bar{p}$ events.

²See Reference [40] for a measure of beam halo and losses using the installed arrays of scintillation counters on both sides of the CDF detector.

2.2.3 Tracking System

Detection and tracking of charged particles is the most essential part for B physics analysis. It determines the beam collision point and vertex points of the secondary particles. Generally trackers provide two fundamental kinds of measurement. On one side, they determine the direction and curvature of a particle's path; on the other, they delimit a narrow region where the particle might have been produced. The CDF II tracking system, shown in Figure ??, fulfills both kinds of requirements by combining different detector elements.

There are two primary tracking detector systems in the CDF Run II, inner tracking and outside tracking. The inner tracking system of a 90-cm long silicon micro-strip vertex detector, consisting of one single-sided layer and six double-sided layers, with an additional double-sided layer at large η , surrounds the beam pipe [41]. Outside the silicon detector, a 3.1 meter long drift chamber with 96 layers of sense wires, the Central Outer Tracker (COT), is used with the silicon detector to determine the momenta of charged particles and the z position of the $p\bar{p}$ interaction (z_{vertex}) [42].

Charged particle moving in a uniform magnetic field, as inside the CDF tracker, have a helicoidal trajectory. By measuring the radius of curvature of the helix, one obtains the particle's transverse momentum; the longitudinal momentum is related to the helix pitch. This information can be used in several ways: as a requirement in a trigger, during particle identification, in order to calibrate the calorimeters.

To obtain a precise measurement of the helix radius and pitch, it is necessary to sample points of the trajectory which are spread on a long lever arm. Therefore, a good spectrometer requires a large tracking volume. On the other hand, by taking a few, very accurate measurements of the track position near the primary interaction point, it is possible to narrow the region of space in which a given particle was originated. By intersecting such regions, it is possible to determine which (if any) particles were produced in a secondary vertex, trigger on their existence, and measure the mass and lifetime of short-lived particles.

Helix parametrization

Within an axial and almost uniform magnetic field \vec{B} , such as the one inside the CDF solenoid, charged particles are subjected to the Lorentz force

$$\vec{F} = qe\vec{v} \times \vec{B} \quad (2.6)$$

and move along helices of radius

$$r = \left| \frac{p_T}{qeB} \right| \quad (2.7)$$

At CDF, such helices are described with the following parameters.

$\cot \theta$: cotangent of the polar angle at minimum approach

c : curvature of the helix (inverse of diameter), with the same sign as the particle charge

z_0 : z coordinate at minimum approach

d : minimum distance between the helix and the detector axis, impact parameter

ϕ_0 : azimuthal direction of the track at minimum approach

The term “minimum approach” refers to the point of the helix which lies closest to the detector axis, in the proximity of the origin.

The purpose of the tracking system is to find tracks, and to associate to each track the best estimate of its parameters c, d, ϕ_0, z_0 and $\cot \theta$.

Central Outer Tracker

The Central Outer Tracker (COT) is an open-cell drift chamber, which fills the volume between radial coordinates of 40 and 138 cm, up to a $|z|$ of 155 cm. with its long lever arm, it provides an accurate measurement of track curvature, ϕ_0 and $\cot \theta$. The COT surrounds the silicon detector and extends to a radius

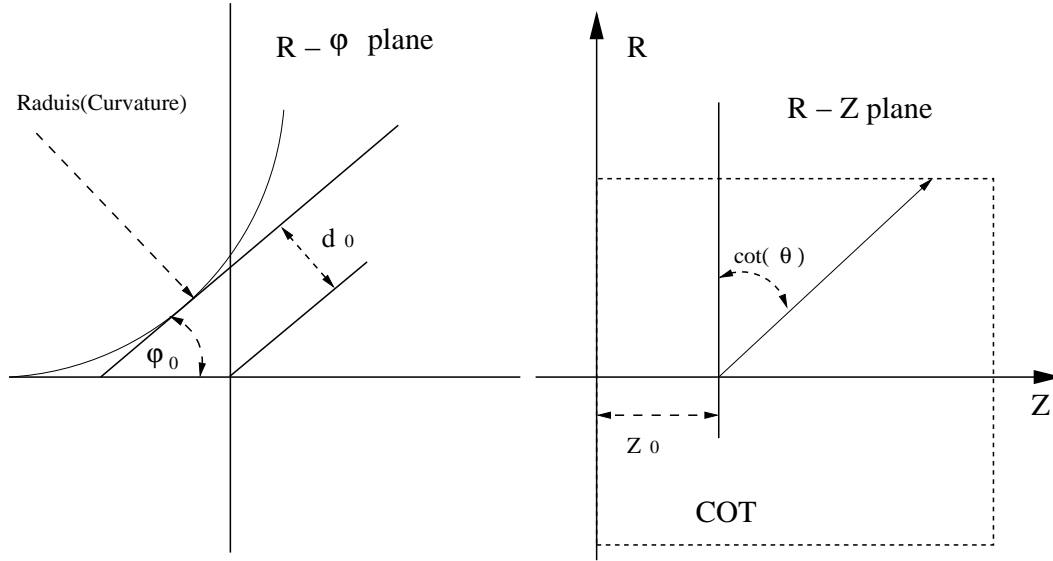


Figure 2.9: The schematic trajectory of a charged particle. It shows the helix parameters to describe track trajectory mathematically.

just inside of the Time-of-Flight system. The inner and outer walls of the COT cylinder are made of 0.25 in aluminum sheet with the inner radius at 0.4 m. The tracking volume is divided in eight superlayers(SL), each containing twelve layers of sense wires. Axial superlayers, in which wires are parallel to the magnetic field, alternate with superlayers in which the wires have a 3° stereo angle. Each superlayer is divided in identical cell and cells are delimited by two field panels, made of gold-coated Mylar, and two shaper panels, which are Mylar with two field-shaping panels attached. A cell contains twenty five gold-plated copper-beryllium wires with $51\mu\text{m}$. They alternate between potential and sense wires. The wire spacing is about 7.5 mm in all SL. COT contains total 30,240 sense wires that run the length(in z) of the chamber between two end plates. Each wire is strung between the two endplates with a tension of 1.3 N, giving a total load on the endplates of 40 tons from all of the wires. At the center of COT, a mylar wire support is epoxied to all of the sense and potential wires to provide additional electrostatic stability. The spacing between wires and the field sheets is just under 1 cm and varies slightly between SL. In an axial layer, the wires and fieldplanes are parallel to the z axis, and thus provide

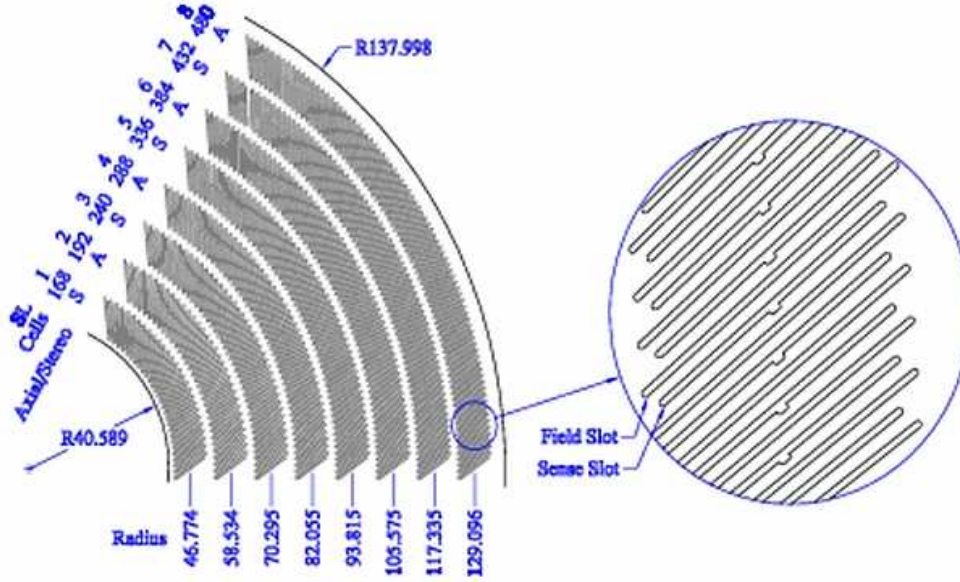


Figure 2.10: Schematic view of COT endplate. Slots for field plates and wire planes alternate.

only $r - \phi$ information. In stereo layers, a given wireplane or field sheet which starts at a slot in one endplate is offset by 6 cells. This generates a stereo angle of 3° which gives z axis information.

The design of three cells from SL2 is shown in Figure 2.11 and Table 2.2 summarize the COT geometry. Ar-Ethane gas(60 : 40 mixture) fills the active chamber volume and both provides a source of ionized electrons and defines the drift velocity. When a charged particle passes through , the mixed gas is ionized and produce electrons. The electrons drift towards the same sense wires, resulting in an avalanche at the wire surface, which provides a gain of $\sim 10^4$. The charge of ionized electrons is used in the measurement of dE/dX , for particle identification. Due to the magnetic field, the electrons drift with a Lorentz angle of $\sim 35^\circ$. It is the reason that the cells are tilted with respect to the radial direction with the same Lorentz angle.

The voltage on the wire plane is set in order to insure a maximum drift time, about 100 ns which is less than the time between beam crossing time which is currently 396 ns. The drift time resolution is better than 2 ns giving

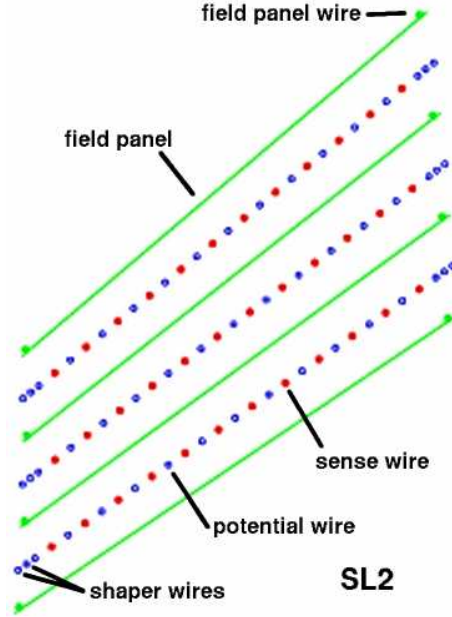


Figure 2.11: Nominal cell layout for SL2. Other superlayers are similar.

a single hit resolution of $150 \mu\text{m}$. This hit resolution combined with the large lever arm, give the COT a momentum resolution of

$$\frac{\sigma_{p_T}}{p_T^2} = 0.15\% \text{ GeV}/c \quad (2.8)$$

Silicon Tracking System

The CDF Run II silicon tracking system provides a decay position and a trajectory for charged particles with an extremely high precision. It has proven to be an excellent tool for top search and for b physics since the CDF Run I experiment. The primary goal of the silicon tracking system is to reconstruct tracks for use in the pattern recognition of displaced secondary vertices from the beam collision position. These secondary vertices are created from the decay of long lived particles and provide a very good background rejection power in the identification of charm and beauty hadrons.

Silicon tracking system consists of eight layers of microstrip silicon detec-

Superlayer	Average r	Stereo angle	# cells	# sense wires
1	46 cm	$+3^\circ$	168	2016
2	59 cm	0	192	2304
3	70 cm	-3°	240	2880
4	82 cm	0	288	3456
5	94 cm	$+3^\circ$	336	4032
6	106 cm	0	384	4068
7	119 cm	-3°	432	5184
8	131 cm	0	480	5760
Axial total			1344	16128
Stereo total			1176	14112
Overall			2520	30240

Table 2.2: Central Outer Tracker geometry

tor on wafer, placed in a range between 1.135 and 30 cm from the beam axis. It provides accurate, three-dimensional vertexing measurements by measuring the d and z_0 parameters of charged tracks and also extends the tracking coverage of CDF from the COT limit($|\eta| < 1$) to $|\eta| < 2$. The tracker is divided, in three concentric subsystems : Layer00, SVXII and ISL(intermediate silicon layers).

Microstrip silicon detectors are based on inversely polarized $p-n$ junctions. If a charged particle crosses the detector, electron-hole pairs are released by ionization, and drift towards the surface. By segmenting the surface into p^+ (or n^+) strips, which are capacitively coupled to conductive strips, the position of the ionizing particle can be measured along an axis orthogonal to the segments.

All of the ISL wafers and two of those in SVXII are double-sided, with axial strips on the p side and small-angle stereo (SAS) strips on the n side, which form an angle of $\pm 1.2^\circ$ with the detector axis. Three layers of SVXII consist of double-sided wafer whose n-strip from an angle of 90° with the axial direction. Orthogonal strips provide a very accurate measurement of z coordinate. By using both SAS and 90° wafers 3D vertexing resolution is improved dramatically. Lastly, L00, being placed extremely close to the interaction point, is built of radiation-hard, single-sided microstrip wafers.

	Layer	Active width (cm)	Wedge A radius (cm)	Wedge B radius (cm)	Type
Layer00	0	0.64(A) 1.28(B)	1.35	1.62	Axial only
SVX II	1	1.536	2.995	2.545	90°
	2	2.3038	4.57	4.12	90°
	3	3.84	7.02	6.52	Stereo -
	4	4.608	8.72	8.22	90°
	5	5.824	10.645	10.095	Stereo +
ISL	6c	2×5.73	23.1	22.6	Stereo -
	6f	2×5.73	20.2	19.7	Stereo -
	7f	2×5.73	29	28.6	Stereo +

Table 2.3: Silicon tracker geometry. L00 wafers have different widths in ϕ wedges A and B. ISL geometry is reported for the central(c) region ($|\eta| < 1$), where layer 7 is absent, and forward(f) region. Radii are measured at the center of the wafer.

Silicon wafers in L00 and SVXII are arranged on twelve azimuthal wedges. In the region $1 < |\eta| < 2$, the inner layer of ISL is divided in 24 wedges, while the outer layer forms 36 wedges; 28 wedges forms a single ISL layers in the central region ($|\eta| < 1$). Without ISL and L00, SVX II reaches a impact parameter resolution of $\sim 40 \mu\text{m}$ which includes the $25 - 30 \mu\text{m}$ contribution from the transverse size of the beamline. Table 2.3 shows the summary of the CDF Run II silicon tracker geometry.

Track reconstruction

Track reconstruction begins in the outer tracking chamber - the COT. The first step in track reconstruction is to form line segment from hits in each superlayer in the COT. Line segment from the axial layers which are consistent with lying tangent to a common circle are linked together to form a track. A two dimensional track fit is performed on $R - \phi$ plane. Line segment in stereo layers are then linked to the 2D track, then finally a helix fit is performed.

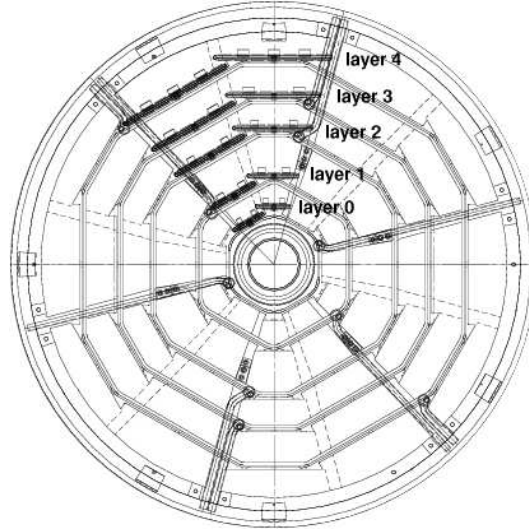


Figure 2.12: SVX bulkhead, end view. it shows two wedges installed.

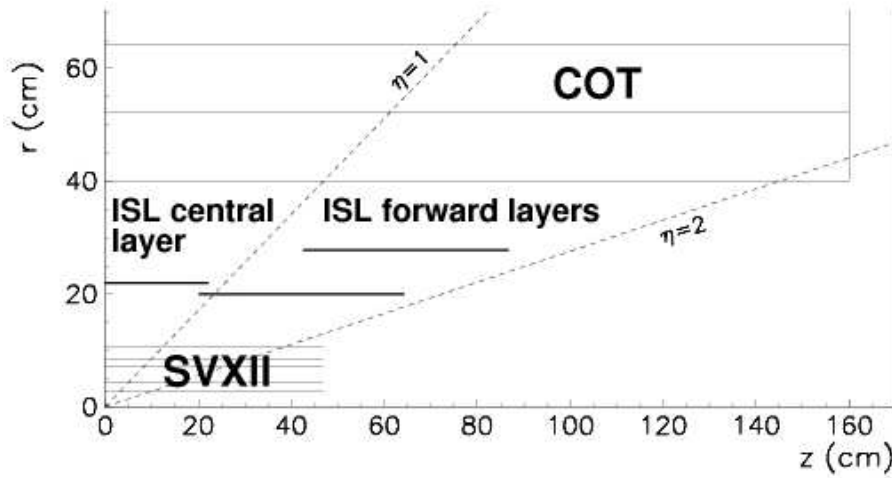


Figure 2.13: .

Schematic view of CDF tracking system. η coverage of each tracking system is shown.

The next step is to extrapolate the track reconstructed in COT into the silicon tracking system. It starts in the outermost layer of the silicon tracker. A road, or window around the track is established based on the errors on the COT track parameters. If hits lie within the road, they are added to the track. A new track fit is then performed, resulting in a new error matrix and a new road. This road is then used to add hits from the next silicon layer. This procedure is repeated until there are no layers left. There may be multiple tracks with different combinations of silicon hit associated with one COT track. In this case, the track with the largest number of silicon hits is chosen.

2.2.4 Time-of-Flight

Right outside of tracking systems, there is the Time-Of-Flight (TOF) detector which measures the flight time of particles. The TOF detector newly has been added to the CDF II detector to enhance the particle identification [45]. It is very useful for particle identification in low momentum region. Figure 2.14 shows the separation power as a function of momentum for each particle.

The time-of-flight of the particle is defined to be the difference between the arrival time at the TOF scintillator and the collision time t_0 . Similarly, the path length L of the particle is calculated in between the scintillator and the beam collision point. Using this information and the momentum of the particle, the mass of the particle is given in formula below,

$$m = \frac{p}{c} \sqrt{\left(\frac{ct}{L}\right)^2 - 1} \quad (2.9)$$

Figure 2.15 shows the charged particle mass calculated given formula with TOF information.

The primary goal is to provide a 2σ separation between π^\pm and K^\pm for momentum $p < 1.6 \text{ GeV}/c^2$. By combining it with dE/dx it is expected to improve the neutral B meson flavor determination. Another purpose of TOF detector is to search for highly ionizing particle-monopole [46]. Since the mass

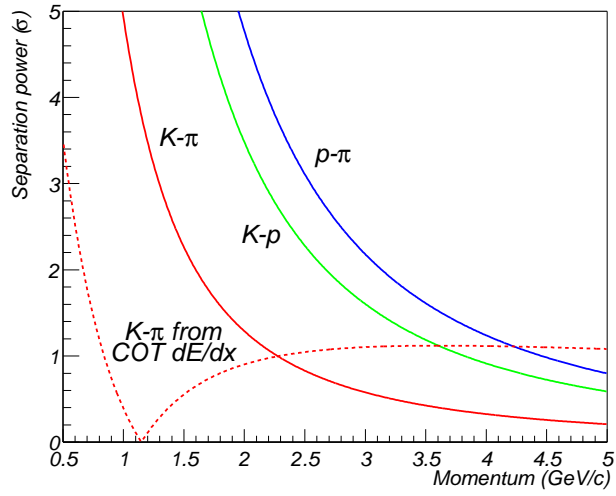


Figure 2.14: The separation power as a function of momentum between K/π , p/π , and K/p traversing a distance of 140 cm, expressed in separation power assuming a resolution of 100 ps. The dashed line shows the K/π separation power from the dE/dX measurement in the COT.

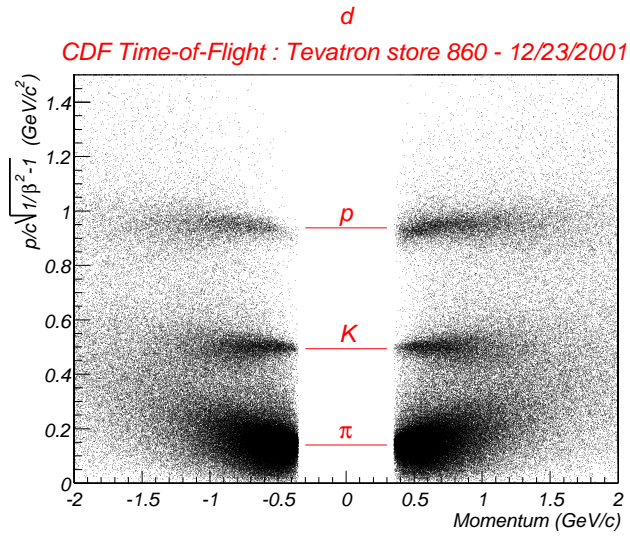


Figure 2.15: The TOF performance plot. the mass of charged particles are calculated with TOF information. Positively charge tracks are on the right, negative tracks are on the left.

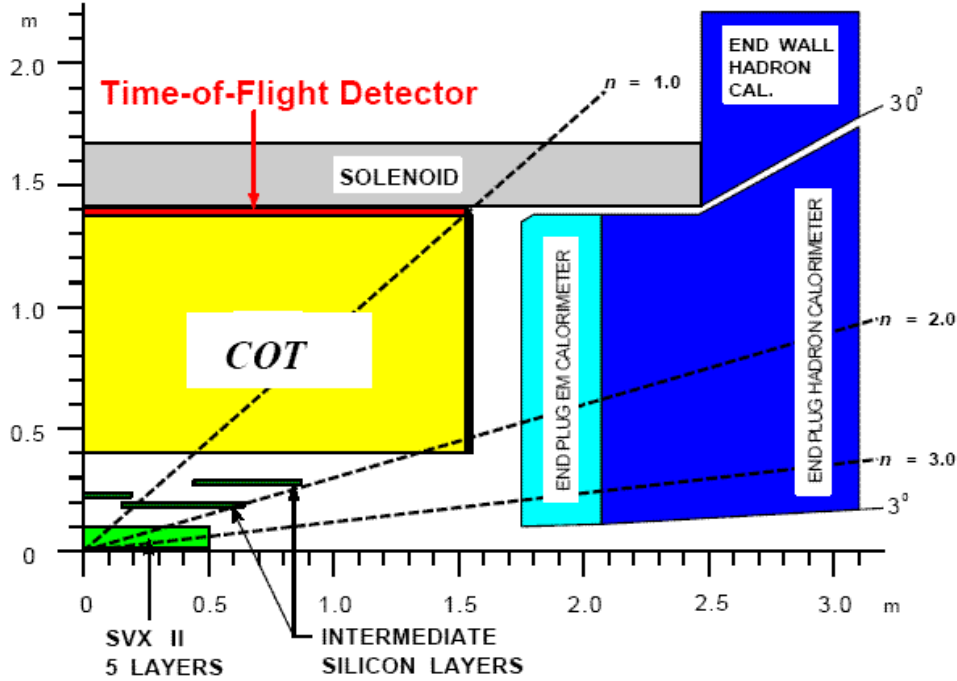


Figure 2.16: Side view of the central region of the CDF II detector (quarter section), showing the Tracking System which is cylindrically symmetric. Layer 00 is missing from the illustration.

difference between pion and proton is even bigger than the difference between pion and Kaon, the particle identification ability of selecting proton from pion by combining TOF and dE/dx together is very powerful in b physics.

2.2.5 Superconducting Solenoid Coil

The superconducting solenoid magnet coil is made of an aluminum-stabilized NbTi/Cu superconductor. It provides a uniform 1.41 T magnetic field along the incident beam direction in the COT region.

The CDF calorimeter systems are located outside the solenoid with two separated devices of the electromagnetic (EM) and hadronic (HA) calorimeters where hadron, electron, photon deposit most of their energy. This is useful to identify electrons and photons. Unlike hadrons and electrons, muons

only deposit minimum ionization energy in the calorimeters, so muon system outside the calorimeter is used to identify muon. In addition, there are the Central Pre-Radiator (CPR) and Central Electromagnetic Strip (CES) chambers. Both CPR and CES are used to discriminate between a signal photon and background from a neutral pion decay to $\gamma\gamma$.

2.2.6 Calorimeters

Calorimetry has played a crucial role in the physics CDF has produced: the top mass discovery, the precision measurement of the W mass, photon and jet measurements over many orders of magnitude, and searches for new phenomena have all exploited the excellent behavior of the calorimeters. In the upgraded detector the existing scintillator-based calorimeter was retained within central region, but its electronics needed to be replaced due to the shorter bunch spacing. On each “end” of CDF, the plug and forward ($|\eta| > 1$) calorimeters were replaced with one new end-plug calorimeter. The system promises an exceptional increase in compactness, hermiticity, radiation hardness, and speed over the present system.

The solenoid and tracking volumes of CDF are surrounded by calorimeters, which cover 2π in azimuth and $|\eta| \leq 3.6$. The central electromagnetic (CEM) calorimeter covers $|\eta| \leq 1.1$ and is followed at a larger radius by the central hadronic calorimeters (CHA and WHA), which cover $|\eta| \leq 1.3$. These calorimeter use scintillator as the active medium. The CEM absorber is lead and the CHA/WHA absorber is iron. The calorimeters are segmented into units of 15 degrees in azimuth and 0.1 pseudorapidity. Two phototubes bracket each tower in ϕ , the average of the energy in the two tubes is used to determine the ϕ position of energy deposited in a tower.

The calorimeter is made up of wedges, or “physical towers”, measured in $\eta - \phi$ coordinates. Each tower uses a series of absorber and scintillator layers. Scintillator light is collected by a light pipe and a wavelength shifter that directs the energy into a photomultiplier tube (PMT). An $r - z$ view of the detector shows the calorimeter wedges arranged as if a ϕ cut into slices, with

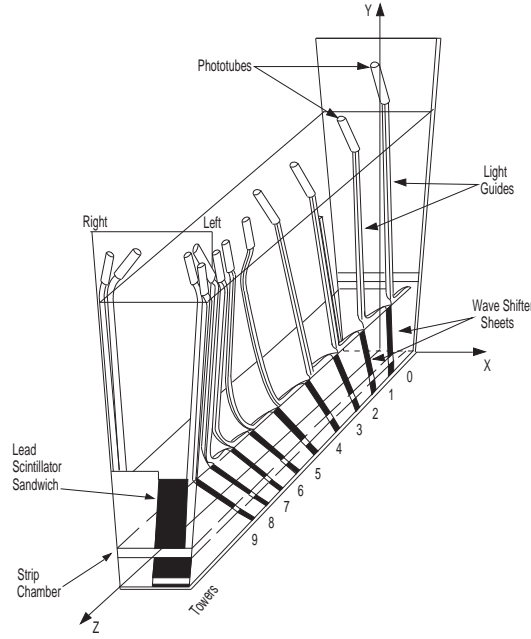


Figure 2.17: Schematic view of the wedge module of the central electromagnetic calorimeter.

each slice pointing back toward the interaction point. The central portion of the calorimeter has towers that span 15° in ϕ and 0.11 in units of η , while plug calorimeter towers span either 15° or 7.5° in ϕ , and varying ranges in η .

The CEM uses a hybrid design. It consists of the lead and scintillator layers with an embedded strip chamber approximately at the depth of maximum particle multiplicity for electromagnetic showers. The scintillator provides a good energy resolution and the strip chamber provides the position determination and transverse development at the shower maximum. The average energy resolution of the CEM is

$$\frac{\sigma(E)}{E} = \frac{13.5\%}{\sqrt{E_T}} \oplus 2\% \text{ (added in quadrature)}, \quad (2.10)$$

where $E_T = E \cdot \sin\theta$ (E in GeV).

The CHA and WHA are made of steel and scintillator. The interaction length of both the CHA and WHA is $4.5 \lambda_0$. The CHA has 32 layers with 2.5 cm sampling, and the WHA has 15 layers with 5.0 cm sampling.

For hadrons, the single-particle resolution depends on angle and varies from roughly $50\%/\sqrt{E}$ plus 3% added in quadrature in the CHA to $75\%/\sqrt{E}$ plus 4% added in quadrature in the WHA.

For Run II, there is new plug calorimeter, with variable tower size, which extends coverage out to $|\eta| = 3.6$. The plug electromagnetic calorimeter (PEM) covers both ends of the superconducting magnet coil. Each of them are made of four quadrants of $\delta\phi = 90^\circ$. And each of the quadrants consists of 34 layers of proportional tube arrays interleaved with 2.7 mm thick lead absorber panel filling about 50 cm in depth. The plug hadronic calorimeter (PHA) has 20 layers of steel and proportional tubes. Each energy resolution of PEM and PHA is about 16% and 80%. The PEM contains an embedded position detector at shower maximum to improve electron identification and π^0/γ separation. In addition, the first layer of the PEM may be read out separately as a pre-shower detector.

2.2.7 The Central Preradiator & Central Shower Maximum Detector

The central calorimeter is segmented into 48 independent wedge modules. The full central detector is constructed of two rings of 24 wedges each that make contact at $z = 0$. Each wedge subtends 15° in azimuth and approximately one unit in η . Both CPR and CES chambers are segmented into two halves in CDF z coordinates.

A system of proportional wire chambers in front of the central electromagnetic calorimeters (the CPR system) uses the one-radiation-length-thick magnet coil as a ‘preradiator’ to determine whether showers start before the calorimeter [47]. Wire chambers with cathode strip readout (the CES system), located at shower maximum in the central electromagnetic calorimeter, give 2-dimensional profiles of showers.

The CPR chambers’ perpendicular distance to beam line is 168 cm. Inside each CPR chamber the wires running along z directions are split about the middle of z . They are 16 wires at low $|z|$ ($7.9 \sim 119.7$ cm), and 16 at high $|z|$

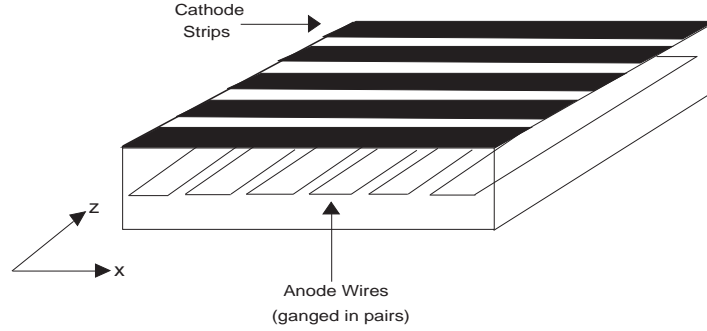


Figure 2.18: Schematic view of CES.

(123.5 \sim 235.3 cm) for a total of 32 in one wedge.

The CES chambers' perpendicular distance to beam line is 184 cm. The CES anode wires measure ϕ and cathode strips measure η . Inside each chamber the wires running along z directions are split in the middle in z (121.2 cm). They are 32 wires at low $|z|$ (0.2 \sim 121.2 cm), and 32 at high $|z|$ (121.2 \sim 239.6 cm) for a total of 64 in one wedge. The strips are slightly different pitch in low and high $|z|$. There are the 69 z strips at low $|z|$ and 59 at high.

2.2.8 Muon Chambers

The muon detectors are located outside of the calorimeter, at the furthest reaches of the detector. Muons are minimum ionizing particles, which means they are capable of travelling through many interaction lengths before losing their energy and stopping.

CDF uses the steel in the calorimeter, the magnet return yoke, and additional steel shielding to stop all other charged particles from entering the muon detectors. The muon chambers record hits from the path of the muon through the detector. This information, combined with tracks in the COT, results in an excellent muon identification, as well as, rejection of cosmic background.

The muon detectors are four systems of scintillators and proportional wire chambers which extend out to $|\eta| \leq 1.5$. They are, moving outward from the

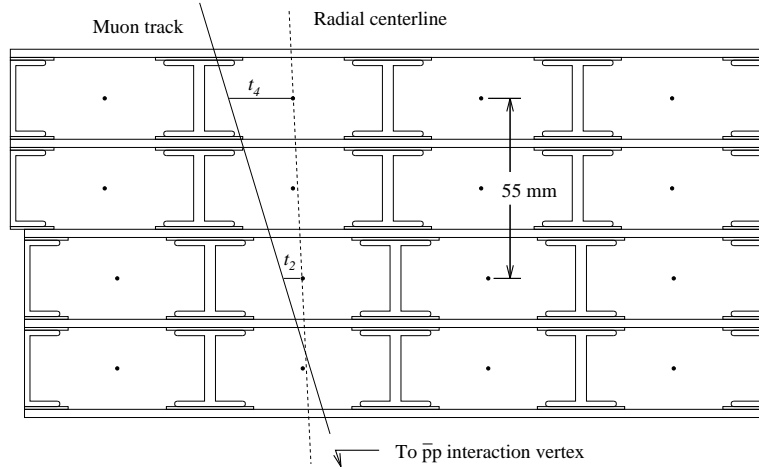


Figure 2.19: Cross section of a CMU module. Each module contains 4 layers of 4 rectangular drift cells.

interaction point: central muon (CMU), central muon upgrade (CMP), central muon extensions (CMX/CSX), and barrel muon detector (BMU) detectors. The BMU is newly installed for CDF Run II experiment.

CMU

The CMU is located around the outside of the central hadron calorimeter at a radial distance of 3470 mm from the beam axis. It covers $|\eta| < 0.6$ region. The muon detector is segmented in ϕ into 12.6° wedges which fit into the top of each central calorimeter wedge. This leaves a gap in the central muon coverage of 2.4° between each wedge. The three modules are bolted together at each end to form a single unit. This single unit is suspended from the top of the calorimeter wedge. Figure 2.19 shows the location of the central muon chamber. Each of the three modules in a wedge consists of four layers of four rectangular drift cell. A diagram of one module is shown in Figure 2.20.

CMP

The CMP covers $|\eta| < 0.6$. It provides confirmation for tracks from CMU but with reduced non-muon (hadronic) background. It consists of 4 layers of

single-wire drift cells installed outside of 2 feet of additional steel to reduce the non-muon background. The drift cells are rectangular with cross-sectional dimensions of $2.5 \text{ cm} \times 15 \text{ cm}$.

CMX

The CMX is an extension to the central muon detector to cover $0.6 < |\eta| < 1.0$. It consists of a conical arrangement of drift tubes and scintillation counters, which are used to reject background based on timing information. The drift cell differ from those of the CMP only in length. They are arranged in azimuthal sections with 15° azimuthal angle. Each wedge has 8 layers of rectangular tubes in radial direction and 6 cells neighbor in each other in ϕ . The 8 layers are grouped in pairs to form 4 continuous layers, each of which is half-staggered with respect to each other. The layout of CMX is given in Figure 2.20.

BMU

The barrel muon detector is newly installed for the CDF Run II. It covers $1.0 < |\eta| < 1.5$. Three-quarters of the azimuth is instrumented. The chambers are 11.9 feet long, 1 inch deep, and 3.3 inches wide, with each chamber covering 1.25° in azimuth. The chambers are stacked four high radially, with the second and fourth stacks staggered azimuthally by a half-cell relative to the first and third.

The rapidity coverage of the muon detectors are summarized as following:

- The CMU and CMP extend out to $|\eta|$ of 0.6.
- The CMX spans a range of $0.6 < |\eta| < 1.0$.
- The BMU finalizes the coverage from $1.0 < |\eta| < 1.5$.

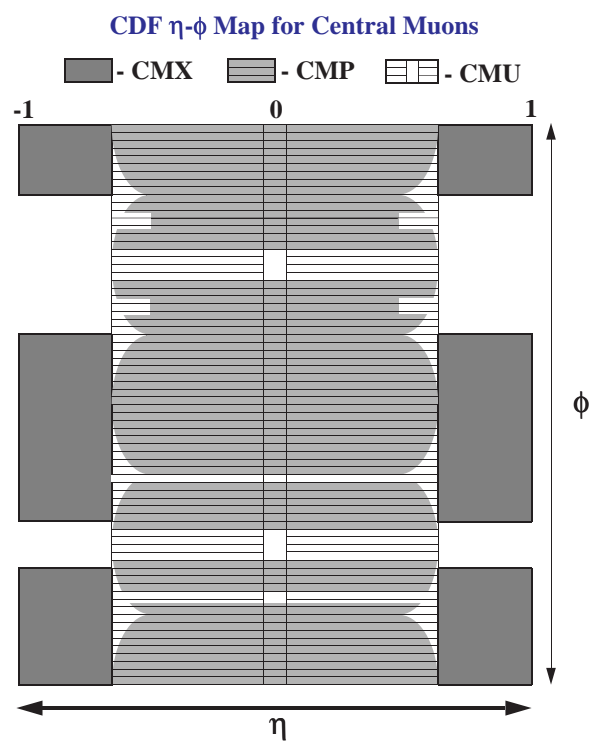


Figure 2.20: The coverage of muon system. CMU, CMP and CMX coverage are hatched.

2.3 Trigger and data acquisition systems

The trigger system is the important component for detector at hadron collider. It is impossible to record all events produced during the $p\bar{p}$ collisions. A typical event size is 250 kB. At the 2.5 MHz beam crossing rate, the system would have to be capable of recording 625 GB/s. This is assuming that there is an interaction every beam crossing, which is not unreasonable, described as an average of 2.3 interactions per crossing in Table 2.1.

We are interested in events containing particles with large transverse energy. This reflects hard scattering of quarks in the protons and anti-protons. The uninteresting inelastic events, called “minimum bias”, occur ten orders of magnitude more frequently than $t\bar{t}$ events, and four order of magnitude more often than events with b ’s. Currently, the maximum event rate to disk is ≈ 70 Hz. If events were selected randomly, we would have no chance of acquiring interesting data samples large enough to make precise measurements or to approach new physics.

The complex system of digital electronics called the trigger allows the experiment to decide, in a very short amount of time, whether an event is interesting enough to record or not. It is of the utmost importance that the decision is fast, so that collisions are not missed while the trigger is thinking about its decision.

There are three trigger paths at CDF trigger system so that a data acquisition system (DAQ) efficiently consumes the collision events within a 132 ns bunch-crossing rate.³ Since all the events cannot be stored, only the interesting events are selected by triggers. In each trigger step, the data size is reduced according to that triggering ability: 40 kHz acceptable rate at Level-1, 300 Hz for Level-2, and 30-50 Hz at Level-3 trigger stage.

Figure 2.21 shows the functional block diagram of the readout electronics. To accommodate a 132 ns bunch-crossing time and a 4 μ s decision time for the

³In the period of data taking considered in this analysis, the accelerator was operating in 35 bunches mode (beam crossing interval of 396 ns) and the trigger was clocked every 132 ns with the two intermediate clock cycles automatically rejected.

first trigger level, all front-end electronics are fully pipelined, with on-board buffering for 42 beam crossings. Data from the calorimeters, the central tracking chamber, and the muon detectors are sent to the Level-1 trigger system, which determines whether a $p\bar{p}$ collision is sufficiently interesting to hold the data for the Level-2 trigger hardware. See Figure 2.22 for details. The Level-1 trigger is a synchronous system with a decision reaching each front-end card at the end of 42-crossing pipeline. Upon a Level-1 trigger accept, the data on each front-end card are transferred to one of four local Level-2 buffers. The second trigger level is an asynchronous system with an average decision time of 20 μ s. A Level-2 trigger accept flags an event for readout. Data are collected in DAQ buffers and then transferred via a network switch to a Level-3 CPU node, where the complete event is assembled, analysed, and, if accepted, written out to permanent storage. These events can also be viewed by online monitoring programs running on other workstations.

All events accepted by Level-2 trigger are collected in the Event Builder (EVB), and then the EVB assembles those event fragments into one data block and delivers it to the Level-3 trigger system. The Level-3 trigger system is a farm of parallel processors which operate on a Linux PC, where a full event reconstruction is implemented in software. After passing through the Level-3 trigger, the Data Logger system delivers events to the tape device or online monitoring processes. The Level-3 reconstruction program is written in C++ with object-oriented techniques. The same reconstruction program is used in the offline event analysis.

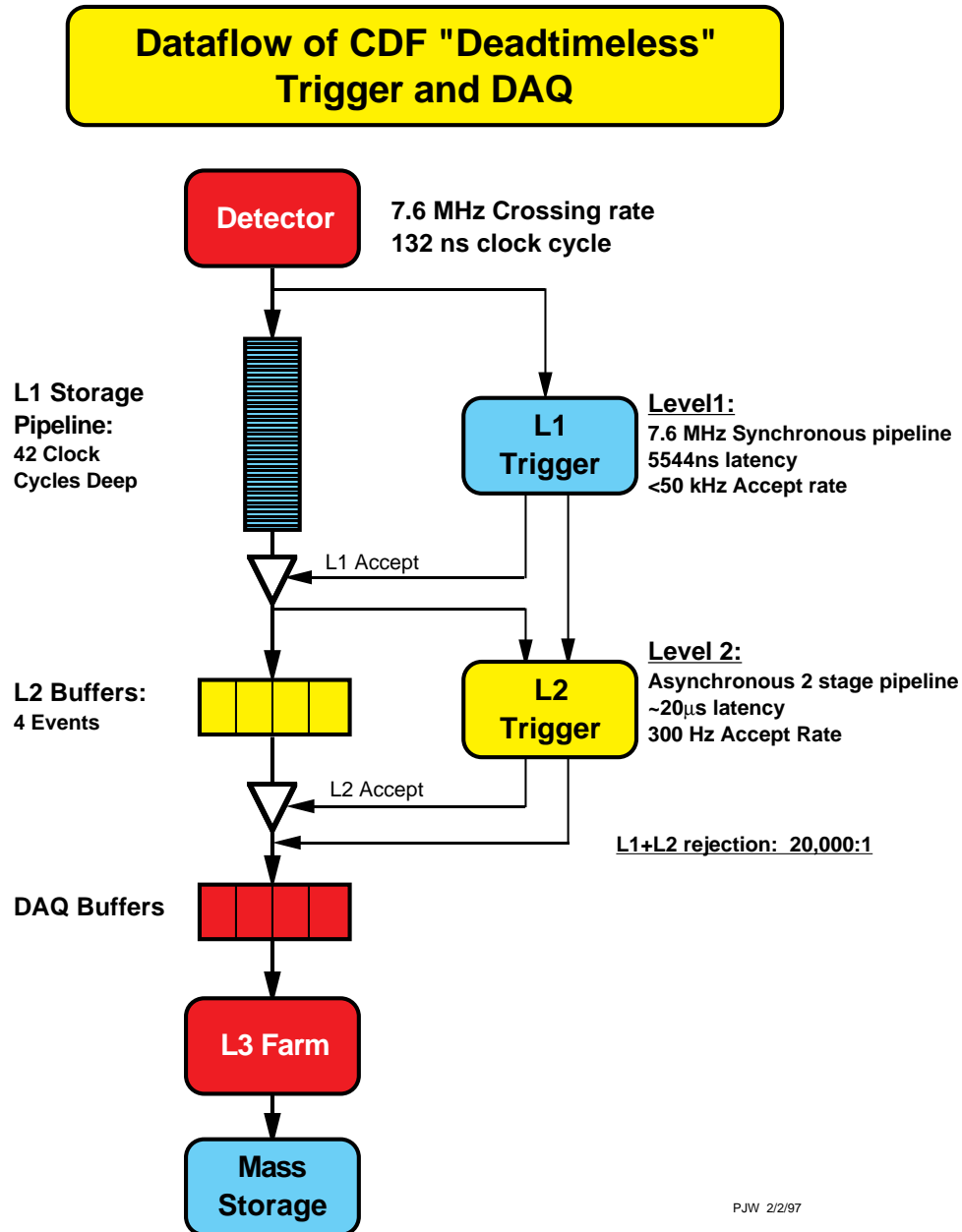
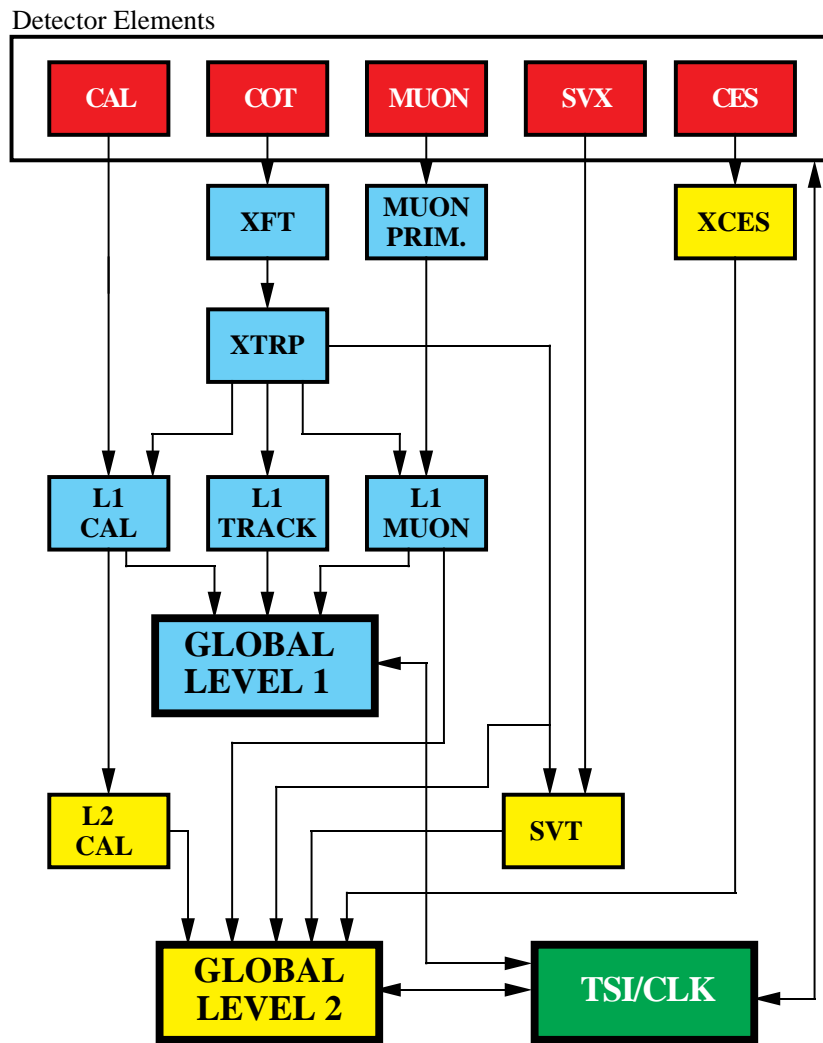


Figure 2.21: Trigger System Flowchart for CDF. This diagram shows the maximum rate which the trigger system was designed to handle. We are currently running at a 2.5 MHz input rate into Level-1, and a 20 kHz output rate from Level-1.

RUN II TRIGGER SYSTEM



PJW 9/23/96

Figure 2.22: Block diagram of the Run II trigger system at CDF.

Chapter 3

Data Samples and Selection Cuts

3.1 Data Samples

The dataset used for this analysis is the J/ψ samples, xpmmm0d dataset, and the reconstruction is based on cdfsoft version 5.3.1. The total integrated luminosity corresponds to about 360 pb^{-1} , with run range of $138425 \sim 185517$. The data were accumulated in the period of February, 2003 to July, 2004. The GoodRun bits are required. A run is considered to be good for a specific analysis if all relevant detector systems operated normally during this run as determined by the experts. The particular good run definition used in the current analysis. we use new COT/XFT configuration. Loose selection cuts as follows, The data are collected with the J/ψ -triggers, and the most important trigger selections are briefly described below.

At Level 1, the di-muon trigger requires two muon stubs. A muon stub is a short trajectory formed by hits in the muon chamber (CMU, CMX and CMP). The stubs are matched in the XTRP to a track from the XFT.

The tracks are required to be of opposite charge in the L1_TWO_CMU1.5_PT1.5 and L1_CMU1.5_PT1.5_CMX1.5_PT2_CSX paths. For the run range between 138425 to 181838, the Level 1 di-muon triggers were auto-accepted at Level 2.

Starting from run 181839, the dimuon trigger paths have L2 cutting (opening angle and opposite-charge cut) implemented. At Level 3, two muon tracks are required to have opposite charge and are within 5 *cm* in z_0 . A cut of 30 *cm* between the stub and track intercept is applied for CMU muons, while this matching cut is 50 *cm* for CMX muons and 15 *cm* for CMUP muons. There is a P_T cut of 1.5, 2 and 4 GeV/c for tracks associated with CMU muon, CMX muon and CMUP muon respectively.

TrackRefitter is used for track refitting and rescaling COT covariance matrix, in accordance with the procedures described in CDF 6905 [49] [50]. Calibration table is PROD_PHYSICS_CDF and PassName is set to 13 for each run. This is for several reasons, track parameters are corrected for the energy loss in the material of the detector using appropriate particle type hypothesis. Indeed, as a particle travels through the material of the detector it losses energy, therefore a measurement by a measuring station further downstream may need to be corrected. In tracking, the uncertainties on the COT hit positions are ascribed without taking into account the effect of multiplying scattering in the material of the detector, therefore the uncertainties on track parameters retured by the track fit tend to underestimated(in a fashion that depends where the track goes in the detector and how energetic the track is). **TrackRefitter** brings these uncertainties back in line usiong empirical corrections. We dropped L00 hits in thr track refit, because the respective trakcing sub-systems are not yet sufficiently well understood and calibrated. Also the results of the kind of analyses we describe are not expected to benefit substantially from using L00. Track refit starts with COT track parameters and error matrix. A succesful refit therefore relies on a well measured track. In this anaylsis, no track minimum hit requirement is applied because a track is well understood by tracking group. The elements of the initial track covariance matrix are rescaled using the accepted default method using **TrackRefitter**. This procedure is necessary to correct for multiple scattering effects in the drift chamber volume. CTVMFT is used for vertexing, mass constraint is applied on J/ψ candidates. Rescaled magnetic field is 1.41 Tesla on vertex fit. The primary vertex is chosen as the closest point to the z position of the J/ψ vertex.

We use CDF offline version 5.3.4 for B meson reconstruction.

3.2 Basic Selections

The cuts used in this analysis are similar to the analysis which measures B hadron mass into J/ψ final state [51]. The basic requirements for tracks and muons are as follows:

- Track quality cuts:
 - ≥ 3 Silicon r - ϕ hits (including ISL)
- Muon selection:
 - $P_T(\mu) > 1.5 \text{ GeV}/c$
 - CMU stub matching $\chi_{xpos}^2 < 9$

We also have studied the optimization cut of χ_{xpos}^2 . The results show that there is no significant improvements, we therefore decided to keep the cut the same as analysis in the CDF experiment.

3.3 Selection for $J/\psi, \psi(2S) \rightarrow \mu^+ \mu^-$

In $p\bar{p}$ collision at $\sqrt{s} = 1.96 \text{ TeV}$ with the trigger requirements we have, at least 80% of J/ψ are from prompt $c\bar{c}$ production, while not more than 20% are coming from B decays [57]. With good track quality and muon selection requirements described above, $J/\psi, \psi(2S)$ candidates are subjected to a vertex constraint fit using CTVMFT package VertexFit. The resultant invariant mass is required to be within 80 MeV/c^2 of PDG [13] value (3096.87 MeV/c^2 for J/ψ and 3686.093 MeV/c^2 for $\psi(2S)$). Figure 3.1 and Figure 3.2 show the invariance mass distributions of $J/\psi \rightarrow \mu^+ \mu^-$ and $\psi(2S) \rightarrow \mu^+ \mu^-$, respectively.

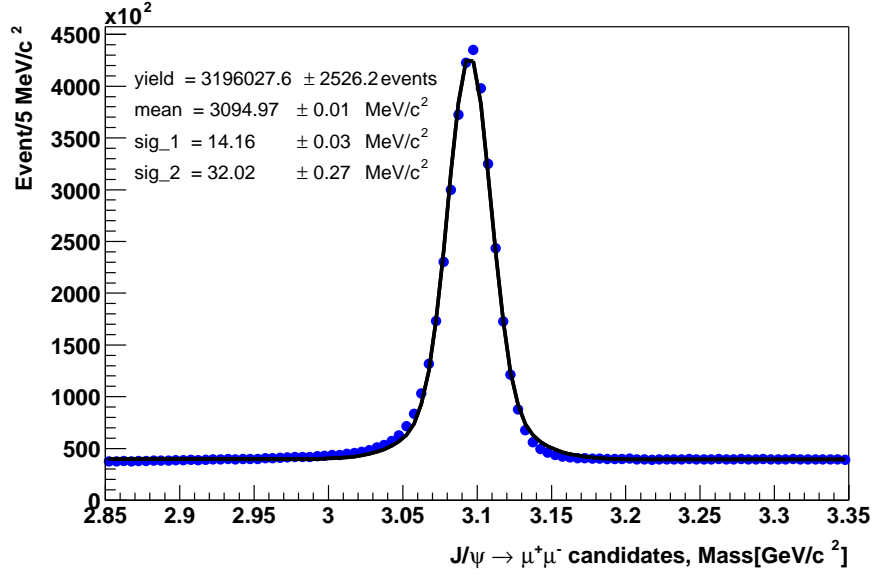


Figure 3.1: The invariance mass distributions of $J/\psi \rightarrow \mu^+\mu^-$.

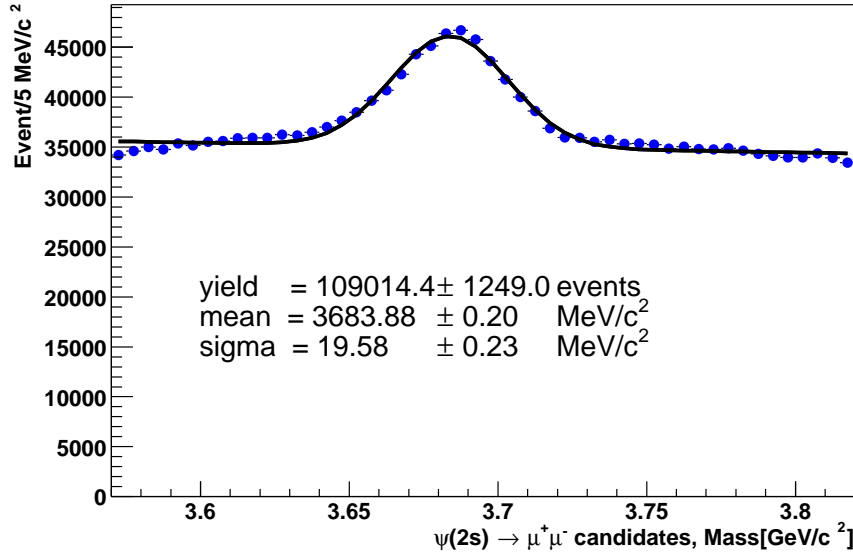


Figure 3.2: The invariance mass distributions of $\psi(2S) \rightarrow \mu^+\mu^-$.

3.4 Selection for $\psi(2S) \rightarrow J/\psi \pi^+ \pi^-$

With good track quality and muon selection described above, the vertex fit is applied to 2 muons with the J/ψ mass constrained to the PDG value. In addition, we require that the invariant mass of $\pi^+ \pi^-$ be between $0.31 \text{ GeV}/c^2$ and $0.61 \text{ GeV}/c^2$ [54]. Figure 3.3 shows the invariant mass of $\psi(2S) \rightarrow J/\psi \pi^+ \pi^-$.

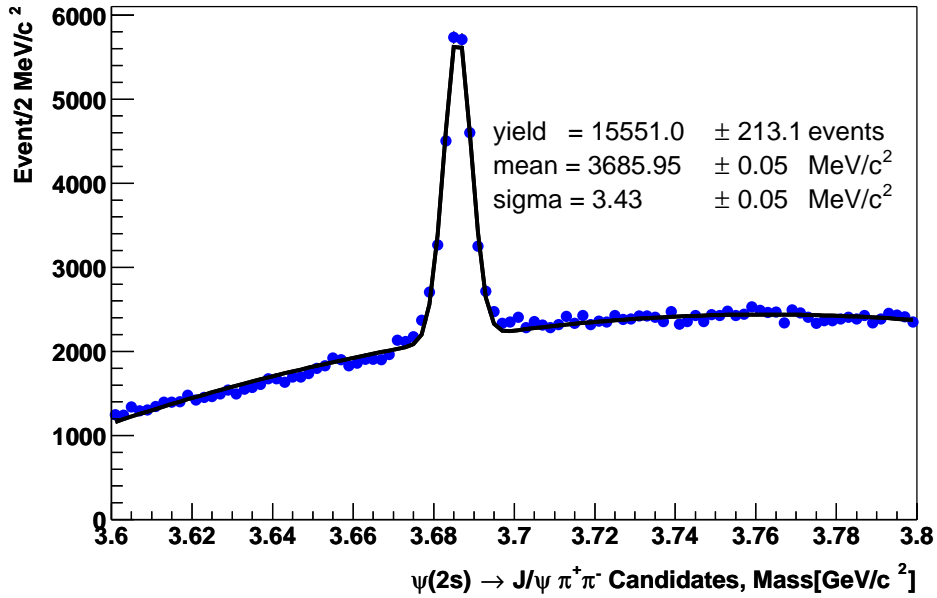


Figure 3.3: The invariance mass distributions of $\psi(2S) \rightarrow J/\psi \pi^+ \pi^-$.

3.5 Reconstruction of $B_u^\pm \rightarrow J/\psi K^\pm, B_u^\pm \rightarrow \psi(2S)K^\pm$ and $B_s^0 \rightarrow J/\psi\phi$

The reconstruction begins by selecting $J/\psi \rightarrow \mu^+\mu^-$ or $\psi(2S) \rightarrow \mu^+\mu^-$ or $\psi(2S) \rightarrow J/\psi\pi^+\pi^-$ candidates as described above. Once a J/ψ or $\psi(2S)$ candidate is selected, we then search for a $\phi \rightarrow K^+K^-$ candidate with a pair of additional tracks each also with $p_T > 0.4$ GeV/ c . The invariant mass of K^+K^- is required to be within 10 MeV/ c^2 of the ϕ mass [?]. The p_T of ϕ candidate is required to be greater than 2.0 GeV/ c . The B meson candidates are then reconstructed by associating a J/ψ or $\psi(2S)$ candidate with a ϕ candidate. Combinatoric background is greatly suppressed due to the narrowness of ϕ resonance. All tracks, 4 tracks in $B_s^0 \rightarrow J/\psi\phi$ or $B_s^0 \rightarrow \psi(2S)\phi$ followed by $\psi(2S) \rightarrow \mu^+\mu^-$ and 6 tracks in $B_s^0 \rightarrow \psi(2S)\phi$ followed by $\psi(2S) \rightarrow J/\psi\pi^+\pi^-$, are required to be consistent with having originated from a common vertex. Prompt background, with tracks coming directly from the primary vertex, can be reduced by exploiting variables sensitive to the long lifetime of the B meson. To reduce prompt background, the transverse decay length (L_{xy}) of B is required to exceed 100 μm , where L_{xy} is defined as the transverse distance from the beam axis to the B decay vertex projected onto the transverse momentum of B_s^0 candidate. To ensure well measured B meson decay vertex. The transverse momentum of B_s^0 candidate is required to be greater than 6.5 GeV/ c to further reduce combinatoric background. The analysis cuts are list in Table 3.1 and Table 3.2 for B_u^\pm and B_s^0 respectively.

Figure 3.4 and Figure 3.5 show the invariant mass distributions for $B_u^\pm \rightarrow J/\psi K^\pm$ and $B_u^\pm \rightarrow \psi(2S)K^\pm$, while Figure 3.6 shows the invariant mass distribution for $B_s^0 \rightarrow J/\psi\phi$. The mass distribution is fitted with a single Gaussian for signal and 1st order polynomial for background, the fitting range is done from 5.1 to 5.6 GeV/ c^2 . Fitting results with different ranges as well as different functions will be described later in the systematics section.

3.5 Reconstruction of $B_u^\pm \rightarrow J/\psi K^\pm, B_u^\pm \rightarrow \psi(2S)K^\pm$ and $B_s^0 \rightarrow J/\psi \phi$

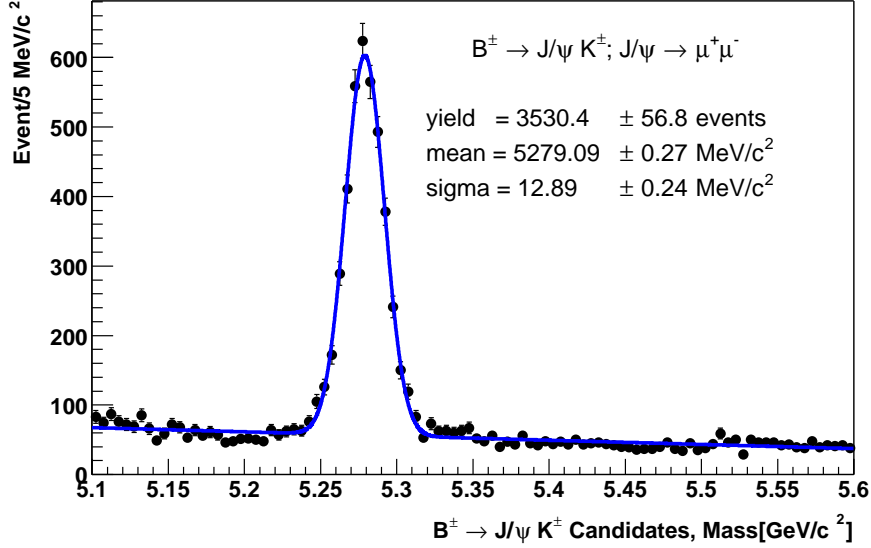


Figure 3.4: $B_u^\pm \rightarrow J/\psi K^\pm$ mass distribution where $J/\psi \rightarrow \mu^+\mu^-$. The mass distribution is fitted with a single Gaussian for signal and 1st order polynomial for background.

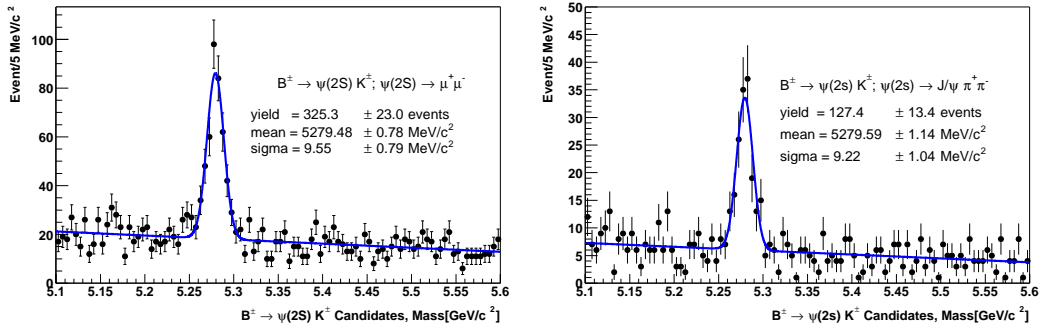


Figure 3.5: $B_u^\pm \rightarrow (\psi(2S) \rightarrow \mu^+\mu^-)K^\pm$ mass distribution(left), $B_u^\pm \rightarrow (\psi(2S) \rightarrow J/\psi \pi^+\pi^-)K^\pm$ mass distribution(right). The mass distribution is fitted with a single Gaussian for signal and 1st order polynomial for background.

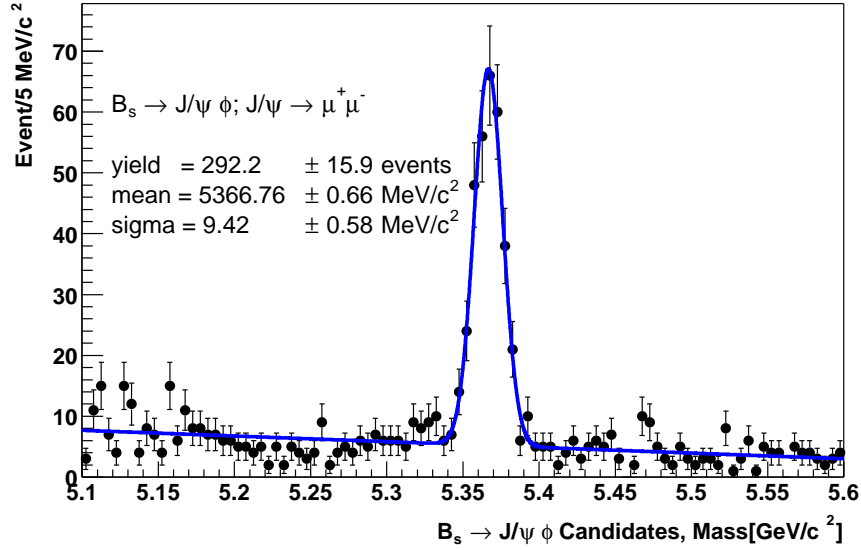


Figure 3.6: $B_s^0 \rightarrow J/\psi \phi$ mass distribution where $J/\psi \rightarrow \mu^+ \mu^-$ and $\phi \rightarrow K^+ K^-$. The fitting function is single Gaussian for signal and 1st order polynomial for background.

3.5 Reconstruction of $B_u^\pm \rightarrow J/\psi K^\pm, B_u^\pm \rightarrow \psi(2S)K^\pm$ and $B_s^0 \rightarrow J/\psi \phi$ 53

$B_u^\pm \rightarrow J/\psi K^\pm$	$B_u^\pm \rightarrow \psi(2S)K^\pm$ $\psi(2S) \rightarrow \mu^+\mu^-$	$B_u^\pm \rightarrow \psi(2S)K^\pm$ $\psi(2S) \rightarrow J/\psi \pi^+\pi^-$	Units
Silicon r - ϕ hits ≥ 3	same as left	same as left	
$P_T(\mu) > 1.5$	same as left	same as left	GeV/c
$ M_{(\mu^+\mu^-)} - M_{J/\psi}^{PDG} \leq 80$	same as left	same as left	MeV/ c^2
-	-	$ M_{(\mu^+\mu^-\pi^+\pi^-)} - M_{\psi(2S)}^{PDG} \leq 20$	MeV/ c^2
-	-	$0.31 \leq M_{(\pi^+\pi^-)} \leq 0.61$	GeV/ c^2
$P_T(K^\pm) > 2.0$	same as left	same as left	GeV/c
$P_T(B_s^0) > 6.5$	same as left	same as left	GeV/c
CTVMFT fit converges	same as left	same as left	
prob(B vertex fit) > 0.1	same as left	same as left	%
$L_{xy}(B) > 100$	same as left	same as left	μm

Table 3.1: All applied cuts for reconstruction of B_u^\pm ; J/ψ and $\psi(2S)$ decays to $\mu^+\mu^-$, and $\psi(2S) \rightarrow J/\psi \pi^+\pi^-$.

$B_s^0 \rightarrow J/\psi \phi$	$B_s^0 \rightarrow \psi(2S)\phi$ $\psi(2S) \rightarrow \mu^+\mu^-$	$B_s^0 \rightarrow \psi(2S)\phi$ $\psi(2S) \rightarrow J/\psi \pi^+\pi^-$	Units
Silicon r - ϕ hits ≥ 3	same as left	same as left	
$P_T(\mu) > 1.5$	same as left	same as left	GeV/c
$ M_{(\mu^+\mu^-)} - M_{J/\psi}^{PDG} \leq 80$	same as left	same as left	MeV/ c^2
-	-	$ M_{(\mu^+\mu^-\pi^+\pi^-)} - M_{\psi(2S)}^{PDG} \leq 20$	MeV/ c^2
-	-	$0.31 \leq M_{(\pi^+\pi^-)} \leq 0.61$	GeV/ c^2
$P_T(\phi) > 2.0$	same as left	same as left	GeV/c
$ M_{(K^+K^-)} - M_\phi^{PDG} \leq 10$	same as left	same as left	MeV/ c^2
$P_T(B_s) > 6.5$	same as left	same as left	GeV/c
CTVMFT fit converges	same as left	same as left	
prob(B vertex fit) > 0.1	same as left	same as left	%
$L_{xy}(B) > 100$	same as left	same as left	μm

Table 3.2: The summary of cuts applied for reconstruction of $B_s^0 \rightarrow J/\psi \phi$, $B_s^0 \rightarrow \psi(2S)\phi$ with $\psi(2S) \rightarrow \mu^+\mu^-$ and $B_s^0 \rightarrow \psi(2S)\phi$ with $\psi(2S) \rightarrow J/\psi \pi^+\pi^-$.

For $B_u^\pm \rightarrow J/\psi K^\pm$ and $B_u^\pm \rightarrow \psi(2S)K^\pm$ decays, there are Cabbibo suppressed decay contribution. To evaluate this effect, we generated Monte Carlo samples for $B^\pm \rightarrow J/\psi \pi^\pm$ and $B^\pm \rightarrow \psi(2S)\pi^\pm$ and then reconstruct them as $B_u^\pm \rightarrow J/\psi K^\pm$ and $B_u^\pm \rightarrow \psi(2S)K^\pm$. Figure 3.7 shows the shape of the mass distribution in each case. We then fit the $B_u^\pm \rightarrow J/\psi K^\pm$ and $B_u^\pm \rightarrow \psi(2S)K^\pm$ mass distribution with the Cabbibo suppressed decay contribution taken into account. Figure 3.8 shows the result, and the fitting range is between 5.2 - 5.6 GeV/c^2 . The Cabbibo suppressed contribution is about 3.6 %.

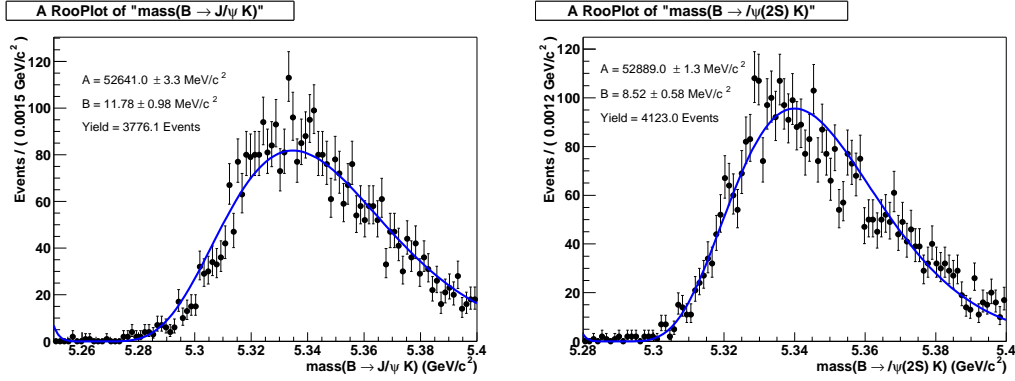


Figure 3.7: Cabbibo suppressed $B^\pm \rightarrow J/\psi \pi^\pm$ mass distribution(left), $B^\pm \rightarrow \psi(2S)\pi^\pm$ mass distribution(right). The fitting function is defined as Equation 3.1

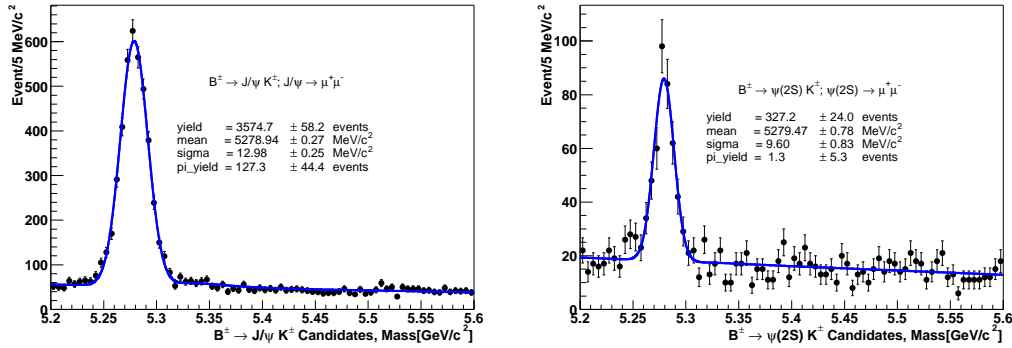


Figure 3.8: Fitting of the $B_u^\pm \rightarrow J/\psi K^\pm$ and $B_u^\pm \rightarrow \psi(2S)K^\pm$ mass distribution with the Cabbibo suppressed decay contribution taken into account.

3.5 Reconstruction of $B_u^\pm \rightarrow J/\psi K^\pm, B_u^\pm \rightarrow \psi(2S) K^\pm$ and $B_s^0 \rightarrow J/\psi \phi$ 55

Likelihood Function of corrected fitting of B^\pm

$$\mathcal{L}_i = f_{sig} G(x, m, \sigma) + (1 - f_{sig})(f_\pi C(x, A, B) + (1 - f_\pi) B(x, s)) \quad (3.1)$$

where f_{sig} is signal fraction, $G(x, m, \sigma)$ is Gaussian function,

$$G(x, m, \sigma) = \frac{1}{\sqrt{2\pi}\sigma} \exp^{-\frac{(x-m)^2}{2\sigma^2}}$$

$C(x, A, B)$ is Cabbibo suppressed B^\pm ,

$$C(x, A, B) = \frac{1}{Norm} \cdot (x - A)^6 \cdot \exp^{-\frac{x-A}{B}}$$

$B(x, s)$ is the 1st order polynomial function,

$$B(x, s) \text{ is } s \cdot \left(x - \frac{x_{max} + x_{min}}{2}\right) + \frac{1}{x_{max} - x_{min}}$$

At here, A, B is fixed with MC

Chapter 4

Observation of $B_s^0 \rightarrow \psi(2S)\phi$

Figure 4.1 shows the invariant mass distributions of $B_s^0 \rightarrow \psi(2S)\phi$, with $\psi(2S) \rightarrow \mu^+\mu^-$ and $\psi(2S) \rightarrow J/\psi\pi^+\pi^-$. Fitting is done the same way as in other modes. The width for each mode is fixed in the following way. We take the ratio of the widths from Monte Carlo simulation for $B_s^0 \rightarrow \psi(2S)\phi$ relative to $B_s^0 \rightarrow J/\psi\phi$, then calculate the width for $B_s^0 \rightarrow \psi(2S)\phi$ using the width of $B_s^0 \rightarrow J/\psi\phi$ from data. Comparison between Monte Carlo and data for the control sample of $B_u^\pm \rightarrow J/\psi K^\pm$ and $B_u^\pm \rightarrow \psi(2S)K^\pm$ show that Monte Carlo simulation predict the relative ratio of width of the two modes reasonably well. The details are list in Table 4.1 and Table 4.2, which summarize the mean value and width for both Monte Carlo and data for all decay modes. More details of Monte Carlo simulation will be described later.

4.1 Fitting method

The likelihood function used for fitting all B meson mass distribution defined as follows:

$$\mathcal{L}(\vec{\theta}) = \prod_{i=1}^n f(x_i, \vec{\theta})$$

where the x_i is data following probability density function $f(x, \vec{\theta})$ and $\vec{\theta}$ is unknown parameters to be determined. The likelihood for ith entry is like as

$$\mathcal{L}_i = f_{sig}S(x_i; m, \sigma) + (1 - f_{sig})B(x_i; slop)$$

where f_{sig} is signal fraction, S is Gaussian function for signal defined as

$$S(x; m, \sigma) = \frac{1}{\sqrt{2\pi}\sigma} \exp\left(-\frac{x-m}{2\sigma^2}\right),$$

B is the 1st order polynomial function for background defined as

$$B(x; slop) = slop \cdot \left(x - \frac{x_{max}+x_{min}}{2}\right) + \frac{1}{x_{max}-x_{min}},$$

where x_{max}, x_{min} is maximum and minimum mass fitting range.

We obtain 20.2 ± 5.0 events for $\psi(2S) \rightarrow \mu^+\mu^-$ channel and 12.3 ± 4.1 events for the $\psi(2S) \rightarrow J/\psi\pi^+\pi^-$ channel. Figure 4.2 shows the combined mass distributions of $B_s^0 \rightarrow \psi(2S)\phi$ with $\psi(2S) \rightarrow \mu^+\mu^-$ and $\psi(2S) \rightarrow J/\psi\pi^+\pi^-$. We fit the combined distribution using two Gaussians and obtain 31.8 ± 6.3 events.

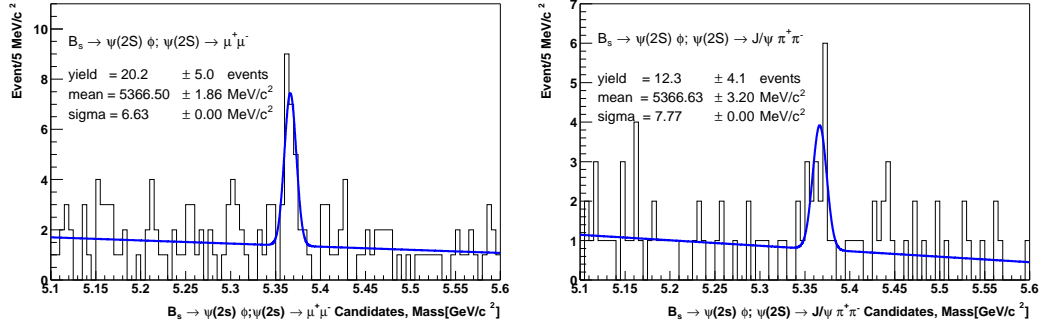


Figure 4.1: $B_s^0 \rightarrow (\psi(2S) \rightarrow \mu^+\mu^-)\phi$ mass distribution(left), $B_s^0 \rightarrow (\psi(2S) \rightarrow J/\psi\pi^+\pi^-)\phi$ mass distribution width fixed(right). The fitting function is single Gaussian for signal and the 1st order polynomial for background.

4.2 Background contributions

Two sources of background are expected in the B_s^0 signal region: combinatoric background and reflection of $B_d^0 \rightarrow J/\psi K^{*0}$ (for $B_s^0 \rightarrow J/\psi\phi$) or

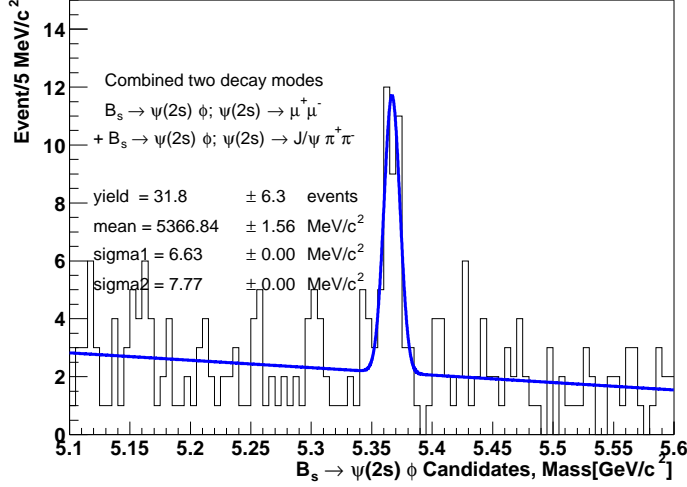


Figure 4.2: The combined mass distribution of $B_s^0 \rightarrow (\psi(2S) \rightarrow \mu^+\mu^-)\phi$ mode and $B_s^0 \rightarrow (\psi(2S) \rightarrow J/\psi\pi^+\pi^-)\phi$ mode. The fitting function is double Gaussian for signal and 1st order polynomial for background.

$B_d^0 \rightarrow \psi(2S)K^{*0}$ (for $B_s^0 \rightarrow \psi(2S)\phi$) where the pion from K^{*0} decay is mis-assigned as a kaon. The combinatoric background is modeled by a first order polynomial. The $B_d^0 \rightarrow J/\psi K^{*0}$ ($B_d^0 \rightarrow \psi(2S)K^{*0}$) reflection background results in a broad distribution near and above the B_s^0 signal region. The fraction of $B_d^0 \rightarrow J/\psi K^{*0}$ ($B_d^0 \rightarrow \psi(2S)K^{*0}$) events fall into the $B_s^0 \rightarrow J/\psi\phi$ ($B_s^0 \rightarrow \psi(2S)\phi$) signal region is estimated using Monte Carlo simulation. The background contribution from reflection in our data sample is then calculated by multiplying the fraction determined from Monte Carlo simulation by the number of $B_d^0 \rightarrow J/\psi K^{*0}$ and $B_d^0 \rightarrow \psi(2S)K^{*0}$ candidates in the same data. The contribution of $B_d^0 \rightarrow J/\psi K^{*0}$ reflection in the $B_s^0 \rightarrow J/\psi\phi$ signal region is estimated to be 6.6 ± 0.3 events. The contribution of $B_d^0 \rightarrow \psi(2S)K^{*0}$ reflection in the $B_s^0 \rightarrow \psi(2S)\phi$ signal region is 0.34 ± 0.05 and 0.19 ± 0.03 events for $\psi(2S) \rightarrow \mu^+\mu^-$ and $\psi(2S) \rightarrow J/\psi\pi^+\pi^-$ modes, respectively.

The details of the background contribution study will be described in Section 3.9. The conclusion is that the $B_d^0 \rightarrow J/\psi K^{*0}$ ($B_d^0 \rightarrow \psi(2S)K^{*0}$) back-

Decay	Mean[MeV/ c^2]	Width[MeV/ c^2]
$B_u^\pm \rightarrow J/\psi K^\pm$	5279.29 ± 0.07	11.94 ± 0.06
$B_s^0 \rightarrow J/\psi \phi$	5371.00 ± 0.04	8.72 ± 0.04
$B_u^\pm \rightarrow \psi(2S)K^\pm; \psi(2S) \rightarrow \mu^+\mu^-$	5278.85 ± 0.05	9.14 ± 0.04
$B_u^\pm \rightarrow \psi(2S)K^\pm; \psi(2S) \rightarrow J/\psi \pi^+\pi^-$	5278.85 ± 0.20	9.72 ± 0.15
$B_s^0 \rightarrow \psi(2S)\phi; \psi(2S) \rightarrow \mu^+\mu^-$	5370.55 ± 0.03	6.14 ± 0.02
$B_s^0 \rightarrow \psi(2S)\phi; \psi(2S) \rightarrow J/\psi \pi^+\pi^-$	5370.73 ± 0.13	7.19 ± 0.09

Table 4.1: Summary of fitting results of charmonium final states of Monte Carlo.

Decay	Mean	Width	Yield
$B_u^\pm \rightarrow J/\psi K^\pm$	5279.09 ± 0.27	12.89 ± 0.24	3530.5 ± 56.8
$B_s^0 \rightarrow J/\psi \phi$	5366.76 ± 0.66	9.42 ± 0.58	292.2 ± 15.9
$B_u^\pm \rightarrow \psi(2S)K^\pm; \psi(2S) \rightarrow \mu^+\mu^-$	5279.48 ± 0.78	9.55 ± 0.79	325.4 ± 23.0
$B_u^\pm \rightarrow \psi(2S)K^\pm; \psi(2S) \rightarrow J/\psi \pi^+\pi^-$	5279.59 ± 1.14	9.22 ± 1.04	127.4 ± 13.4
$B_s^0 \rightarrow \psi(2S)\phi; \psi(2S) \rightarrow \mu^+\mu^-$	5366.50 ± 1.86	6.63 ± 0.00	20.2 ± 5.0
$B_s^0 \rightarrow \psi(2S)\phi; \psi(2S) \rightarrow J/\psi \pi^+\pi^-$	5366.63 ± 3.20	7.77 ± 0.00	12.3 ± 4.1

Table 4.2: Summary of fitting results of charmonium final states using real data, The unit of mean and width is MeV/ c^2 .

ground contribution is negligible due to the fact that only a small fraction of the misidentified $K^{*0} \rightarrow K^+\pi^-$ can satisfy the $\phi \rightarrow K^+K^-$ mass requirement.

4.3 Significance of Signal

Since $B_s^0 \rightarrow \psi(2S)\phi$ decay is the first observation, we will need to calculate the signal significance. In order to estimate the significance of the signals, we follow the approach recommended by the statistic committee and also used for example in $B_s \rightarrow \phi\phi$ analysis [48]. We evaluate the probability for the expected background to fluctuate to the observed number of events, under the hypothesis of null signal, using a Poisson distribution with the expected background events as mean value: the so-called P-values. The P-value, P are

defined as:

$$P = \sum_{x=N}^{\infty} \frac{B^x}{x!} \cdot e^{-B} = 1 - \sum_{x=0}^{N-1} \frac{B^x}{x!} \cdot e^{-B}, \quad (4.1)$$

where B is background from the fitting, $[\pm 3\sigma]$ excluded events in the signal region. We also define P-value as

$$P = \int_S^{\infty} \frac{1}{\sqrt{2\pi}} e^{-\frac{x^2}{2}} dx = \frac{1}{2} \cdot \text{erfc}\left(\frac{S}{\sqrt{2}}\right) (\text{one sided Gaussian tail}), \quad (4.2)$$

where N is number of events in the signal region, defined as $[\pm 3\sigma]$, S is statistical significance. We calculate the P -value from Equation 4.1 and 4.2. the total P-value of two independent P-value can be expressed [56] as:

$$P_{total} = P_1 \cdot P_2 \times (1 - \ln(P_1 \cdot P_2)), \quad (4.3)$$

where P_{total} is total P-value and P_1, P_2 are two independent P-value. Table 4.3 shows the P-value and significance.

Decay of $B_s^0 \rightarrow \psi(2S)\phi$	Signal	Background	P-value	Significance
$\psi(2S) \rightarrow \mu^+\mu^-$	30	10.0 ± 3.2	2.51×10^{-7}	5.02σ
$\psi(2S) \rightarrow J/\psi \pi^+\pi^-$	20	6.5 ± 2.6	1.61×10^{-5}	4.16σ
Combined $B_s^0 \rightarrow \psi(2S)\phi$			1.11×10^{-10}	6.35σ

Table 4.3: P-value and significance of each decay mode and combined.

4.4 Details on Background Contribution study

As mentioned earlier, two sources of background are expected in the B_s^0 signal region: combinatoric background and reflection of $B_d^0 \rightarrow J/\psi K^{*0}$ (for $B_s^0 \rightarrow J/\psi\phi$) or $B_d^0 \rightarrow \psi(2S)K^{*0}$ (for $B_s^0 \rightarrow \psi(2S)\phi$) where the pion from K^{*0} decay is mis-assigned as a kaon. The combinatoric background is modeled by a first order polynomial. The $B_d^0 \rightarrow J/\psi K^{*0}$ ($B_d^0 \rightarrow \psi(2S)K^{*0}$) reflection background

results in a broad distribution near and above the B_s^0 signal region. In Section 3.6, we have made the statement that the $B_d^0 \rightarrow J/\psi K^{*0}$ ($B_d^0 \rightarrow \psi(2S)K^{*0}$) reflection background contribution is negligible, therefore, we have ignored this background in the fitting. In this section, we will describe the details of our study on this type of background, to show how we have arrived to that conclusion.

This background contribution can be studied in three different ways. First of all, the fraction of $B_d^0 \rightarrow J/\psi K^{*0}$ ($B_d^0 \rightarrow \psi(2S)K^{*0}$) events fall into the $B_s^0 \rightarrow J/\psi\phi$ ($B_s^0 \rightarrow \psi(2S)\phi$) signal region can be estimated using Monte Carlo simulation. The background contribution from reflection in our data sample is then calculated by multiplying the fraction determined from Monte Carlo simulation by the number of $B_d^0 \rightarrow J/\psi K^{*0}$ and $B_d^0 \rightarrow \psi(2S)K^{*0}$ candidates observed in the same data. Secondly, one can take the background shape from Monte Carlo, and fit the B_s^0 mass spectra with this particular background taken into account and check if the result is consistent with what we obtained by neglecting the background contribution from reflection. Thirdly, one can fit the ϕ mass spectra directly in data, and check if the signal yield is consistent with what we obtained before by fitting the B_s^0 mass distribution. The last check is Monte Carlo independent.

Background Contribution estimate from Monte Carlo and data

We generate about 2M Monte Carlo events of $B_d^0 \rightarrow J/\psi K^{*0}$, 10M events of $B_d^0 \rightarrow (\psi(2S) \rightarrow \mu^+\mu^-)K^{*0}$ and 20M events of $B_d^0 \rightarrow (\psi(2S) \rightarrow \mu^+\mu^-)K^{*0}$ events. The $B_d^0 \rightarrow J/\psi K^{*0}$ ($B_d^0 \rightarrow \psi(2S)K^{*0}$) background contribution is expected to be small due to the fact that only a small fraction of the misidentified $K^{*0} \rightarrow K^+\pi^-$ can satisfy the $\phi \rightarrow K^+K^-$ mass requirement, as shown in Figure 4.3. To evaluate B_d^0 reflection in B_s^0 signal region, the B_d^0 is reconstructed as B_s^0 . The $B_d^0 \rightarrow J/\psi K^{*0}$ ($B_d^0 \rightarrow \psi(2S)K^{*0}$) reflection background results in a broad distribution near and above the B_s^0 signal region as shown in Figure 4.4 and Figure 4.5.

The B_d^0 signal yields from data, B_d^0 MC sample size as well as the B_d^0 MC

Decay	B_d^0 Data	B_d^0 MC	B_d^0 MC (B_s^0 region)
$B_d^0 \rightarrow J/\psi K^{*0}$	1440.6 ± 63.0	21109.0 ± 145.3	97.0 ± 9.8
$B_d^0 \rightarrow (\psi(2S) \rightarrow \mu^+ \mu^-) K^{*0}$	141.1 ± 20.4	57510.0 ± 239.8	138.0 ± 11.7
$B_d^0 \rightarrow (\psi(2S) \rightarrow J/\psi \pi^+ \pi^-) K^{*0}$	72.6 ± 12.7	69785.0 ± 264.2	99.0 ± 9.9

Table 4.4: Background Contribution from B_d^0 reflection to B_s^0 meson.

sample contributing in the B_s^0 signal region are summarized in Table 4.4. The background contribution from reflection in our data sample is then calculated by multiplying the fraction determined from Monte Carlo simulation by the number of $B_d^0 \rightarrow J/\psi K^{*0}$ and $B_d^0 \rightarrow \psi(2S) K^{*0}$ candidates in the same data.

$$N(B_d^0 \text{ reflection}) = N(B_d^0 \rightarrow J/\psi K^{*0}) \times \frac{n(B_s^0 \rightarrow J/\psi \phi)}{n(B_d^0 \rightarrow J/\psi K^{*0})},$$

where $N(B_d^0 \text{ reflection})$ is number of B_d^0 reflection events in the B_s^0 signal region, $N(B_d^0 \rightarrow J/\psi K^{*0})$ is number of events from data (Figure 4.6) and $n(B_s^0 \rightarrow J/\psi \phi)$ is number of $B_d^0 \rightarrow J/\psi K^{*0}$ Monte Carlo events reconstructed as $B_s^0 \rightarrow J/\psi \phi$ in $B_s^0 \rightarrow J/\psi \phi$ signal region, while $n(B_d^0 \rightarrow J/\psi K^{*0})$ is number of $B_d^0 \rightarrow J/\psi K^{*0}$ events from Monte Carlo simulation. The contribution of $B_d^0 \rightarrow J/\psi K^{*0}$ reflection in the $B_s^0 \rightarrow J/\psi \phi$ signal region is estimated to be 6.6 ± 0.3 events. The contribution of $B_d^0 \rightarrow \psi(2S) K^{*0}$ reflection in the $B_s^0 \rightarrow \psi(2S) \phi$ signal region is 0.34 ± 0.05 and 0.19 ± 0.03 events for $\psi(2S) \rightarrow \mu^+ \mu^-$ and $\psi(2S) \rightarrow J/\psi \pi^+ \pi^-$ modes, respectively. This corresponds about 2% of $B_s^0 \rightarrow J/\psi \phi$ and $B_s^0 \rightarrow \psi(2S) \phi$ signal events.

Including the B_d^0 background shape in the fit

As a consistency check, we also take the B_d^0 background (due to reflection) shape from Monte Carlo, and include the shape in the B_s^0 mass fitting for all three B_s^0 decay modes. Figure 4.7 shows the B^0 reflection effect (in red) in B_s mass distribution, the effect on the signal yield is negligible in all cases.

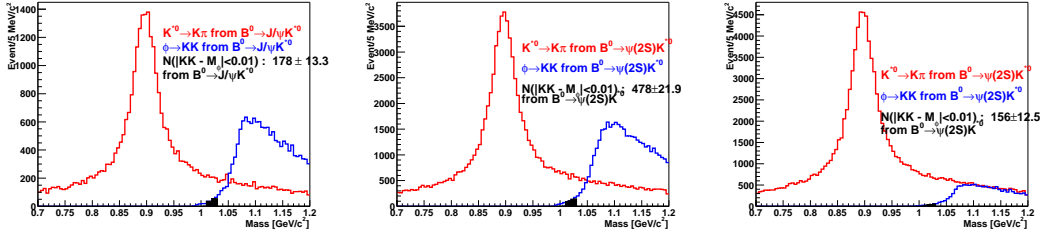


Figure 4.3: $K^{*0} \rightarrow K^+\pi^-$ distribution from $B_d^0 \rightarrow J/\psi K^{*0}$ ($B_d^0 \rightarrow \psi(2S) K^{*0}$) MC samples (red), and $\phi \rightarrow K^+K^-$ distribution when reconstructed as $B_s^0 \rightarrow J/\psi \phi$ ($B_s^0 \rightarrow \psi(2S)\phi$) (blue). The black area highlights the ϕ signal region, showing that only a small fraction of the misidentified $K^{*0} \rightarrow K^+\pi^-$ can satisfy the $\phi \rightarrow K^+K^-$ mass requirement.

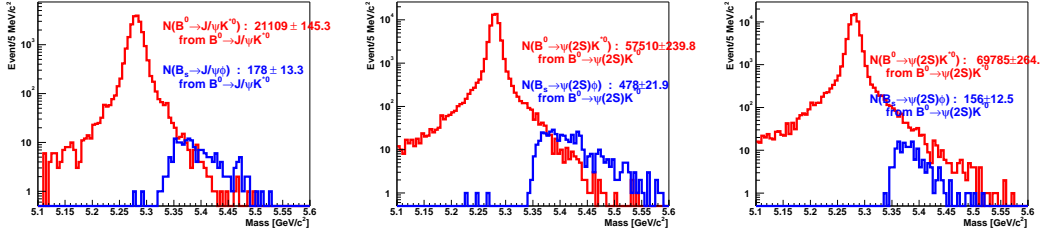


Figure 4.4: Red histograms are MC $B_d^0 \rightarrow J/\psi K^{*0}$ ($B_d^0 \rightarrow \psi(2S) K^{*0}$) mass distributions, and Blue histograms are for the same sample but reconstructed as $B_s^0 \rightarrow J/\psi \phi$ ($B_s^0 \rightarrow \psi(2S)\phi$).

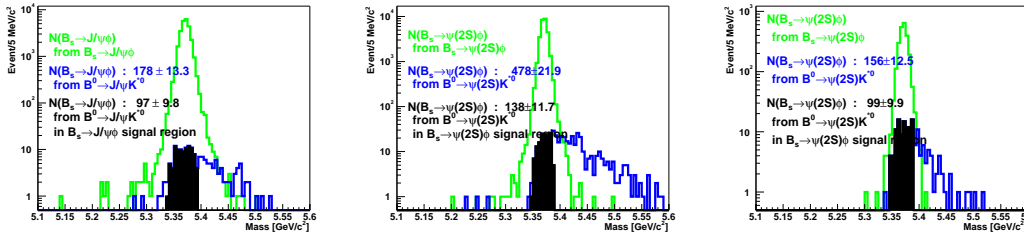


Figure 4.5: Green histograms are MC $B_s^0 \rightarrow J/\psi \phi$ ($B_s^0 \rightarrow \psi(2S)\phi$) signal distributions and blue histogram is MC $B_d^0 \rightarrow J/\psi K^{*0}$ ($B_d^0 \rightarrow \psi(2S) K^{*0}$) distribution reconstructed as $B_s^0 \rightarrow J/\psi \phi$ ($B_s^0 \rightarrow \psi(2S)\phi$), indicating that the background contribution from reflection results in a broad distribution near and above the B_s^0 signal region. Black area highlights the MC $B_d^0 \rightarrow J/\psi K^{*0}$ ($B_d^0 \rightarrow \psi(2S) K^{*0}$) reflection contribution in the signal region ($\pm 3\sigma$). Note that the right most plot is for $\psi(2S) \rightarrow J/\psi \pi^+\pi^-$ mode.

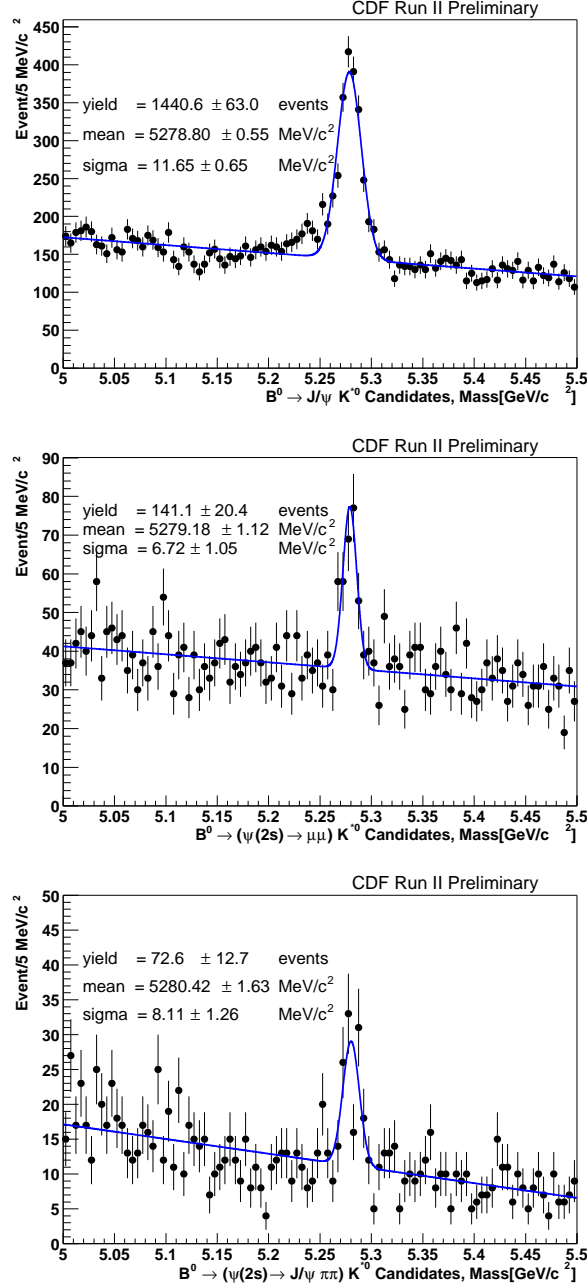


Figure 4.6: $B_d^0 \rightarrow J/\psi K^{*0}$ mass distribution(Upper), $B_d^0 \rightarrow (\psi(2S) \rightarrow \mu^+\mu^-) K^{*0}$ (middle) and $B_d^0 \rightarrow (\psi(2S) \rightarrow J/\psi \pi^+\pi^-) K^{*0}$ mass distribution(lower). The mass distribution is fitted with a single Gaussian for signal and 1st order polynomial for background. K- π swap is not considered.

Fitting the ϕ mass spectra in data for B_s^0

As another consistency check (Monte Carlo independent), we also fit the ϕ mass spectra in data for the B_s^0 modes. This check is important because if there is indeed a sizable contribution from the B_d^0 background reflection, then the background will show up in the ϕ mass distribution. On the other hand, if the background reflection is indeed negligible, then the signal yield from fitting the ϕ mass spectra should be consistent with that from fitting the B_s^0 mass spectra.

Figure 4.8 shows the $\phi \rightarrow K^+K^-$ mass distribution for $B_s^0 \rightarrow J/\psi\phi$ in the B_s^0 signal region, sideband region as well as after sideband subtraction. The B_s^0 signal region is defined as a $\pm 3\sigma$ mass window around the signal peak, while the sideband region is defined as -9σ to -6σ (low sideband) and $+6\sigma$ to $+9\sigma$ (high sideband). Figure 4.9 shows the fitting results for $\phi \rightarrow K^+K^-$ mass distribution from $B_s^0 \rightarrow J/\psi\phi$ in the B_s^0 signal region as well as after sideband subtraction. The result (after sideband subtraction) is consistent with that from fitting for the B_s^0 mass distribution. Figure 4.10 shows the $\phi \rightarrow K^+K^-$ mass distribution for $B_s^0 \rightarrow (\psi(2S) \rightarrow \mu^+\mu^-)\phi$ in the B_s^0 signal region, sideband region as well as after sideband subtraction. Figure 4.11 shows the fitting for $\phi \rightarrow K^+K^-$ mass distribution for $B_s^0 \rightarrow (\psi(2S) \rightarrow \mu^+\mu^-)\phi$ Monte Carlo and for data after sideband subtraction (in the later case, the width for the double Gaussian is fixed from Monte Carlo). The result is again consistent with that from fitting the B_s^0 mass spectra directly.

In conclusion, the $B_d^0 \rightarrow J/\psi K^{*0}$ ($B_d^0 \rightarrow \psi(2S)K^{*0}$) background contribution is negligible for this analysis, due to the fact that only a small fraction of the misidentified $K^{*0} \rightarrow K^+\pi^-$ can satisfy the $\phi \rightarrow K^+K^-$ mass requirement.

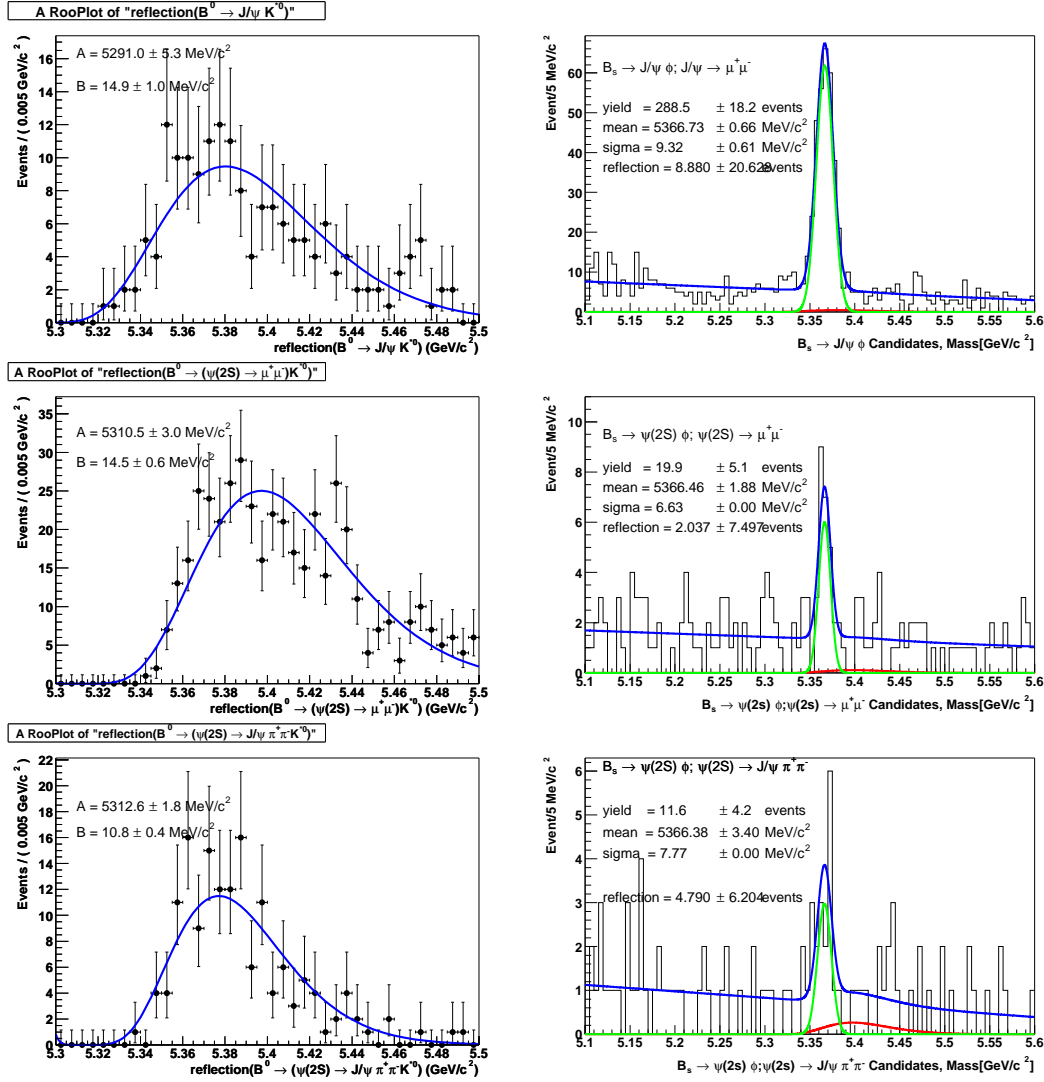


Figure 4.7: The B^0 reflection in B_s mass region(left column plots) and B_s mass distribution including B^0 reflection effect(right column plots), shown in red.

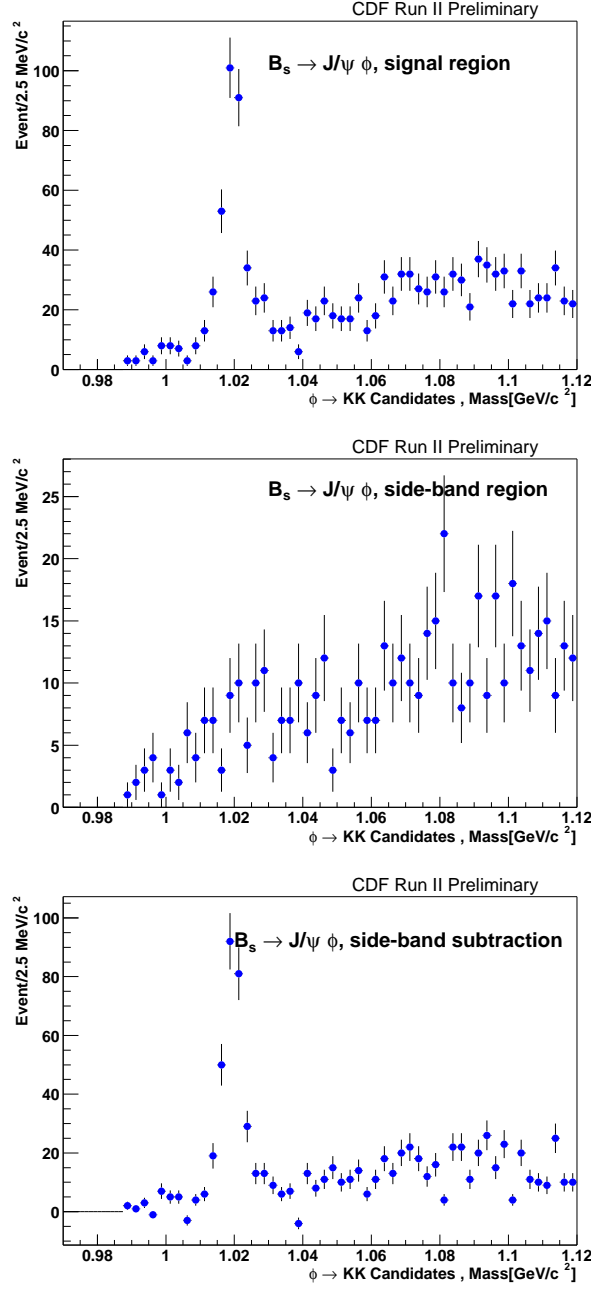


Figure 4.8: $\phi \rightarrow K^+K^-$ distribution from $B_s^0 \rightarrow J/\psi\phi$. Upper plot is in B_s^0 signal region, middle one is in the sideband region and lower one is after sideband subtraction.

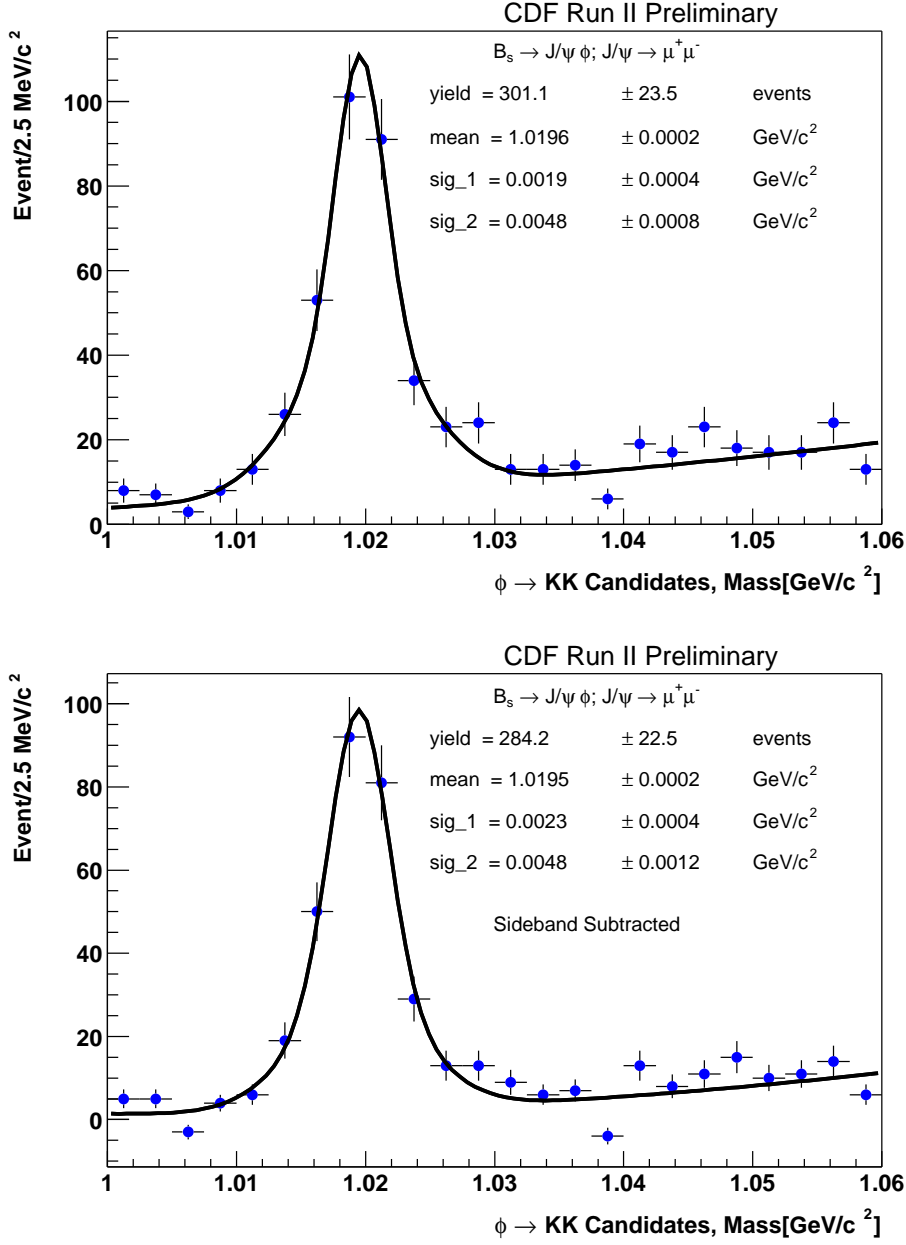


Figure 4.9: $\phi \rightarrow K^+ K^-$ distribution from $B_s^0 \rightarrow J/\psi \phi$. The mass distribution is fitted with a double Gaussian for signal and 2nd order polynomial for background. Upper plot is B_s^0 signal region, lower one is sideband subtracted region.

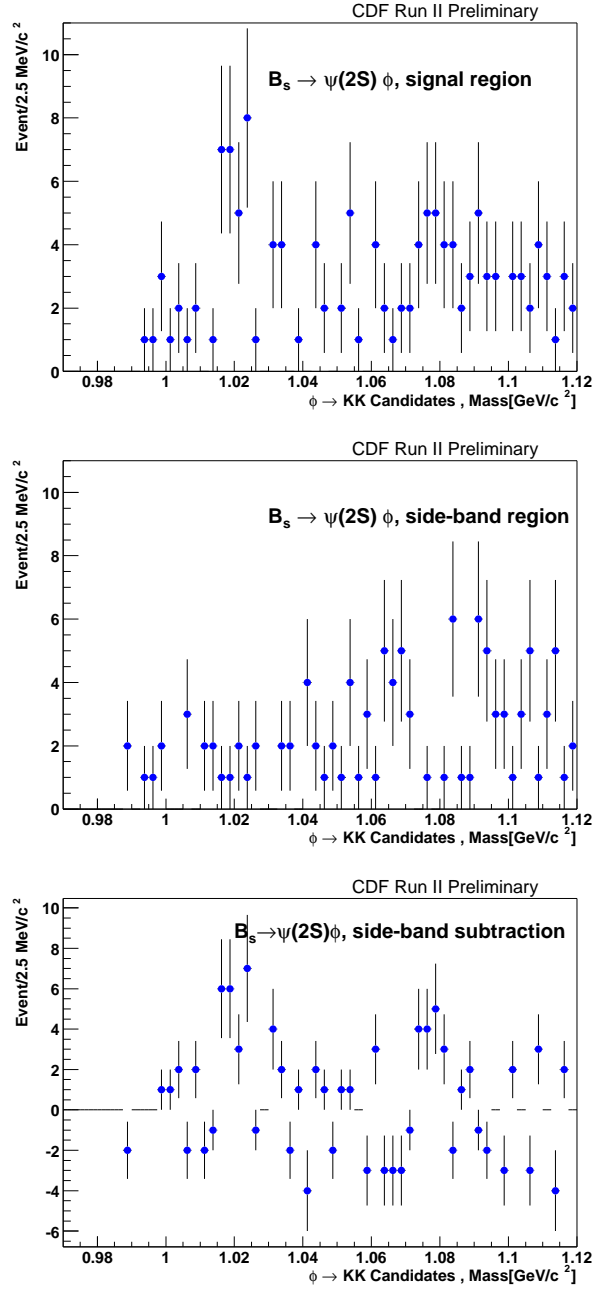


Figure 4.10: $\phi \rightarrow K^+K^-$ distribution from $B_s^0 \rightarrow (\psi(2S) \rightarrow \mu^+\mu^-)\phi$ decay. Upper plot is B_s^0 signal region, middle one is sideband region and lower one is sideband subtracted region.

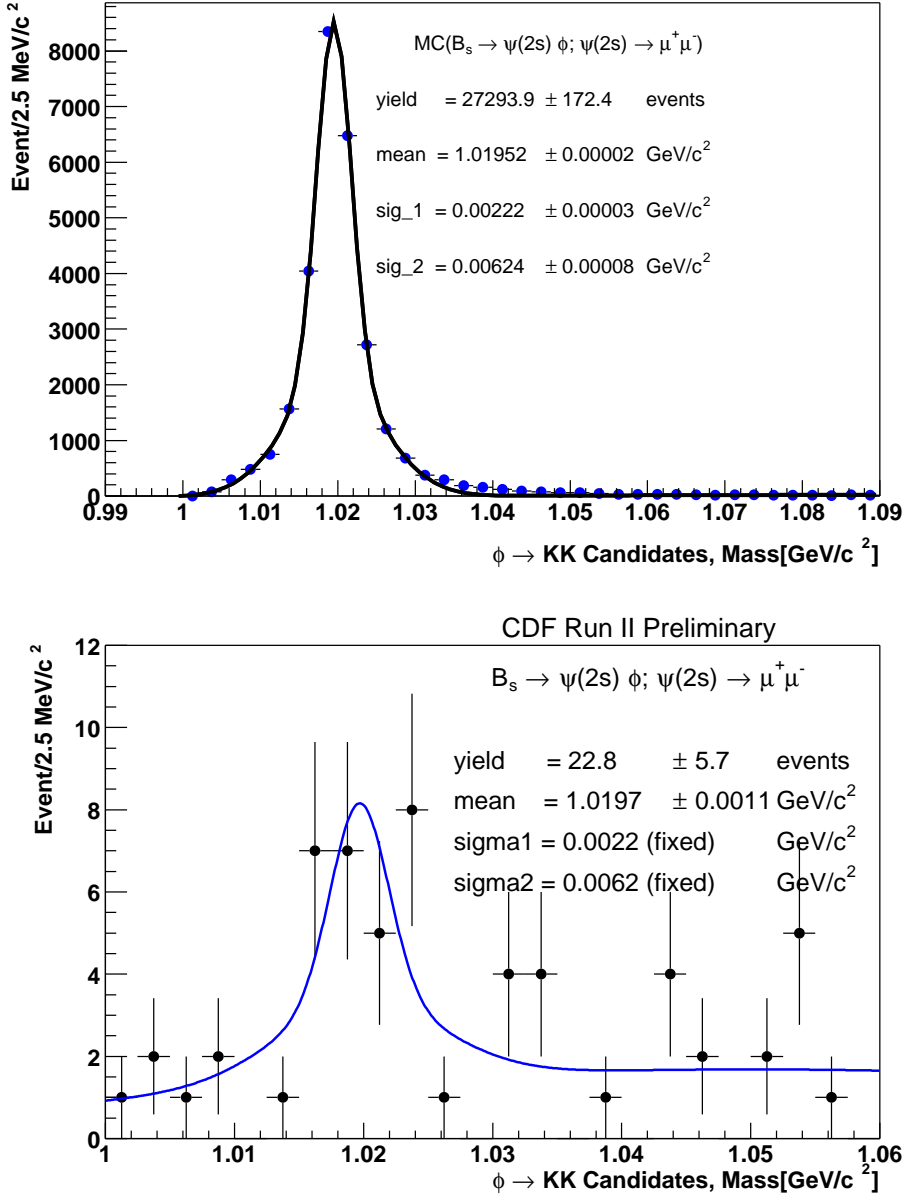


Figure 4.11: $\phi \rightarrow K^+K^-$ distribution from $B_s^0 \rightarrow (\psi(2S) \rightarrow \mu^+\mu^-)\phi$ decay. Upper plot is from Monte Carlo, lower plot from data after sideband subtraction. The mass distribution is fitted with a double Gaussian for signal and 2nd order polynomial for background. In the lower plot, the width of the double Gaussian is fixed to the value from Monte Carlo.

Chapter 5

The measurement of $\mathcal{B}(B_s^0 \rightarrow \psi(2S)\phi)/\mathcal{B}(B_s^0 \rightarrow J/\psi\phi)$

5.1 Introduction

As described earlier, we use $B_s^0 \rightarrow J/\psi\phi$ as normalization mode, and measure the relative branching ratio of $\mathcal{B}(B_s^0 \rightarrow \psi(2S)\phi)/\mathcal{B}(B_s^0 \rightarrow J/\psi\phi)$. Since in case of $\mu^+\mu^-$ modes most systematic effects are expected to cancel between normalization mode and signal mode, we will only use $\psi(2S) \rightarrow \mu^+\mu^-$ decay channel for the signal mode of $B_s^0 \rightarrow \psi(2S)\phi$. In order to do the measurement, we will need to determine the trigger and detection (including analysis selection cuts) efficiencies for the two decay modes. Here, we only care about the ratio of the detection efficiencies between the two modes, not the absolute values. We will use Monte Carlo events to determine the relative efficiency. To make sure the Monte Carlo simulation can predict the actual efficiencies reasonably well, we will use the control sample of B^\pm decays to do cross checks and study systematic effects.

5.2 Realistic Monte Carlo generation

The Monte Carlo samples for B decays is generated using B-generator [52]. Specific decays are performed with EvtGen [53]. We use single b -quark generation using NDE, b quark transverse momentum is required to be greater than 5 GeV/ c and its rapidity is within $-1.3 \leq \eta \leq 1.3$. HepgFilter(2 muons) is used as the generator level filter and require $-1.2 \leq \eta(\mu) \leq 1.2$, and $P_T(\mu)$ is greater than 1.4 GeV/ c for each J/ψ and $\psi(2S)$ decays as shown in Appendix B. We use standard trigger simulation and production with cdfsoft version 5.3.4 and generated Monte Carlo samples (about 2M events for each mode) for $B_u^\pm \rightarrow J/\psi K^\pm$, $B_u^\pm \rightarrow \psi(2S)K^\pm$ as well as $B_s^0 \rightarrow J/\psi\phi$, $B_s^0 \rightarrow \psi(2S)\phi$ decay modes.

5.3 Monte Carlo sample and data comparison

In order to make sure the Monte Carlo can reproduce the relative efficiencies reasonably well, we compare Monte Carlo events with data after sideband subtraction, using $B_u^\pm \rightarrow J/\psi K^\pm$, $B_u^\pm \rightarrow \psi(2S)K^\pm$ as well as $B_s^0 \rightarrow J/\psi\phi$.

Figure 5.1 shows the comparison between data and Monte Carlo for $B_u^\pm \rightarrow J/\psi K^\pm$ decay mode. Figure 5.2 is for $B_u^\pm \rightarrow \psi(2S)K^\pm$ with $\psi(2S) \rightarrow \mu^+\mu^-$. Figure 5.3 is for $B_s^0 \rightarrow J/\psi\phi$ mode.

The “Prob” numbers shown in the plots are for χ^2 test probability for the two distributions under comparison. Here is the description of the variable names used in the comparison plots:

- B Pt: B candidate P_T distribution;
- B Lxy: B candidate L_{xy} distribution without L_{xy} cut;
- Prob 2D: B candidate vertex fitting 2D probability (without the cut);
- J/ψ Pt: J/ψ candidate P_T ;
- J/ψ Pt: J/ψ candidate P_T ;

- J/ψ η : J/ψ candidate η ;
- $muon1$ pt: the P_T of the lower P_T muon candidate (with default cut);
- $muon2$ pt: the P_T of the higher P_T muon candidate (with default cut);
- $muon1$ eta: η of the lower P_T muon candidate;
- $muon2$ eta: η of the higher P_T muon candidate;
- $muon1$ phi: ϕ of the lower P_T muon candidate;
- $muon2$ phi: ϕ of the higher P_T muon candidate;
- kaon Pt: P_T of kaon candidate (without the cut);
- kaon eta: η of kaon candidate;
- kaon phi: ϕ of kaon candidate;
- delta jeta: difference between two muon candidate in η (absolute value);
- delta jphi: difference between two muon candidate in ϕ (absolute value);
- delta phieta: difference between two kaon candidate in η (absolute value);
- delta phiphi: difference between two kaon candidate in ϕ (absolute value);
- delta bphi: difference between J/ψ (or $\psi(2S)$) and ϕ in ϕ (absolute value);

The name convention also applies to other comparison plots shown later in the thesis.

5.4 Relative detection efficiencies for B^\pm and B_s

Table 5.1 shows the summary of relative efficiencies from Monte Carlo simulation, for both control samples as well as signal samples. Note that here we

have assumed that the polarization of $B_s^0 \rightarrow \psi(2S)\phi$ decay is the same as in $B_s^0 \rightarrow J/\psi\phi$. Systematics due to the lack of knowledge on the polarization for $B_s^0 \rightarrow \psi(2S)\phi$ is studied later in the systematics section.

Decay	Relative Efficiency	Comments
$B_u^\pm \rightarrow J/\psi K^\pm$	0.9719 ± 0.0075	Control Sample
$B_u^\pm \rightarrow \psi(2S)K^\pm; \psi(2S) \rightarrow \mu^+\mu^-$		
$B_s^0 \rightarrow J/\psi\phi$	0.9249 ± 0.0058	Signal Mode
$B_s^0 \rightarrow \psi(2S)\phi; \psi(2S) \rightarrow \mu^+\mu^-$		

Table 5.1: The relative efficiencies from Monte Carlo simulation.

5.5 The measurement of $\mathcal{B}(B_s^0 \rightarrow \psi(2S)\phi)/\mathcal{B}(B_s^0 \rightarrow J/\psi\phi)$

Table 5.2 shows the observed number of events from data and Table 5.3 shows the current measured branching ratio for different decay modes. Together with the relative efficiencies determined from Monte Carlo, we can then measure the relative branching ratio using the formula described earlier:

$$\begin{aligned}
& \frac{\mathcal{B}(B_s^0 \rightarrow (\psi(2S) \rightarrow \mu^+\mu^-)\phi)}{\mathcal{B}(B_s^0 \rightarrow J/\psi\phi)} \\
&= \frac{N(B_s^0 \rightarrow \psi(2S)\phi)\mathcal{B}(J/\psi \rightarrow \mu^+\mu^-)\mathcal{B}(\phi \rightarrow KK)}{N(B_s^0 \rightarrow J/\psi\phi)\mathcal{B}(\psi(2S) \rightarrow \mu^+\mu^-)\mathcal{B}(\phi \rightarrow K^+K^-)} \times \frac{\epsilon_{(B_s^0 \rightarrow J/\psi\phi; J/\psi \rightarrow \mu^+\mu^-)}}{\epsilon_{(B_s^0 \rightarrow \psi(2S)\phi; \psi(2S) \rightarrow \mu^+\mu^-)}} \\
&= \frac{N(B_s^0 \rightarrow \psi(2S)\phi)\mathcal{B}(J/\psi \rightarrow \mu^+\mu^-)}{N(B_s^0 \rightarrow J/\psi\phi)\mathcal{B}(\psi(2S) \rightarrow \mu^+\mu^-)} \times \frac{\epsilon_{(B_s^0 \rightarrow J/\psi\phi; J/\psi \rightarrow \mu^+\mu^-)}}{\epsilon_{(B_s^0 \rightarrow \psi(2S)\phi; \psi(2S) \rightarrow \mu^+\mu^-)}}
\end{aligned}$$

Table 5.4 shows the measured relative branching ratios in this analysis, together with the previous published measurement results. We obtain $\mathcal{B}(B_s^0 \rightarrow \psi(2S)\phi)/\mathcal{B}(B_s^0 \rightarrow J/\psi\phi) = 0.52 \pm 0.13(stat)$.

Decay	Yield	Comments
$B_u^\pm \rightarrow J/\psi K^\pm$	3530.5 ± 56.8	Control sample
$B_u^\pm \rightarrow \psi(2S)K^\pm; \psi(2S) \rightarrow \mu^+\mu^-$	325.4 ± 23.0	Control sample
$B_s^0 \rightarrow J/\psi\phi$	292.2 ± 15.9	Normalization mode
$B_s^0 \rightarrow \psi(2S)\phi; \psi(2S) \rightarrow \mu^+\mu^-$	20.2 ± 5.0	Signal mode

Table 5.2: The observed number of events.

Decay	Branching Ratio (PD)
$J/\psi \rightarrow \mu^+\mu^-$	$(5.88 \pm 0.10) \%$
$\psi(2S) \rightarrow \mu^+\mu^-$	$(7.3 \pm 0.8) \times 10^{-3}$
$\psi(2S) \rightarrow J/\psi\pi^+\pi^-$	$(31.8 \pm 1.0) \%$
$\phi \rightarrow K^+K^-$	$(49.2 \pm 0.6) \%$

Table 5.3: The PDG values for different decay modes [13].

Decay	This analysis	CDF Run I	Reference
$\frac{\mathcal{B}(B_d^0 \rightarrow \psi(2S)K^{*0})}{\mathcal{B}(B_d^0 \rightarrow J/\psi K^{*0})}$		$0.52 \pm 0.11 \pm 0.05$	0.61 ± 0.10 [PDG 04]
$\frac{\mathcal{B}(B_u^\pm \rightarrow \psi(2S)K^\pm)}{\mathcal{B}(B_u^\pm \rightarrow J/\psi K^\pm)}$	0.72 ± 0.05	$0.56 \pm 0.08 \pm 0.06$	0.64 ± 0.06 [BaBar 02]
$\frac{\mathcal{B}(B_s^0 \rightarrow \psi(2S)\phi)}{\mathcal{B}(B_s^0 \rightarrow J/\psi\phi)}$	0.52 ± 0.13		

Table 5.4: The measured relative branching ratios in this analysis, together with published results, where the first error is statistical and the second error is systematics.

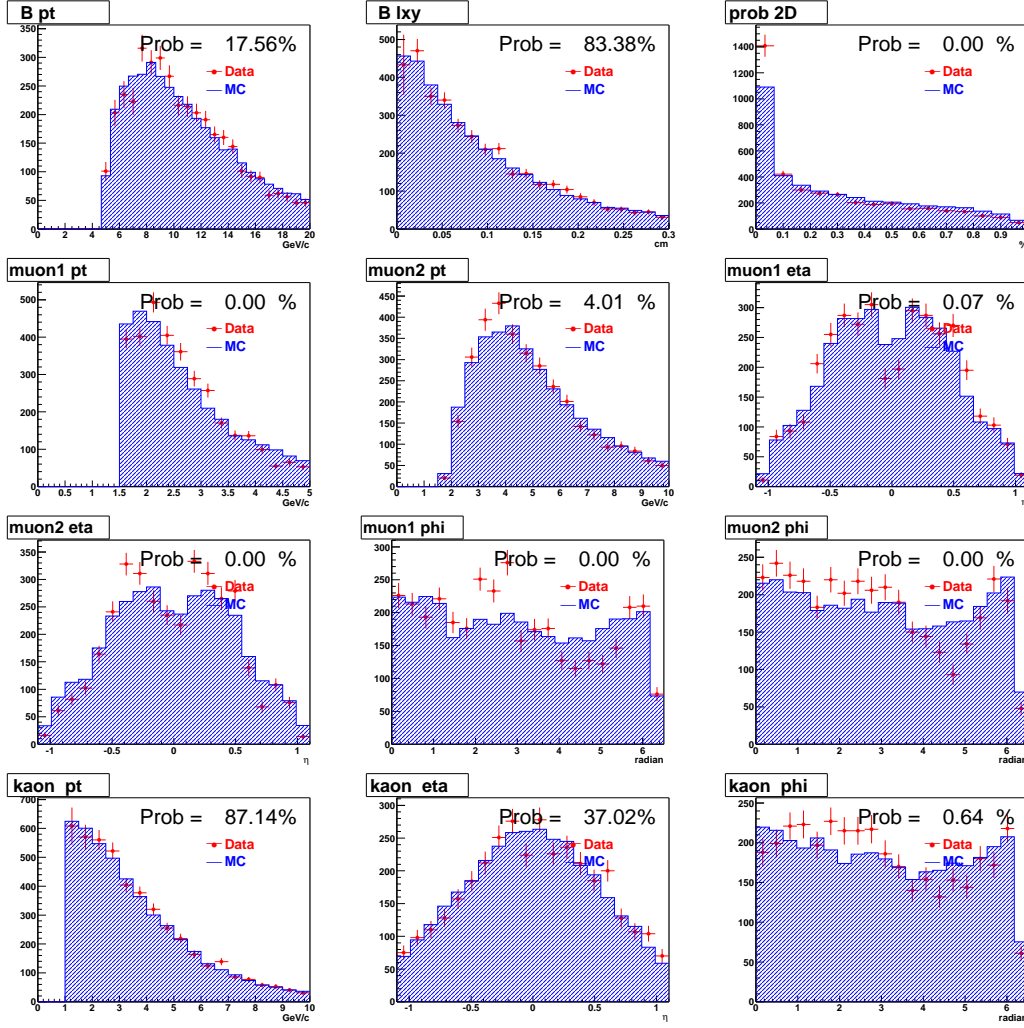


Figure 5.1: Comparison between Monte Carlo sample with sideband subtracted data sample in the decay of $B_u^\pm \rightarrow J/\psi K^\pm$. See description in Section 5.3.

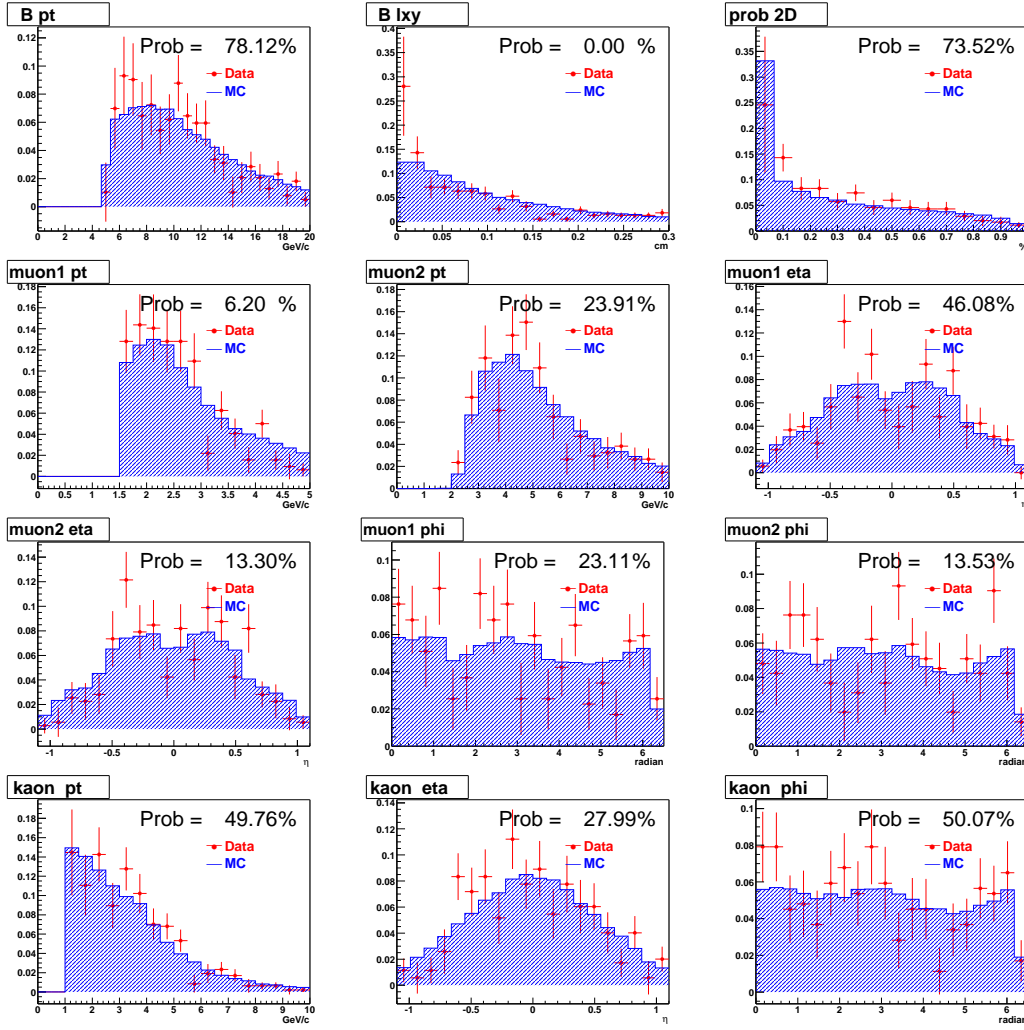


Figure 5.2: Comparison between Monte Carlo sample with sideband subtracted data sample in the decay of $B_u^\pm \rightarrow \psi(2S)K^\pm, \psi(2S) \rightarrow \mu^+\mu^-$. See description in Section 5.3.

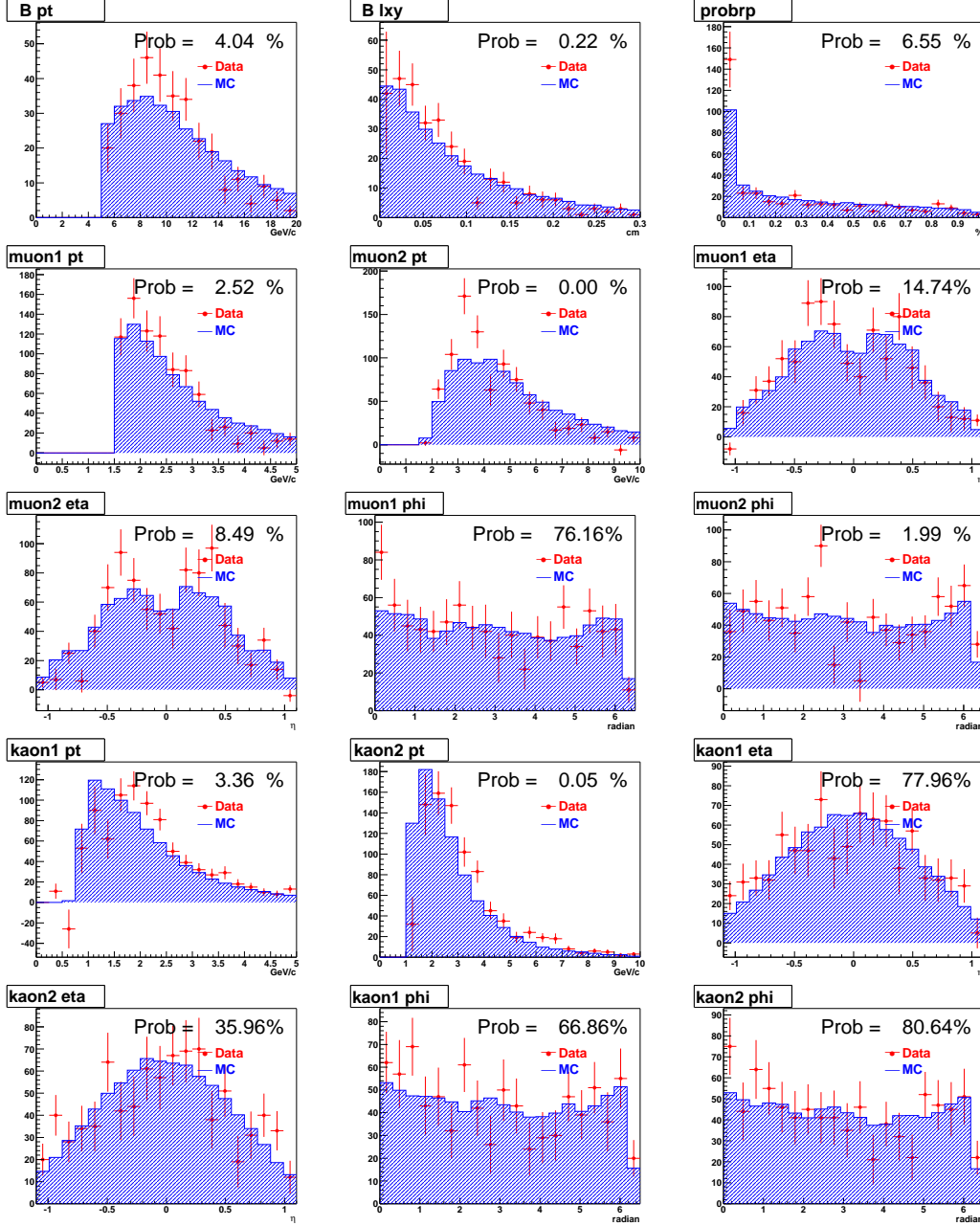


Figure 5.3: Comparison between Monte Carlo sample with sideband subtracted data sample in the decay of $B_s^0 \rightarrow J/\psi\phi$. See description in Section 5.3.

Chapter 6

Systematic studies and consistency checks

6.1 Introduction

As described already above, the relative branching ratio measurement is done with the formula below:

$$\begin{aligned} & \frac{\mathcal{B}(B_s^0 \rightarrow (\psi(2S) \rightarrow \mu^+\mu^-)\phi)}{\mathcal{B}(B_s^0 \rightarrow J/\psi\phi)} \\ &= \frac{N(B_s^0 \rightarrow \psi(2S)\phi)\mathcal{B}(J/\psi \rightarrow \mu^+\mu^-)\mathcal{B}(\phi \rightarrow K^+K^-)}{N(B_s^0 \rightarrow J/\psi\phi)\mathcal{B}(\psi(2S) \rightarrow \mu^+\mu^-)\mathcal{B}(\phi \rightarrow K^+K^-)} \times \frac{\epsilon_{(B_s^0 \rightarrow J/\psi\phi; J/\psi \rightarrow \mu^+\mu^-)}}{\epsilon_{(B_s^0 \rightarrow \psi(2S)\phi; \psi(2S) \rightarrow \mu^+\mu^-)}} \\ &= \frac{N(B_s^0 \rightarrow \psi(2S)\phi)\mathcal{B}(J/\psi \rightarrow \mu^+\mu^-)}{N(B_s^0 \rightarrow J/\psi\phi)\mathcal{B}(\psi(2S) \rightarrow \mu^+\mu^-)} \times \frac{\epsilon_{(B_s^0 \rightarrow J/\psi\phi; J/\psi \rightarrow \mu^+\mu^-)}}{\epsilon_{(B_s^0 \rightarrow \psi(2S)\phi; \psi(2S) \rightarrow \mu^+\mu^-)}} \end{aligned} \quad (6.1)$$

From here, one can see there are a few different types of systematics involved:

- Systematics due to the branching ratio $\mathcal{B}(\psi(2S) \rightarrow \mu^+\mu^-)$ and $\mathcal{B}(J/\psi \rightarrow \mu^+\mu^-)$.

This is likely the dominate systematics. The detail is discussed later.

- Systematics due to the signal yield determination, or fitting, for $N(B_s^0 \rightarrow \psi(2S)\phi)$ and $N(B_s^0 \rightarrow J/\psi\phi)$. One expects partial cancellation in the ratio. We will evaluate the systematic uncertainties by varying the fitting range and using different fitting functions.
- Systematics due to the determination of the efficiencies: $\epsilon_{(B_s^0 \rightarrow J/\psi\phi)}$ and $\epsilon_{(B_s^0 \rightarrow \psi(2S)\phi)}$.

Here one expects most effects cancel out in the ratio. This is due to the fact that both modes are B_s^0 decays, and the decay topologies are very similar. However, one has to worry about any differences due to the decay kinematics resulting in different distributions for the parameters (such as P_T distribution of tracks) used in the selection cuts. For example, there will be some difference due to the fact that $\psi(2S)$ and J/ψ have difference masses. In addition, the polarization for the two decays could be different and the effect can be studied by Monte Carlo. Therefore, we will first use Monte Carlo to find out what distributions are different between the $B_s^0 \rightarrow \psi(2S)\phi$ and $B_s^0 \rightarrow J/\psi\phi$, and then study the systematic effects due to them. Whenever possible, we will use the control sample from data to evaluate the systematic uncertainties.

6.2 Monte Carlo comparison between $\psi(2S)$ and J/ψ modes

Figure 6.1 shows the comparison between various distributions for $B_s^0 \rightarrow \psi(2S)\phi$ followed by $\psi(2S) \rightarrow \mu^+\mu^-$ and $B_s^0 \rightarrow J/\psi\phi$ followed by $J/\psi \rightarrow \mu^+\mu^-$ decay modes. Note that all comparison plots are made without the analysis cut on that particular distribution. For example, the L_{xy} distribution was made without the L_{xy} cut. The name convention for each individual plot is similar to the ones described in Section 4.3. Most of the distributions are very similar (as expected, some are almost identical, such as P_T of B_s^0 , L_{xy} of B_s^0 , prob of B vertex fit etc). However, the P_T of muons are somewhat different, especially around low P_T range. In Figure 6.1, muon1 is the muon with lower P_T while muon2 is the one with higher P_T in the same event. Since the trigger and detection efficiency is not flat at low P_T and is not modeled well in realistic Monte Carlo, we will need to study the systematics using real data. The details of the study is described in the next section. The P_T of kaon (kaon1 is the lower P_T kaon, while kaon2 is the higher one) is also somewhat different between the two decay modes. However, all kaon P_T are above 800 MeV/c, and the detection efficiency is reasonably flat therefore we do not expect large systematics uncertainty due to this.

Figure 6.2 shows the same comparison between $B_u^\pm \rightarrow J/\psi K^\pm$ and $B_u^\pm \rightarrow \psi(2S)K^\pm$ with $\psi(2S) \rightarrow \mu^+\mu^-$. Similar differences are also found in the muon P_T distributions. This is not surprising as the main difference is due to the difference between $\psi(2S)$ and J/ψ in both B_s and B^\pm cases. This also means that we can use the control sample from real data (which has large statistics) to study the systematics and perform consistency checks. From the Monte Carlo comparison studies between the $\psi(2S)$ and J/ψ modes, we conclude that one of the main focus of the systematic study should be the difference in the muon P_T distribution (low P_T range). This is because the muon efficiency has a turn-on at low P_T range, above 2.5 GeV/c, the efficiency is flat. Although the difference is not large, the effects have to be studied. In addition, similar difference is found in the control sample, therefore, we can use the control

sample to perform consistency checks.

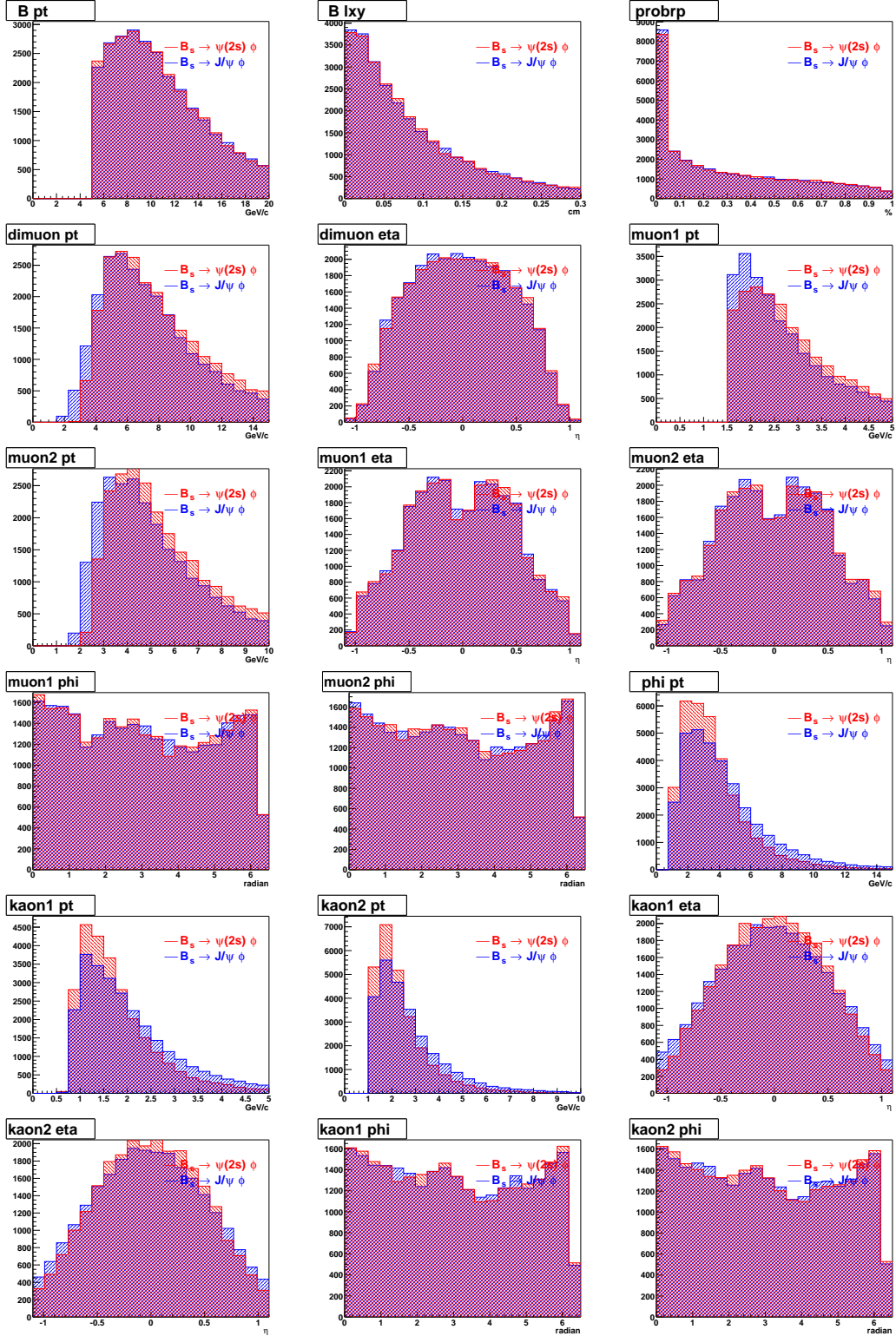


Figure 6.1: Comparison between Monte Carlo sample in the decay of $B_s^0 \rightarrow J/\psi\phi$ and $B_s^0 \rightarrow \psi(2S)\phi, \psi(2S) \rightarrow \mu^+\mu^-$

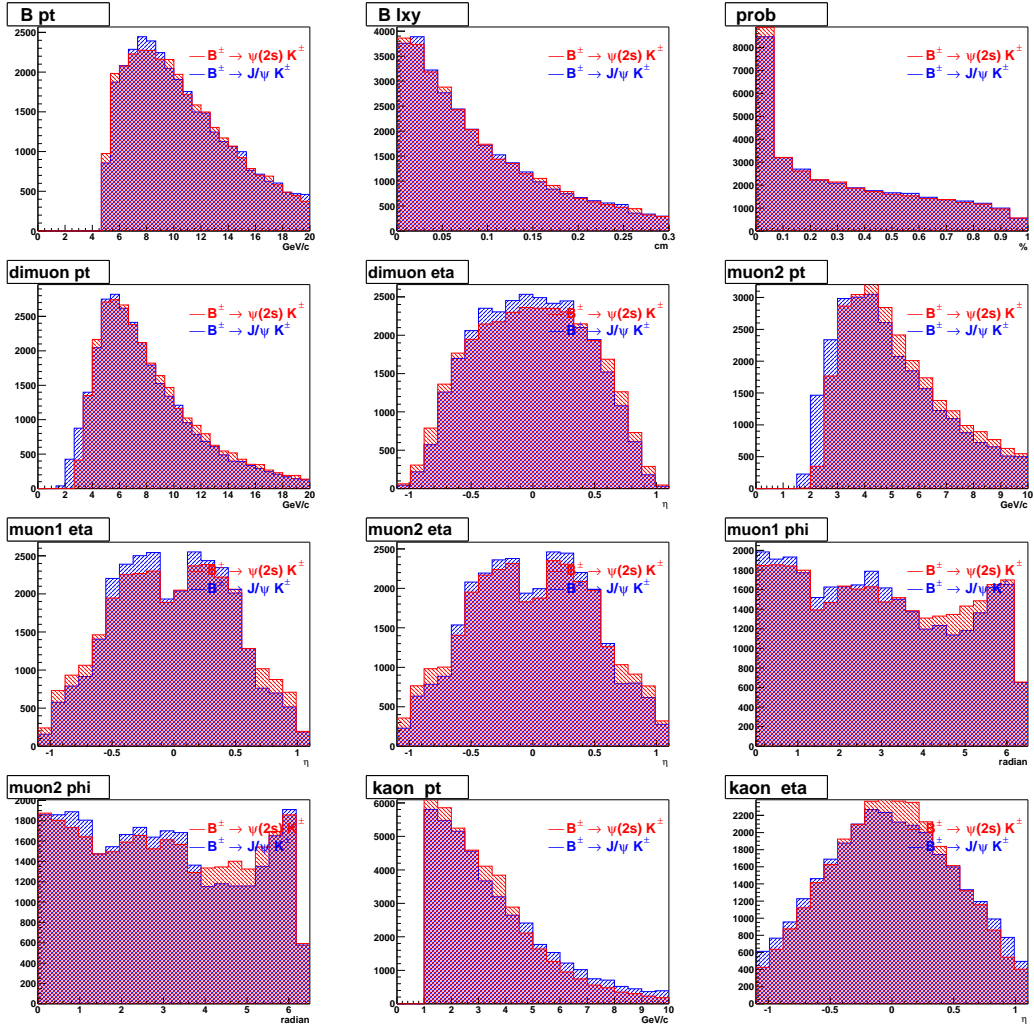


Figure 6.2: Comparison between Monte Carlo sample in the decay of $B_u^\pm \rightarrow J/\psi K^\pm$ and $B_u^\pm \rightarrow \psi(2S) K^\pm, \psi(2S) \rightarrow \mu^+ \mu^-$

6.3 Systematic Studies

6.3.1 Transverse Momentum of Muon

So far, we have done consistency checks using the control samples from real data with different P_T ranges. We have found that all results are statistically consistent, indicating the systematics due to the muon P_T distribution is small. However, those consistency checks are still statistically limited. Another way to study the systematics is to use the muon efficiencies measured directly from data. The single muon efficiency has been very carefully measured from the same data samples in $B_s \rightarrow \mu^+ \mu^-$ analysis [55], and the measurement was done in such a way that the dependences of P_T , phi, eta of the muon as well as run ranges are all taken care of. We apply the central values and combined error (statistical and systematic) of the measured efficiency curves to the Monte Carlo samples at event by event level, to recalculate the relative efficiency for both the B^\pm and B_s decays. The results will be used as systematical corrections to the central value of the relative efficiencies obtained from Monte Carlo before. Since each of the measurement has its own error, we will use those errors of the measurements to evaluate the systematic uncertainties (due to the lack of precise knowledge on the actual muon efficiency). To do that, we will increase or decrease each measured muon efficiency by 2σ , and recalculate the relative efficiency of the decay modes. We will take the difference between the two cases as the systematic uncertainty for the final measurement.

Table 6.1 shows the results. The difference is very small for both the corrected central value as well as the uncertainties, we therefore assign no systematics due to the P_T of the muon distribution difference.

6.3.2 Polarization

As mentioned earlier, the polarization of the $B_s^0 \rightarrow \psi(2S)\phi$ and $B_s^0 \rightarrow J/\psi\phi$ does not have to be the same, even though one would naively expect them to be similar. Different polarization could result in different detection efficiency for the two modes. So far, we have assumed that the two modes have the same

	$\epsilon(\frac{B_u^\pm \rightarrow J/\psi K^\pm}{B_u^\pm \rightarrow \psi(2S)K^\pm})$	$\epsilon(\frac{B_s^0 \rightarrow J/\psi \phi}{B_s^0 \rightarrow \psi(2S)\phi})$
Nominal	0.9719 ± 0.0075	0.9249 ± 0.0058
Corrected	0.9774 ± 0.0092	0.9095 ± 0.0096
+1 σ	0.9779 ± 0.0091	0.9102 ± 0.0095
- 1 σ	0.9768 ± 0.0093	0.9088 ± 0.0097
+2 σ	0.9784 ± 0.0090	0.9108 ± 0.0094
- 2 σ	0.9762 ± 0.0094	0.9081 ± 0.0098

Table 6.1: Systematics study using single muon efficiency measured from real data.

polarization when determine the relative efficiency. To study the systematics due to the lack of knowledge on the polarization for the $B_s^0 \rightarrow \psi(2S)\phi$, we generate Monte Carlo samples with purely CP even and CP odd for $B_s^0 \rightarrow \psi(2S)\phi$. Figure 6.3 shows the comparison between the CP even and CP odd cases for the $B_s^0 \rightarrow \psi(2S)\phi$. The name convention for each individual plot is similar to the ones described in Section 4.3.

We repeat the analysis, and Table 6.2 shows the results on the relative efficiency for the two extreme cases and the final results on the ratio of branching ratios. We take the difference of relative efficiency between the two extreme cases as systematics uncertainty (5.5%) due to the lack of knowledge on the polarization for $B_s^0 \rightarrow \psi(2S)\phi$. This is likely an overestimate. Note that in principle, one should also worry about the possible difference in lifetime between the CP even and CP odd modes. At this point, we have ignored this possible effects since one expects the polarization is similar (to first order) between the two modes, and we will evaluate this effect in details later.

Mode	Relative efficiency	$\frac{\mathcal{B}(B_s^0 \rightarrow \psi(2S)\phi)}{\mathcal{B}(B_s^0 \rightarrow J/\psi \phi)}$
Nominal	0.9249 ± 0.0058	0.52 ± 0.13
CP even	0.9381 ± 0.0082	0.52 ± 0.13
CP odd	0.8872 ± 0.0075	0.49 ± 0.13

Table 6.2: Comparison between CP even and CP odd $B_s^0 \rightarrow \psi(2S)\phi$

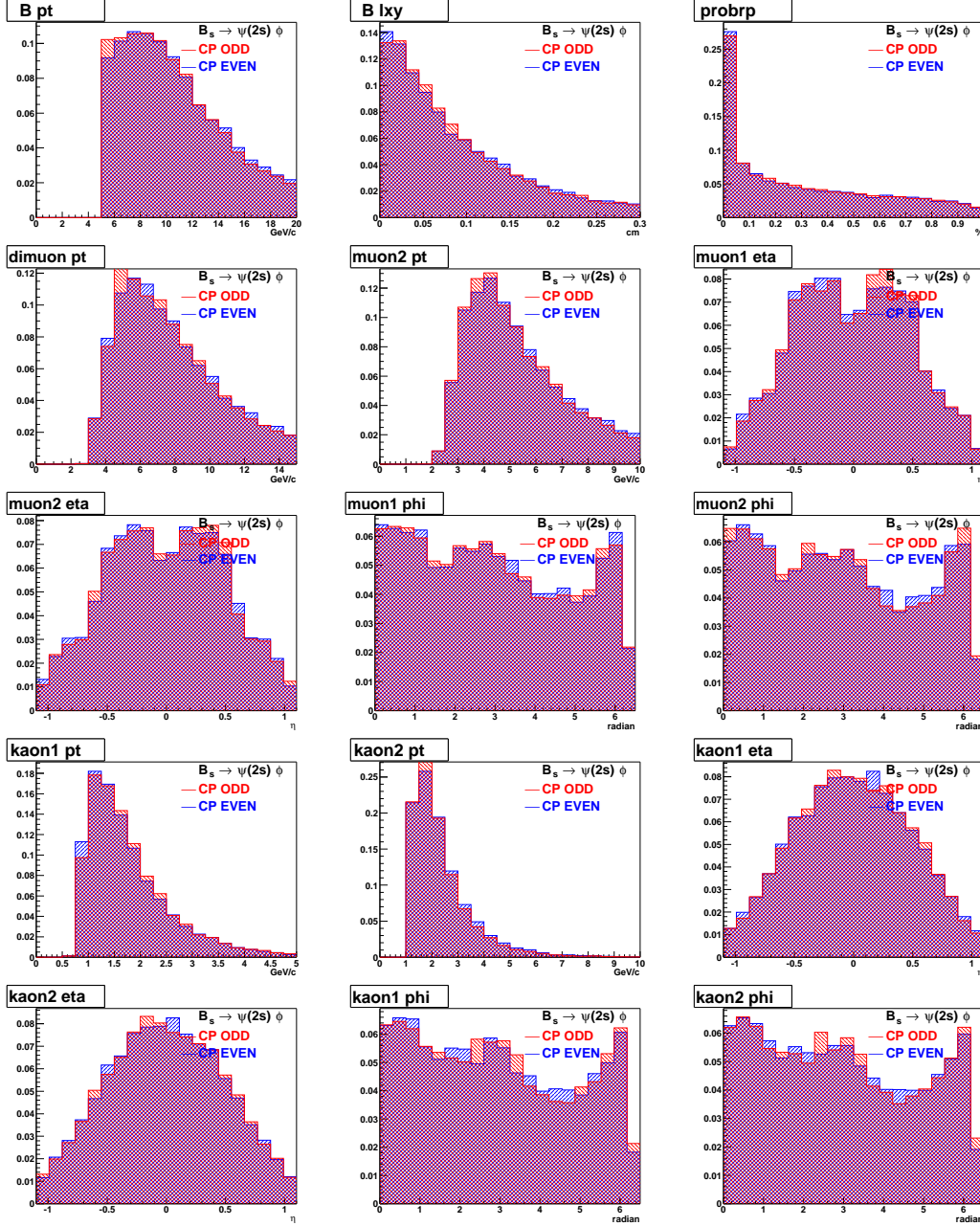


Figure 6.3: Comparison between Monte Carlo sample in the decay of CP even and CP odd of $B_s^0 \rightarrow \psi(2S)\phi, \psi(2S) \rightarrow \mu^+\mu^-$

6.3.3 Fitting

We evaluate the systematic uncertainty due to fitting by varying the fitting range and using different fitting methods. No significant variations observed. For example, Figure 6.4 and Figure 6.5 show the mass distributions with fitting results where the fitting range is between 5.2 to 5.5 GeV/ c^2 for all decay modes. Table 6.3 shows the results of systematic studies due to fitting.

One can estimate the systematics error for fit variance as follows:

$$\sigma = \sqrt{\frac{\sum_i x_i^2 - N \langle x \rangle^2}{N-1}}$$

where,

$$\langle x \rangle = \sum_i x_i / N$$

We obtain the systematic errors due to fitting method as 3.9 %.

Fitting method	Value
Nominal	0.52 ± 0.13
Unbinned likelihood fit(width floating)	0.49 ± 0.13
Binned likelihood fit(width fixed)	0.52 ± 0.14
Binned χ^2 fit(width fixed)	0.52 ± 0.14
2 Gaussian + 1st order polynomial	0.49 ± 0.13
Gaussian + 2nd order polynomial(width fixed)	0.52 ± 0.14

Table 6.3: The systematics study due to fitting.

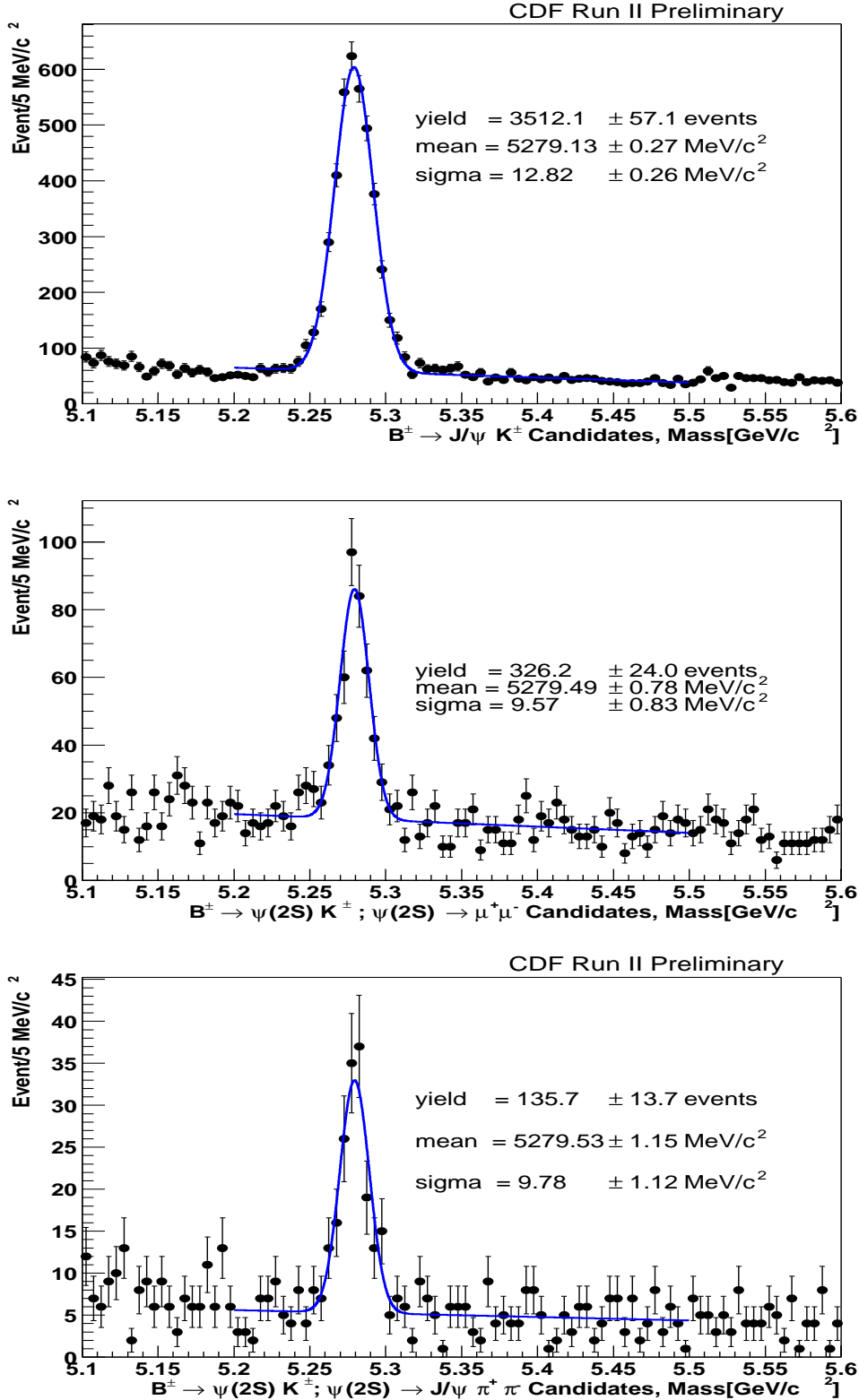


Figure 6.4: $B^\pm \rightarrow J/\psi(\psi(2S))K^\pm$ mass distribution where $J/\psi \rightarrow \mu^+\mu^-$, $\psi(2S) \rightarrow \mu^+\mu^-$ or $\psi(2S) \rightarrow J/\psi\pi^+\pi^-$. The mass distribution is fitted with a

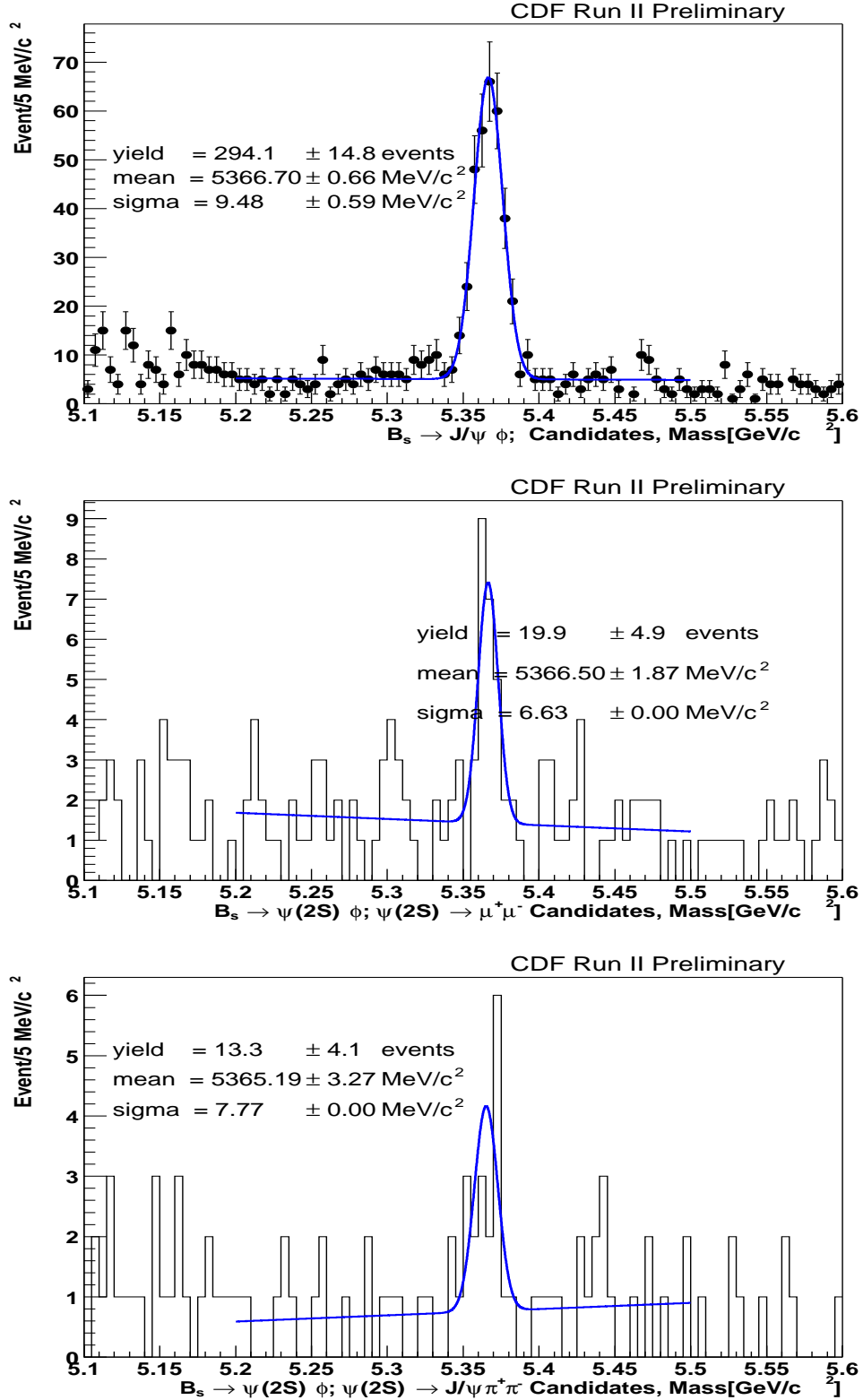


Figure 6.5: $B_s^0 \rightarrow J/\psi(\psi(2S))\phi$ mass distribution where $J/\psi \rightarrow \mu^+\mu^-$, $\psi(2S) \rightarrow \mu^+\mu^-$ or $\psi(2S) \rightarrow J/\psi\pi^+\pi^-$. The mass distribution is fitted with a

6.3.4 Daughter branching fraction

The branching ratios and uncertainties of daughter particles is taken from the Particle Data Group [13].

- $B(J/\psi \rightarrow \mu^+\mu^-) = (5.88 \pm 0.10) \%$
- $B(\psi(2S) \rightarrow \mu^+\mu^-) = (7.3 \pm 0.8) 10^{-3}$
- $B(\psi(2S) \rightarrow J/\psi\pi^+\pi^-) = (31.8 \pm 1.0) \%$
- $B(\phi \rightarrow K^+K^-) = (49.2 \pm 0.6) \%$

The result of this analysis is dominated by the current (PDG) experimental measurement uncertainties on $\mathcal{B}(\psi(2S) \rightarrow \mu^+\mu^-)$ which is $(7.3 \pm 0.8) \times 10^{-3}$ (11%), since the $\mathcal{B}(J/\psi \rightarrow \mu^+\mu^-)$ is well measured. This effect does not cancel in the ratio.

For $\psi(2S)$ decays, $(\mathcal{B}\psi(2S) \rightarrow J/\psi\pi^+\pi^-)$ has been well measured in the past compared to that for $\psi(2S) \rightarrow \mu^+\mu^-$. In principle, one could use CDF data to determine the ratio of $\psi(2S) \rightarrow \mu^+\mu^-$ with respect to $\psi(2S) \rightarrow J/\psi\pi^+\pi^-$, thus effectively measure the $\mathcal{B}(\psi(2S) \rightarrow \mu^+\mu^-)$ with better precision (one will need to worry about the systematics due to the two extra π tracks). However, given the fact that this is the first observation for the $B_s^0 \rightarrow \psi(2S)\phi$ decay mode, the relative branching ratio measurement uncertainty is dominated by statistics, it makes more sense to improve the systematics due to the $\mathcal{B}(\psi(2S) \rightarrow \mu^+\mu^-)$ later when we have much more data.

6.4 Consistency checks

6.4.1 Transverse Momentum of Muon

The first thing one could try is to use the control sample, and require the lower P_T muon to be above 2.5 GeV/ c and the higher P_T muon to be above 3.0 GeV/ c . This way, all muons have P_T well above the turn on where the efficiency is flat. The results is in Table 6.4, and no significant difference in the final results seen, even though the relative efficiency changes due to the cuts made.

Decay	cuts	relative efficiency	$\frac{\mathcal{B}(B_u^\pm \rightarrow \psi(2S)K^\pm)}{\mathcal{B}(B_u^\pm \rightarrow J/\psi K^\pm)}$
$B_u^\pm \rightarrow J/\psi K^\pm$ $B_u^\pm \rightarrow \psi(2S)K^\pm$	Nominal cuts	0.9719 ± 0.0075	0.72 ± 0.05
$B_u^\pm \rightarrow J/\psi K^\pm$ $B_u^\pm \rightarrow \psi(2S)K^\pm$	Low P_T muon > 2.5 GeV/ c high P_T muon > 3.0 GeV/ c	0.9160 ± 0.0096	0.71 ± 0.06

Table 6.4: Consistency check with control sample, with high P_T muons only.

	μ -low $P_T < 2.4 \text{ GeV}/c$	μ -low $P_T > 2.4 \text{ GeV}/c$
μ -high $P_T < 4.25 \text{ GeV}/c$	$0.86 \pm 0.14 (1.3339 \pm 0.0227)$	$0.70 \pm 0.19 (0.9448 \pm 0.0193)$
μ -high $P_T > 4.25 \text{ GeV}/c$	$0.71 \pm 0.13 (0.8496 \pm 0.0147)$	$0.78 \pm 0.07 (0.9160 \pm 0.0107)$

Table 6.5: The relative branching ratio of split samples with different muon P_T .

We then split the control samples into four groups (note that we use muon1 and muon2 to indicate the lower and higher P_T muon in the same event):

- low P_T for muon1 and low P_T for muon2;
- low P_T for muon1 and high P_T for muon2;
- high P_T for muon1 and low P_T for muon2;

- high P_T for muon1 and high P_T for muon2;

The results are shown in Table 6.5, the final ratio of branching ratios are shown in the table for each group of samples, and the relative efficiencies are also shown in bracket. The four groups are statistically independent samples, and the results are statistically compatible.

6.4.2 Run ranges

During the data taking in the past few years, the muon efficiency has been changed over the different run ranges. For example, XFT has changed from 2-miss to 1-miss configuration, certain run ranges are affected by COT aging etc. For this analysis, we only care the relative efficiency for the decay modes involved and it is expected to be less sensitive to the run ranges comparing to the absolute efficiency for each decay mode. However, it is important to perform consistency checks over different run ranges. We therefore divide the data sample into three different run ranges, and repeat the analysis on the control sample. The results are shown in Table 6.6. The three run ranges are statistically independent, and the results are also statistically compatible.

Control sample	Run < 152635	152636 < Run < 168889	Run > 174778
$\epsilon(\frac{B_u^\pm \rightarrow J/\psi K^\pm}{B_u^\pm \rightarrow \psi(2S)K^\pm})$	0.976 ± 0.023	0.989 ± 0.010	0.973 ± 0.011
$\frac{\mathcal{B}(B_u^\pm \rightarrow \psi(2S)K^\pm)}{\mathcal{B}(B_u^\pm \rightarrow J/\psi K^\pm)}$	0.78 ± 0.16	0.79 ± 0.08	0.66 ± 0.08

Table 6.6: Consistency check with control sample, with different run ranges.

6.4.3 Transverse Momentum of Kaon

For Kaon P_T distribution, there are some difference between $B_s^0 \rightarrow \psi(2S)\phi$ and $B_s^0 \rightarrow J/\psi\phi$ as shown in Figure 6.1. However, we use the Kaon P_T distribution which is above 800 MeV/ c where we expect the detection efficiency is reasonably flat. Monte Carlo studies show the above is well modeled (note that

we only care about the ratio of efficiency, not the absolute value). Nevertheless, we perform consistency checks using the control sample. We divided the control sample into two statistically independent samples: low Kaon P_T (1.0 - 3.0 GeV/ c) and high Kaon P_T (> 3.0 GeV/ c) region. We then repeated the analysis for the ratio of branching ratio measurement for the control sample. The results are shown in Table 6.7. The relative efficiency is different for the two P_T ranges as expected (due to the difference in the shape of Kaon P_T distribution), however, the final ratio of branching ratio is consistent with each other.

Control sample	$1.0 < \text{kaon}(P_T) < 3.0 \text{ GeV}/c$	$\text{kaon}(P_T) > 3.0 \text{ GeV}/c$
$\epsilon(\frac{B_u^\pm \rightarrow J/\psi K^\pm}{B_u^\pm \rightarrow \psi(2S) K^\pm})$	0.8514 ± 0.0066	1.0292 ± 0.0095
$\frac{\mathcal{B}(B_u^\pm \rightarrow \psi(2S) K^\pm)}{\mathcal{B}(B_u^\pm \rightarrow J/\psi K^\pm)}$	0.67 ± 0.08	0.77 ± 0.06

Table 6.7: Consistency check with control sample, with different kaon P_T ranges.

6.4.4 Other cuts

We have also performed consistency checks on other cuts, the type of cuts we do not expect to have systematic effects as they should drop in the ratio because the distributions are either very similar (P_T of B , vertex probability cut etc, or the detection efficiency is flat (such as Kaon P_T). For these consistency checks, we followed the so called “N-1 cut” approach in cdf note 6708 (see page 18) on measurement of relative branching ratio of $\mathcal{B}(B_s \rightarrow D_s^- \pi^+) / \mathcal{B}(B^0 \rightarrow D^- \pi^+)$.

In this approach, one can evaluate the efficiency of a single cut given that the other N-1 cuts are applied in the following way. One can define a ratio:

$$P^{data, MC} = \frac{n_s - n_b}{N_s - N_b},$$

where n_s, n_b is number of events after N cut and N_s, N_b is number of events after N-1 cut applied, for signal region and sideband region respectively. This

ratio can be compared between data and Monte Carlo. The statistical error on the ratio can be derived using propagation of binomial errors:

$$\sigma(P^{data,MC}) = \frac{\sqrt{N_s \cdot (n_s/N_s) \cdot (1-n_s/N_s) + N_b \cdot (n_b/N_b) \cdot (1-n_b/N_b)}}{N_s - N_b}$$

For this analysis, we can compare the following ratio for data and Monte Carlo:

$$R = \frac{P^{data}(B_u^\pm \rightarrow \psi(2S)K^\pm) / P^{data}(B_u^\pm \rightarrow J/\psi K^\pm)}{P^{MC}(B_u^\pm \rightarrow \psi(2S)K^\pm) / P^{MC}(B_u^\pm \rightarrow J/\psi K^\pm)}$$

Ideally, 1-R should be 0. If 1-R is different from 0 in a statistically significant way, one has to worry about the potential systematic errors. Therefore, this can be used as a consistency check. Table 6.8 shows the results on some of the cut variables and no significant discrepancy is found.

cut	1-R	$\sigma(1 - R)$	Significance
$P_T(B)$	-0.0016	0.0339	0.05
prob(B)	-0.1007	0.0673	1.50
$L_{xy}(B)$	-0.1015	0.0641	1.58
$P_T(K^\pm)$	-0.0944	0.0403	2.34

Table 6.8: Consistency checks on different cuts for the control sample $B_u^\pm \rightarrow J/\psi K^\pm$ and $B_u^\pm \rightarrow \psi(2S)K^\pm$ using the “N-1 cut” approach.

6.5 Summary for systematic errors

Table 6.9 summarize the systematic errors for the relative branching ratio measurement. The total systematic error is 6.7% and is dominated by polarization, this does not include the systematic error due to the daughter branching ratio (which is separated). One could also separate the systematical uncertainty due to polarization, but since it is relatively small, we choose to combine it with the fitting systematics for now.

Source	%
Muon P_T	-
Polarization	5.5
Fitting	3.9
Total	6.7

Table 6.9: Summary of systematic studies.

Chapter 7

Conclusions

In summary, we present the first observation of $B_s^0 \rightarrow \psi(2S)\phi$ decay in $p\bar{p}$ collisions at $\sqrt{s} = 1.96$ TeV using 360 pb^{-1} of data collected by the CDF II detector at the Fermilab Tevatron. We observe 20.2 ± 5.0 and 12.3 ± 4.1 $B_s^0 \rightarrow \psi(2S)\phi$ candidates, in $\psi(2S) \rightarrow \mu^+\mu^-$ and $\psi(2S) \rightarrow J/\psi\pi^+\pi^-$ decay modes, respectively. We also present the first measurement of the relative branching fraction $\mathcal{B}(B_s^0 \rightarrow \psi(2S)\phi)/\mathcal{B}(B_s^0 \rightarrow J/\psi\phi) = 0.52 \pm 0.13(\text{stat.}) \pm 0.04(\text{syst.}) \pm 0.06(\text{BR})$ using the $\psi(2S) \rightarrow \mu^+\mu^-$ decay mode. This result for B_s^0 is consistent with the ratios of branching fractions for the corresponding decays of B_u^\pm and B_d^0 [?].

The $B_s^0 \rightarrow \psi(2S)\phi$ and $B_s^0 \rightarrow J/\psi\phi$ decays are of particular interest because they are pseudoscalar to vector-vector transitions. The $B_s^0 \rightarrow J/\psi\phi$ mode has been recently used at CDF to determine the decay widths for the heavy and light B_s^0 mass eigenstates, by measuring the relative contribution of the CP -odd and CP -even components to the observed angular distribution as a function of the decay time [?]. This analysis is currently statistically limited, and observing the $B_s^0 \rightarrow \psi(2S)\phi$ would allow an independent measurement of the decay widths for the heavy and light B_s^0 mass eigenstates in the future. In particular, the polarization of $B_s^0 \rightarrow \psi(2S)\phi$ could be different from that of $B_s^0 \rightarrow J/\psi\phi$.

Bibliography

- [1] N.Cabibbo. Unitarity Symmetry and Leptonic Decays. Phys. Rev. Lett. **10**, 531 (1963).
- [2] M.Kobayashi and T. Maskawa. CP-Violation in the Renormalizable Theory of Weak Interaction. Prog. Theor. Phys. **49**, 652 (1973).
- [3] R.P.Feynman and M. Gell-Mann. Theory of the Fermi Interaction. Phys. Rev. **109**, 193 (1958).
- [4] J.J.Sakurai. Mass Reveal and Weak Interactions. Nuovo Cim. **7**, 649 (1958).
- [5] D.H.Perkins. Introduction to High Energy Physics. Addison-Wesley, Nenlo Park, California, 3rd edition (1987).
- [6] S.L.Glashow. Partial-Symmetries of Weak Interactions. Nucl. Phys. **22**, 579 (1961).
- [7] S.Weinberg. A Model of Leptons. Phys. Rev. Lett. **19**, 1264 (1967).
- [8] A.Salam. Weak and Electromagnetic Interactions: Elementary Particle Theory. Almqvist and Wiksells, Stockholm (1968).
- [9] N.Ellis and A.Kernan, Heavy Quark Production at the CERN $p\bar{p}$ Collider, Phys. Rep. **195**, 23 (1990).
- [10] P.Nason, S.Dawson and R.K.Ellis, The Total Cross Section for the Production of Heavy Quarks in Hadronic Collisions, Nucl. Phys. **B 303**, 607 (1988).

- [11] P.Nason, S.Dawson and R.K.Ellis, The One Particle Inclusive Differential Cross Section for Heavy Quark Production in Hadronic Collision, Nucl. Phys. **B 327**, 49 (1989); **B 303**, 260(E) (1989).
- [12] M.Luke and M.J.Savage, Extracting $|V_{bc}|$, m_c , and m_b from Inclusive D and B Decays, Phys. Lett. **B 321**, 88 (1994).
- [13] L.Alvarez-Gaume *et al.*, Phys. Lett. **B 592**, 1 (2004).
- [14] Torbjorn Sjostrand. Status of Fragmentations Models. Int. J. Mod. Phys. **A 3**, 751 (1988).
- [15] C.Peterson et al. Scaling Violations in Inclusive e^+e^- Annihilation Spectra. Phys. Rev. **D 27**, 105 (1983).
- [16] J.Chrin. Upon the Determination of Heavy Quark Fragmentation Functions in e^+e^- Annihilation Phys. Rev. Lett. **67**, 2418 (1988).
- [17] G.Kramer and W.F.Palmer. Branching Ratios and CP Asymmetries in the Decay $B \rightarrow VV$. Phys. Rev. **D 45**, 193 (1992).
- [18] G.Kramer and W.F.Palmer. Direct CP Asymmetries in the Decays $B \rightarrow VV$ from an Effective Weak Hamiltonian. Phys. Rev. **D 46**, 2969 (1992).
- [19] A.S.Dighe, I.Dunietz, H.J.Lipkin and J.L.Rosner. Angular Distributions and Lifetimes Differences in $B_s^0 \rightarrow J/\psi\phi$ Decays. Phys. Lett. **B 369**, 144 (1996).
- [20] A.S.Dighe, I.Dunietz, H.J.Lipkin and R.Fleischer. Extracting CKM Phases and $B_s - \bar{B}_s$ Mixing Parameters from Angular Distributions of Non-Leptonic B Decays. Eur. Phys. J. **C 6**, 647 (1999).
- [21] M.Gourdin, A.N.Kamal and X.Y.Pharm. Difficulties in Explaining Recent Data on $B \rightarrow J/\psi + K(K^0)$ Decays with commonly used Form Factors within the Factorization Approach. Phys. Rev. Lett. **73**, 3355 (1994).
- [22] I.Dunietz. $B_s - \bar{B}_s$ Mixing, CP violation, and Extraction of CKM Phases from Untagged B_s Data Samples, Phys. Rev.**D 52**, 3048 (1995).

- [23] M.Beneke, G.Buchella, I.Dunietz. Width Difference in the $B_s - \bar{B}_s$ System. Phys. Rev.**D 54**, 4419 (1996).
- [24] T.Affolder, CDF Collaboration, Measurement of $\sin 2\beta$ from $B \rightarrow J/\psi K_s^0$ with the CDF detector, Phys. Rev.**D 61**, 072005 (2000).
- [25] B.Aubert, Babar Collaboration, Measurement of the CP Asymmetry Amplitude $\sin 2\beta$ with B^0 Mesons. Phys. Rev. Lett. **89**, 201802 (2002).
- [26] K.Abe, Belle Collaboration, Improved measurement of CP-violation parameters $\sin 2\phi_1$ and $|\lambda|$, B meson lifetimes, and $B^0 - \bar{B}^0$ mixing parameter δm_d . Phys. Rev.**D 71**, 072003 (2005).
- [27] H.Albrecht *et al.*, ARGUS Collaboration, Phys. Lett. **B 199**, 451 (1987).
- [28] F.Abe *et al.*, CDF Collaboration, Phys. Rev. **D 58**, 072001 (1990).
- [29] S.J.Richichi *et al.*, CLEO2 Collaboration, Phys. Rev. **D 63**, 031103R (2001).
- [30] D.Buskulic *et al.*, ALEPH Collaboration, Phys. Lett. **B 311**, 425 (1993).
- [31] D.Buskulic *et al.*, BaBar Collaboration, Phys. Rev. **D 65**, 032001 (2002).
- [32] K.Anikeev *et al.* Time-Dependent Angular Analysis of $B_s \rightarrow J/\psi \phi$ and $B_d \rightarrow J/\psi K^{*0}$ Decays, CDF Note 7044.
- [33] Daejung Kong *et al.*, Observation of $B_s \rightarrow \psi(2S)\phi$ and measurement of $Br(B_s \rightarrow \psi(2S)\phi)/Br(B_s \rightarrow J/\psi\phi)$, CDF Note 7525
- [34] J. Cockcroft and E. Walton. Proc. Roy. Soc., 136:619, 1932
- [35] W. K. H. Panofsky *et al.*, Berkeley Proton Linear Accelerator. Rev. Sci. Instrum., 26:111, 1955.
- [36] D. Mohl, G. Petrucci, L. Thorndahl, and Simon Van Der Meer. Physics and Technique of Stochastic Cooling. Phys. Rept., 58:73-119, 1980.
- [37] <http://www-cdfonline.fnal.gov/opshelp/stores/>

- [38] <http://www-cdf.fnal.gov/internal/people/links/JacoboKonigsberg/instr02.ps>
- [39] S. Kilemko *et al.*, “The CDF Run II Luminosity Monitor,” CDF Note 4330.
- [40] Muge Karagoz Unel and Richard Tesarek, “Beam Halo Monitoring at CDF,” Nucl. Instrum. Meth. A **506**, 7 (2003), FERMILAB-PUB-02/304-E.
- [41] S. Nahn, “Status of the CDF Run II Silicon Detector,” CDF Note 6264.
- [42] COT group, A. Mukherjee, R. Wagner, “CDF Central Outer Tracker,” Nucl. Instrum. Meth. A **526**, 249 (2004), CDF Note 6267.
- [43] Shin-Shan Yu *et al.*, “COT dE/dx Measurement and Corrections,” CDF Note 6361.
- [44] K. Anikeev *et al.*, “Construction and Installation of the CDF Time-Of-Flight Counters for Run II,” CDF Note 5818.
- [45] C. Grozis *et al.*, “The Time-Of-Flight Detector at CDF,” Nucl. Phys. Proc. Suppl. A **47**, 344 (2001); Int. J. Mod. Phys. A16S1C, 1119 (2002).
- [46] F. Abe *et al.*, Nucl. Instrum. Meth. A **271**, 387 (1988).
- [47] CDF Collaboration, F. Abe *et al.*, Phys. Rev. D **52**, 4784 (1995) and D. Acosta *et al.*, Phys. Rev. D **65**, 112003 (2002).
- [48] CDF Collaboration, D. Acosta, *et al.*, “First Evidence for $B_s^0 \rightarrow \phi\phi$ Decay and Measurements of Branching Ratio and A_{CP} for $B^+ \rightarrow \phi K^+$,” Phys. Rev. Lett. **95**, 031801 (1997).
- [49] The CDF B Group’s Physics Analysis Kernel Subgroup
- [50] M. Campanelli *et al.* Calibration of the momentum scale for Kalman refitter using J/ψ events CDF Note 6905
- [51] A. Korn *et al.* Measurement of the B Hadron Masses in exclusive $m_{J/\psi}$ Decay Channels, CDF Note 6963

- [52] K.Anikeev et al. Description of Bgenerator II, CDF Note 5092
- [53] W.Bell et al. User Guide For EvtGen @ CDF, CDF Note 5618
- [54] T.Miao. The CDF Collaboration. Fully reconstructed B-meson decays using J/ψ and $\psi(2S)$, 1996. CDF Note 3844, FERMILAB-CONF-96/269-E
- [55] D.Glenzinski et al. Measurement of Level 1, 2 and 3 low p_T dimuon efficiencies for the $B_s \rightarrow \mu^+ \mu^-$ analysis, CDF Note 7314
- [56] http://www-cdf.fnal.gov/physics/statistics/statistics_faq.html
- [57] D.Acosta et al. Measurement of the J/ψ mesons and b quark production cross sections Phys. Rev. D **71**, 032001 (2005)

$B_s^0 \rightarrow \psi(2S)\phi$ 붕괴모드의 관찰과
 $B_s^0 \rightarrow \psi(2S)\phi$ 와 $B_s^0 \rightarrow J/\psi\phi$ 의 상대 갈래비 측정에 관한 연구

공 대 정

경북대학교 대학원 물리학과 입자물리학전공
(지도교수 김 동 희)

미국 페르미 국립 가속기 연구소의 Tevatron 가속기와 CDF 검출기를 이용하여 $B_s^0 \rightarrow \psi(2S)\phi$ 붕괴모드를 연구했다. 질량중심에너지 1.96 TeV 에서 양성자와 반양성자의 충돌로부터 획득한 총 휘도 $360pb^{-1}$ 실험자료를 사용하여 $\psi(2S) \rightarrow \mu^+\mu^-$ 와 $\psi(2S) \rightarrow J/\psi\pi^+\pi^-$ 붕괴를 이용하여 $B_s^0 \rightarrow \psi(2S)\phi$ 붕괴모드의 사건후보를 각각 20.2 ± 5.0 와 12.3 ± 4.1 로 관찰하였다. 또한 $\psi(2S) \rightarrow \mu^+\mu^-$ 를 이용하여 $B_s^0 \rightarrow \psi(2S)\phi$ 와 $B_s^0 \rightarrow J/\psi\phi$ 의 상대 갈래비를 다음과 같이 관찰하였다.

$\mathcal{B}(B_s^0 \rightarrow \psi(2S)\phi)/\mathcal{B}(B_s^0 \rightarrow J/\psi\phi) = 0.52 \pm 0.13(\text{stat.}) \pm 0.04(\text{syst.}) \pm 0.06(\text{BR})$
이것은 이미 발표된 B_u^\pm 와 B_d^0 의 맵시입자로의 최종 붕괴 상태의 결과와 일치함을 확인했다.

